Online coupling of TRIGA-TRAP to the research reactor TRIGA Mainz

Dissertation
zur Erlangung des Grades

"Doktor der Naturwissenschaften"

im Promotionsfach Kernchemie
am Fachbereich Chemie, Pharmazie und Geowissenschaften
der Johannes Gutenberg-Universität
in Mainz

Jessica Grund

geboren in
Frankfurt am Main

Mainz, den 18. April 2018

I was taught that the way of progress
is neither swift nor easy.

Marie Curie

Contents

Abstract

Penning traps are versatile tools to gain knowledge about ground state properties of nuclides through high-precision measurements of their atomic masses. They can be used to refine theoretical mass models, thereby contributing to the understanding of nucleosynthesis. The aim of this work was to couple the double-Penning-trap mass-spectrometry setup TRIGA-TRAP to the research reactor TRIGA Mainz to enable mass measurements of short-lived, neutron-rich nuclides produced by neutron induced fission of ^{235}U. These radio nuclides are transported by an aerosol-based gas-jet system and have to be subsequently ionized. For this, a surface ion source was designed and implemented. It enabled a reliable operation at temperatures above 2000 °C and yielded good ionization efficiencies for alkaline metals. The gas-jet was equipped with monitoring devices, which allowed gaining insight into the dependence of its performance as a function of the pressure inside the target chamber. Several beam diagnostics stations were installed along the beamline for extended characterization and optimization studies of individual components. Ion beams of fission products were generated, mass separated and transformed into ion bunches inside a gas-filled radio frequency quadrupole. The subsequent deceleration from 30 keV to 1.1 keV enabled the injection of radio nuclides into the first Penning trap. Four different short-lived ion species were identified through mass measurements by resonant buffer gas cooling inside this trap. The obtained masses agree with those of the AME2016 within their uncertainties. This dataset is the first obtained for short-lived nuclides at TRIGA-TRAP and confirms the successful transport of fission products from the target to the Penning trap, thereby finalizing the commissioning of TRIGA-TRAP.

Zusammenfassung

Penningfallen sind vielseitige Werkzeuge um durch Hochpräzisionsmessungen der atomaren Masse Wissen über Grundzustandseigenschaften von Atomkernen zu erlangen. Diese können zur Verfeinerung von theoretischen Kernmassenmodellen verwendet werden und tragen dadurch zum Verständnis der Nukleosynthese bei. Das Ziel dieser Arbeit war die Ankopplung des Doppel-Penningfallen-Massenspektrometrie-Aufbaus TRIGA-TRAP an den Forschungsreaktor TRIGA Mainz, um dadurch Massenmessungen von kurzlebigen, neutronenreichen Atomkernen zu ermöglichen, die durch neutroneninduzierte Spaltung von ^{235}U produziert werden. Diese Radionuklide werden mit Hilfe eines aerosolbeladenenen Gasjet-Systems transportiert und anschließend ionisiert. Dafür wurde eine Oberflächenionenquelle konzipiert und implementiert. Diese ermöglichte einen zuverlässigen Betrieb bei Temperaturen von über 2000 °C und ergab gute Ionisationseffizienzen für Alkalimetalle. Der Gasjet wurde mit Überwachungseinheiten ausgestattet, die Einblicke über den Zusammenhang zwischen dem Verhalten des Gasjets und dem Druck in der Targetkammer lieferten. Mehrere Strahldiagnostikstationen wurden entlang der Strahlstrecke installiert, um ausführliche Charakterisierungen und Optimierungen von einzelnen Komponenten zu ermöglichen. Ionenstrahlen aus Spaltprodukten wurden erzeugt, massensepariert und in einem gasgefüllten Radiofrequenz-Quadrupol zu Ionenbündeln transformiert. Die anschließende Abbremsung der Ionen von 30 keV auf 1.1 keV ermöglichte die Injektion von Radionukliden in die erste Penningfalle. Vier verschiedene kurzlebige Ionenspezies wurden mittels Massenmessung über resonante Puffergas-Kühlung in dieser Falle identifiziert. Die erhaltenen Massen stimmen im Rahmen der Fehler mit denen der AME2016 überein. Dieser Datensatz ist der erste, der bei TRIGA-TRAP von kurzlebigen Radionukliden aufgenommen wurde. Er bestätigt den erfolgreichen Transport von Spaltprodukten aus dem Target zur Penningfalle und schließt damit die Inbetriebnahme von TRIGA-TRAP ab.

Chapter 1

Introduction

Throughout its history humankind has been endeavouring to get comprehensive knowledge about the surrounding world. Extensive scientific research gained a lot of insight – in particular during the last century. However, there are still open questions, e.g., about the origin of the universe or how matter is formed. One of the greatest issues of the recent century is the identification of where in the universe elements heavier than iron are created. The so-called *r-process* and is one of the predominant processes for nucleosynthesis. It entails a succession of rapid neutron captures that happen to be faster than the competing radioactive decay of the produced isotopes. Theoreticians developed precise models of the nucleosynthesis and predicted it to occur in neutron-rich environments like neutron-star mergers [Fre99]. It has also been proposed that during this process a characteristic electromagnetic signal will be emitted, produced by radioactive decay of formed nuclei. In 2010 the first realistic prediction of this signal has been made within an international collaboration under the direction of G. Martinez-Pinedo and B. Metzger [Met14]. A luminosity 1000 times brighter than a nova was foretold, reaching its maximum after around one day. Based on that expectation this event has been named *kilonova*. Recently such a signal has been observed for the first time, showing the predicted emission patterns and thereby confirming the theoretical models [Pia17, Abb17, Dro17]. The quality of the latter is now limited by the low statistics since only one event has been observed so far. But also precise nuclear data of neutron-rich nuclei and their properties are required as they contribute to the understanding of nucleosynthesis.

Thus – especially with regard of the current developments – experiments aim for high-precision measurements of exactly these nuclei for investigating their fundamental properties to prove theoretical models. This includes the binding energy *BE(N,Z)*, that is a unique fingerprint of every nucleus and is an important characteristic since it is one of the dominant properties that determine the exact path of the r-process [Mol96]. Due to the mass/energy equivalent stated by Einstein it is inherently connected with the atomic mass. The binding energy can then be investigated by the difference between the experimentally determined atomic mass and the expected mass, given by sum of its constituent parts [Wei35]. Both depend on the number of neutrons N and protons Z with their mass m_N respectively m_p. Thus the binding energy is given by

$$BE(N,Z) = \left(Nm_n + Zm_p - m(N,Z)\right)c^2\,. \tag{1.1}$$

Accurate mass values contribute to a variety of fundamental studies including tests of the Standard Model and the weak interaction, since the mass represents the sum of all the nucleonic interactions [Lun03]. Differences of binding energies also give separation energies, providing clues to the shell structure. A common technique that is widely used to perform high precision mass measurements is the Penning-trap mass spectrometry [Bla06,Mar07,Elo09,Bre09]. It offers high sensitivity [Rod10] and can reach an accuracy below 10^{-9}. To improve this performance and thereby enable investigations of short-lived nuclides with low production rates a lot of progress has been made in the last years regarding the detection systems.

Besides this progress, further developments of new technologies and applications to an unprecedented degree are required to achieve an increasingly deeper level of knowledge about matter. Particle accelerators play an important key role within these research efforts, since they give access to the most exotic nuclei. For a major step into further investigations at the GSI Helmholtzzentrum für Schwerionenforschung, located in Darmstadt/Germany, an international accelerator center for intense, high-energy ion and antiproton beams [Col01] is currently under construction. This new center – called ***F****acility for* ***A****ntiproton and* ***I****on* ***R****esearch* (FAIR, sec. 1.1) – will comprise a new synchrotron, a fragment separator and several new storage rings among which different experimental setups will be installed. Especially with

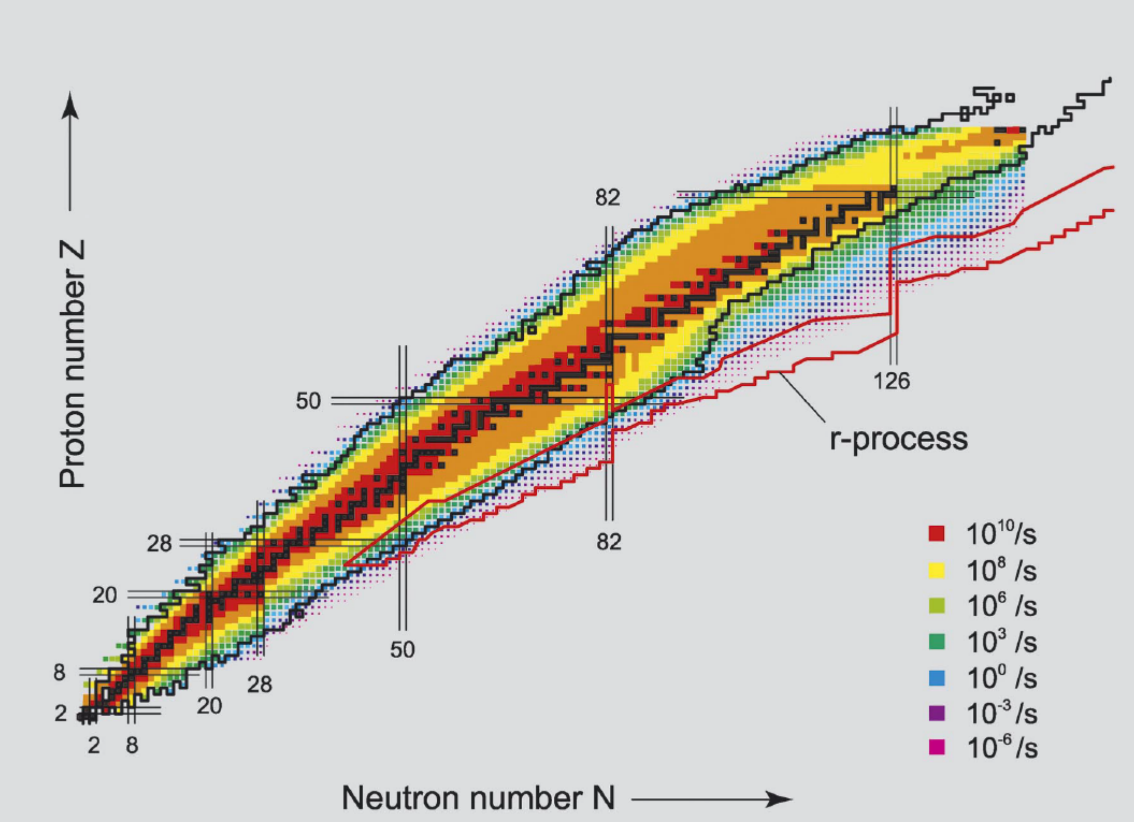

Figure 1.1: Predicted production rates at the proposed facility FAIR [Col01]. Only nuclides with half-lives >100 ns are depicted. The presumed path of the r-process is indicated in red.

regard to the recent scientific breakthrough, the future accelerator facility FAIR has been put into focus of prospective research since it enables the generation of those short-lived nuclei that create the electromagnetic emission observed during a kilonova (see fig. 1.1). One of the planned experiments at FAIR is a setup for *Precision **M**easurements of very short-lived nuclides using an **A**dvanced **T**rapping **S**ystem for highly-charged ions* (MATS) that will be installed at the low-energy beamline (sec. 1.1). It will allow to investigate nuclei far from stability and thereby deepen the knowledge about their fundamental properties.

Whilst FAIR is under construction, development platforms already exist in order to optimize the future experiments. The groups forming the MATS collaboration are among the world leaders in the field of Penning-trap mass spectrometry [Rod10]. One of these development platforms is TRIGA-TRAP [Ket08] that is located at the research reactor TRIGA Mainz. It serves as a prototype for the future MATS-setup that will primarily benefit from the progress made in experimental devices as well as measurement procedures. Thus the experience in construction and operation will considerably minimize the research and development efforts for MATS. TRIGA-TRAP is a double Penning-trap mass spectrometry experiment that on the one hand aims at detection of the nuclear mass of long-lived radioisotopes, e.g., in the region of the actinides. On the other hand, coupling of this setup to the research reactor enables the access to neutron-rich nuclides produced by neutron-induced fission of an actinide target, e.g., ^{235}U or ^{249}Cf. As their fission fragments are short-lived and hardly accessible, either only few data concerning their masses are available or the precision is insufficient. At TRIGA-TRAP fission products are extracted by an aerosol-based gas-jet (sec. 3.1), ionized in a surface ion source (sec. 3.2) and subsequently accelerated to 30 keV. Afterwards the generated ion beam is mass separated (sec. 3.4) and then collected in a radio frequency cooler and buncher (sec. 3.5), that prepares the ions for subsequent mass measurements within a Penning trap (sec. 3.7).

This thesis will discuss the progress of successful online coupling of TRIGA-TRAP to the nuclear reactor. Within this framework a surface ion source has been constructed to boost the ionization efficiency and thus the intensity of the subsequent ion beam. Its implementation and extended characterization (sec. 4.2) will cover the major part of this work in conjunction with efficiency studies of the beam line performance (sec. 4.1). Concluding this thesis the results of first mass measurements of fission products (sec. 4.3) will be presented.

1.1 The research facility FAIR

Even if plenty of knowledge about the basic building blocks of the universe has been gained during the past decades, there are still open questions, e.g., regarding the complex properties of matter. The future accelerator facility FAIR is intended to help solving the puzzle posed by the structure of matter. The scientific field that can be explored within FAIR comprises a wide spectrum [Gut06]. One research goal is to achieve comprehensive knowledge about all aspects of hadronic matter, including

the investigation of fundamental symmetries and interactions. Another research field is about many-body aspects of matter, governing the behaviour of matter as it appears in our physical world as well as on the hadronic level. The science fields split into the following collaborations:
(i) APPA Physics (**A**tomic, **P**lasma **P**hysics and **A**pplications)
(ii) CBM (**C**ompressed **B**aryonic **M**atter)
(iii) PANDA (Anti**p**roton **An**nihilation at **Da**rmstadt)
(iv) NUSTAR Physics (**Nu**clear **S**tructure, **A**strophysics and **R**eactions)
The latter concerns astrophysics, since elements heavier than iron originate from kilonovae. With rare isotope experiments relevant details of the nuclear configuration of the heavy element abundance or the interior of neutron stars shall be clarified. The NUSTAR collaboration comprises – amongst others – the Super-FRS (Superconducting Fragment Separator), LaSpec (Laser Spectroscopy) and MATS [Gut06]. FAIR will create highly intense ion beams and beams of antiprotons with precisely defined energies, thereby giving access to a wide range of new nuclei previously unavailable in laboratories or offering the possibility to study secondary beams of unstable nuclei. It is based on the experience and technological developments hitherto made at GSI in combination with newly developed innovative detector systems and experimental techniques. Its heart will be a superconducting synchrotron ring facility (SIS) connected with a system of cooler-storage rings and several experimental halls (see fig. 1.2). The Super-FRS will be the most powerful in-flight separator worldwide for exotic nuclei up to relativistic energies [Kes14]. Rare isotopes produced via projectile fragmentation of all primary beams up to ^{238}U and via fission of ^{238}U are spatially separated within a few hundred nanoseconds, thereby offering the chance to investigate very short-lived nuclei. These nuclei can either be guided into the high energy branch for reaction studies under complete kinematics or to the ring branch for investigation of, e.g., reactions of atoms with an internal target. The last option is the low energy branch (LEB), which is an experimental area of the NUSTAR collaboration. It is mainly dedicated to precision experiments with bunched beams consisting of very short-lived nuclei stopped in a gas cell.

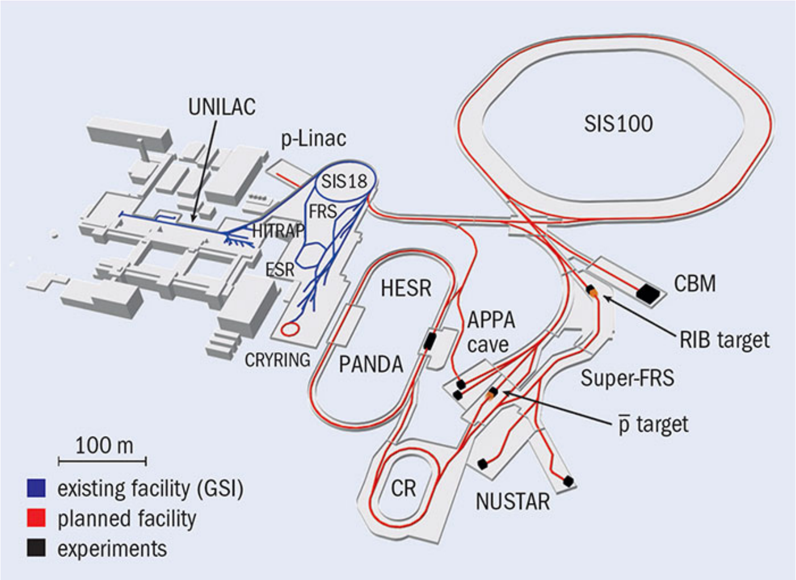

Figure 1.2: The existing facility GSI (blue) with the accelerators UNILAC, SIS 18 and ESR [BF17]. The future facility FAIR – indicated in red – comprises the super fragment separator (Super-FRS), a collector ring (CR) and a high-energy storage ring (HESR). The planned experiments are denoted in black. For details see text.

MATS at FAIR

The MATS experiment at FAIR will comprise high-precision mass measurements, decay studies within a Penning trap, in-trap conversion electron and α-spectroscopy [Rod10]. An overview of its experimental setup, which will be installed at the low energy branch of the Super-FRS, is shown in figure 1.3. The operation of MATS requires the thermalization of ions, thus a gas-filled stopping chamber will be placed in front of this experiment. It will provide a continuous ion beam, which is guided through a radio frequency multipole device, extracted and afterwards accelerated by a system of electrodes to several tens of keV. The energy spread is expected to be around 1 eV with an emittance of a few π mm mrad [Rod10]. For subsequent separation of the ion beam into individual masses, a double-focusing 60° dipole magnet will be deployed with a mass resolving power of $M/\Delta M = 500$. Two einzel lenses will be installed in front of the magnet to form a parallel ion beam. Beam diagnostics like a movable Faraday cup in combination with a multichannel plate detector or a tape station will be provided behind the magnet. These beam diagnostics enable a measurement of the beam composition and will permit a maximum transmission

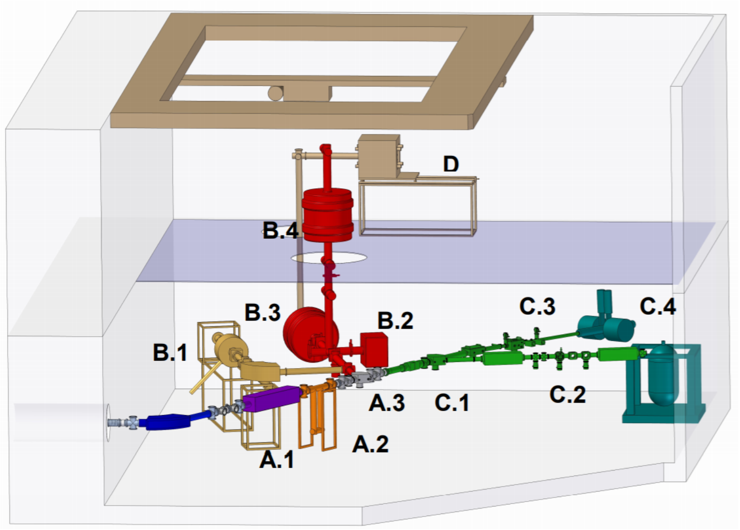

Figure 1.3: Overview of the MATS and LaSpec experiment setups planned for FAIR [Rod10]: The common parts comprise a buncher section (A.1), the multi-reflection time-of-flight mass spectrometer (A.2) and a switchyard (A.3). The EBIT junction is shown in yellow (B.1). The MATS beamline (red) consists of the off-line ion source (B.2) with the preparation trap section (B.3) and a subsequent measurement trap (B.4). The LaSpec beamline is represented in green. D is a setup for neutron decay spectroscopy.

into a subsequent RFQ cooler and buncher, which will be able to pulse down the ions to 2-3 keV. Further procedure depends on the usage of the ion beam: inserting the beam into a switchyard offers the chance to guide the ions either to the Penning-trap mass-spectrometer MATS or to the laser spectrometry experiment LaSpec. For commissioning and test operation of the RFQ a basic surface ion source shall be installed, which provides an ion beam of several nA. The installation of additional ion sources is also foreseen for acceptance trials of all subsystems. Ion beam preparation and manipulation is critical for low-energy studies of radioactive nuclei, since collisions between thermalized ions and buffer gas atoms can result in a poor quality ion beam with a large emittance [Gut06]. Thus the interaction of the prepared ion beam and the performance of the RFQ are crucial for adjacent investigations like ion trapping for mass measurements. Once the beam has been cooled and bunched inside the RFQ, it has to be accelerated again and transported to the experiments. In a first stage of the project, the preparation Penning trap as well as the measurement trap will both be housed in a superconducting 7 T-magnet with two homogeneous field regions, separated by about 200 mm, in a cryogenic environment of 77 K.

The Penning-trap system is currently under commissioning at TRIGA-TRAP and will later be installed at FAIR (B.3 in fig 1.3, [Rod10]). It will be used for mass measurements on singly charged ions via Time-of-Flight Ion Cyclotron Resonance (ToF-ICR) and narrow-band Fourier Transform Ion Cyclotron Resonance (FT-ICR) technique. In a next stage of the project, it will then be replaced by a system comprising a preparation Penning trap for highly charged ions (HCI) and a detector trap. In a future stage, an advanced electron beam ion trap (MATS-EBIT) will replace this Penning trap system in order to enhance the accuracy of mass determinations. This method uses an electron beam to produce highly charged ions in situ to enable novel investigations in a broad range of nuclear physics fields, e.g., studies of ground state properties. A detailed discussion of this aspect is outside of the rope of the presented thesis and can be found in [Ett13].

Chapter 2

Theoretical fundamentals

This section will give an overview of fundamentals that are crucial for this work. It will begin with an overview of radionuclide transport in gas-jets, since it is the first part of the experimental setup. Besides its principle this section comprises gas flow fundamentals, mechanisms of particle loss and basics of aerodynamic focusing. Afterwards the principle of surface ionization will be discussed since is used to convert fission products transported by the gas-jet into an ion beam. The subsequent section is about confinement of ions within electrostatic or magnetic fields. It concludes with a short introduction of different techniques for mass measurements of a single ion employed at TRIGA-TRAP.

2.1 Radionuclide transport in gas-jets

Modern research facilities like nuclear reactors or particle accelerators give access to exotic nuclides, e.g., neutron-rich, neutron-deficient or superheavy isotopes. They are of major scientific interest as their fundamental properties, e.g., the mass, binding energy or chemical behaviour are not sufficiently investigated yet. Their half-lives are generally short, hence it is crucial to apply a fast and efficient extraction method to transport the isotopes of interest to the experimental setup. Like several other online facilities, e.g., JAEA-ISOL [Sat13,Sat15b] and IGISOL [Moo13,Moo14], TRIGA-TRAP uses a so-called aerosol based gas-jet system to get access to short-lived nuclides produced by neutron induced fission inside of the reactor. These systems are widely used since the 1960s [Mac69,Maz81,Wie72], as they are predestined for a fast and efficient transport of radionuclides from their point of origin to separation or detection stages. A gas-jet system in general consists of three parts: The aerosol generator, the adsorption of radionuclides onto aerosol particles and their transport to a subsequent experiment. The addition of particles to a carrier gas is crucial to enable an efficient transport of radionuclides and avoid particle losses due to diffusion processes. Gas-jet systems are suitable for radionuclides with half-lives of at least several seconds, can be continuously operated and do neither require high temperatures or high voltages. As it is an important part of the TRIGA-TRAP setup, individual stages of a gas-jet will be introduced and fundamental parameters that affect its performance will be discussed in this section.

The first part of a gas-jet is the generation of an aerosol. It can be produced by different techniques, e.g., generating an electric arc between electrodes consisting of carbon [Eib09] or metals, atomization of aqueous salt solutions [Zud86] or vaporization of inorganic salt in a heated oven [Sat13,Ket08]. The latter is the method of choice at TRIGA-TRAP as it ensures contaminant free aerosols and high transport efficiencies over several meters [Maz81,Wol76,Sat15b].

Based on previous gas-jet investigations at TRIGA-TRAP cadmium(II)-iodide (CdI_2) has been employed as aerosol material and nitrogen as carrier gas [Gru14]. The latter offers the advantage of a comparably high stopping power and low neutron-capture cross section, i.e., a low activation inside the reactor. Cadmium iodide is placed in a small vessel located inside the oven that is heated to a temperature that is around 100 °C below the melting point of CdI_2 (MP: 387 °C [Hay14]). It is high enough to sublimate an adequate number of molecules but still prevents the salt from fusing, thereby reducing the surface of the salt and thus the number of sublimated particles. The number as well as the diameter of the produced aerosol particles strongly depend on both the temperature and the gas flow rate. Typical size distributions at different gas flow rates are shown in fig. 2.1. A decrease of the gas flow shifts the maximum of size distribution to larger diameters due to increased agglomeration. The conditions employed at TRIGA-TRAP are an oven temperature of 290 °C and a nitrogen gas flow rate of 400 ml/min (STP). It was shown that this combination of parameters produces aerosol particles with a mean diameter of 61.0(1) nm [Gru16], which yields a maximum extraction or transport efficiency.

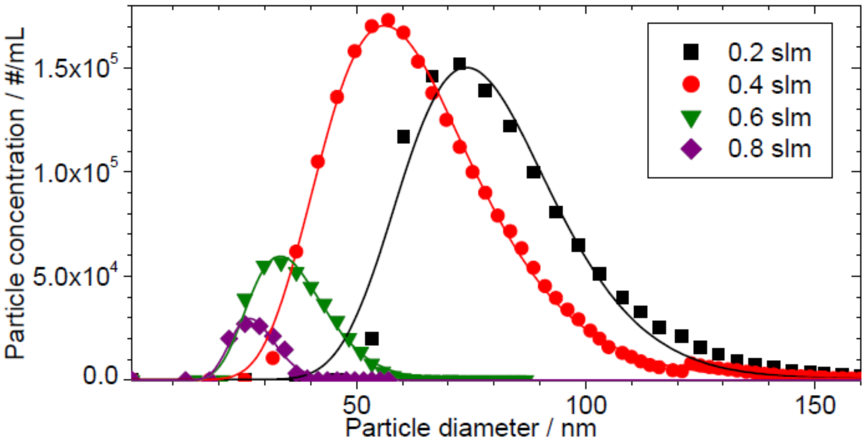

Figure 2.1: Size distributions of CdI_2 aerosol particles in dependence on the gas flow rate [Gru16]. The oven temperature has been kept constant to 290 °C. The solid lines are lognormal distributions fitted to the data.

The second part of a gas-jet is the adsorption of radioactive nuclides on the aerosol particles. A fissionable target is placed inside a stopping chamber that is large enough to ensure the thermalization of fission fragments and simultaneously small enough to enable its installation inside a beam port and keep the flush-out time short. Radionuclides produced by neutron induced fission of ^{235}U have kinetic energies of about 70 MeV to 100 MeV [Gib61], thus, when directly recoiling out of the target, they have a range of a several centimeters in N_2 gas at atmospheric conditions until they are thermalized and can adsorb on the aerosol particles. As the required stopping power depends – amongst others – on the material density inside the chamber, it can be regulated via the pressure and that in turn by the gas flow rate. It has to be adjusted carefully as low flow rates might not be sufficient to thermalize the radionuclides whereas high flow rates could create losses due to turbulences. It also has to be considered that the gas flow not only changes the pressure inside the stopping chamber, but also affects, e.g., the transport efficiency, transport time or – as mentioned above – the size of aerosol particles. After the thermalization process, fission products attached to aerosol particles are transported within the carrier gas to subsequent components, which represent the last part of a gas-jet.

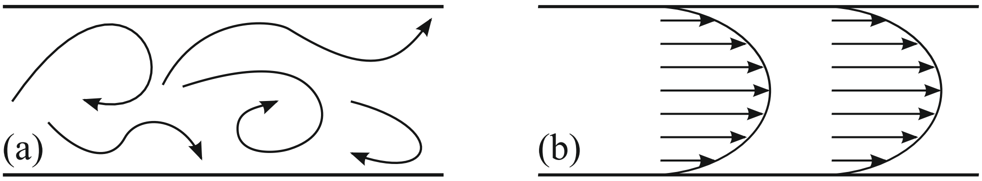

Figure 2.2: A turbulent flow is characterized by highly irregular stream lines (a) whereas stream lines of a laminar flow are parallel (b). Due to the higher friction towards the outer areas a parabolically shaped velocity profile is created.

Particle transport in tubular flows

To estimate particle losses or get information about the particle distribution within the gas-jet, the behavior of the gas stream itself has to be investigated. Various aspect have to be considered and will be discussed within this section. If not otherwise noted, the formalism follows W. Hinds [Hin12] and R. Bahreini [Bah08]. In general aerosol particles follow the gas stream lines that describe the direction of the gas flow. As the velocity of the gas exceeds certain values, e.g., due to tube tapers, eddies and oscillations occur, thereby mixing the separate layers, i.e., producing a turbulent flow (fig. 2.2 (a)). When the aerosol velocity is low, the flow is laminar, i.e., the bulk material moves as distinct layers and the only movement across these layers is the molecular motion that creates viscosity (fig. 2.2 (b)). The friction that the gas molecules experience within a tube increases from the center to the capillary walls and thereby influences their motion. It results in a parabolic velocity distribution, also called Poiseuille flow, i.e., the velocity within the center of the tube is approximately twice as large as the average velocity, whereas it is zero at the walls. The nature of the gas flow can be characterized by the Reynolds number Re that is given by

$$Re = \rho \cdot \nu \cdot D/\eta \tag{2.1}$$

with the density of the gas ρ, its velocity ν and viscosity η. D is the inner diameter of the tube. The flow is laminar for $Re < 1000$ and becomes turbulent for Re > 2100. The general transport by an aerosol requires the consideration of interactions between particles and the surrounding carrier gas. As properties of the aerosol, e.g., density, viscosity or pressure, are in principle those of the pure gas, the interactions on a microscopic scale have to be taken into account, thereby investigating the behavior of a single particle. One important parameter is the relaxation time τ that characterizes the time an embedded particle needs to react to a sudden change of outer forces, e.g., an obstacle. It is proportional to the particle diameter d_p and its density ρ_p and thus depends on the mass of the investigated particle:

$$\tau \propto \frac{\rho_p d_p^2}{\eta} \,. \tag{2.2}$$

η describes the viscosity of the surrounding gas and depends therefore on pressure and temperature. The general ability of particles to follow the surrounding stream is described by the Stokes number *St*. It is defined by the ratio of the particles relaxation time τ to a characteristic dimension of the investigated obstacle. In tube systems with a circular cross-section the tube diameter d_c is used as characteristic dimension. Then the Stokes number is given by

$$St = \frac{\tau \cdot v_0}{d_c} \tag{2.3}$$

Small particles with negligible masses ($St \gg 1$) follow the streamlines almost perfectly, whereas large and heavy particles ($St \ll 1$) tend to retain their initial trajectory independent from the gas flow.

Mechanisms of particle loss

A gas-jet typically consists of a combination of several capillaries, tapers and bendings. Since there are many sources of particle loss, the total length of the system should be kept as short as possible to minimize the overall losses respectively to maximize the transport efficiency. Considerable mechanisms that lead to losses of various extents are diffusion, gravitational sedimentation and impactions onto capillary walls caused by turbulences or by abrupt curvatures. The total transport efficiency η_{tot} is then given by

$$\eta_{tot} = \eta_{diff} \cdot \eta_{grav} \cdot \eta_{turb} \cdot \eta_{bend} \,. \tag{2.4}$$

The individual partial efficiencies and their origin are discussed in the following.

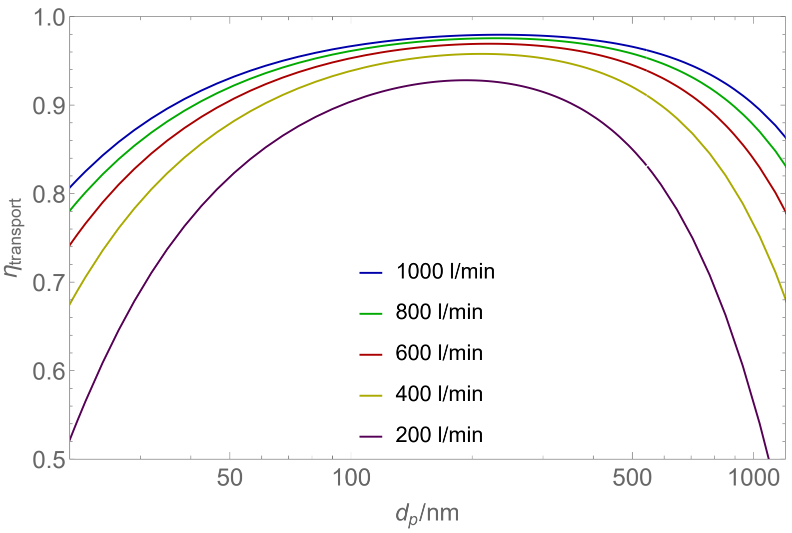

Figure 2.3: Particle losses caused by diffusion (eq. 2.5) and sedimentation (eq. 2.6) at different gas flow rates and an N_2 pressure of 1 bar, shown for CdI_2 as aerosol material. The length of the capillary (inner diameter = 0.86 mm) was set to 10 m.

As aerosol particles adsorb on the capillary wall in the moment of contact, their concentration in the stream decreases from the axis to outer regions. At the capillary wall itself the concentration is zero. Thus a constant diffusion from inner particles to the walls occur and reduces the total amount of particles within the carrier gas. The remaining transport efficiency can be estimated by

$$\eta_{diff} = exp\left(-\frac{\pi d_c L v_{diff}}{Q}\right) . \tag{2.5}$$

Q describes the gas flow through a tube with the total length L and the diameter d_c. v_{diff} denotes the velocity of particle loss caused by diffusion. The concentration gradient, and with that the diffusion velocity to the capillary walls, increases with smaller capillary diameters. Furthermore, particle losses increase when the particle diameter is smaller than 50 nm or larger than 400 nm (see fig. 2.3). Whereas losses due to diffusion dominate at smaller particle diameters, sedimentation becomes more dominant for larger particles. The transport efficiency that expresses the loss due to gravitational sedimentation can be predicted by

$$\eta_{grav} = exp\left(-\frac{d_c L v_{sed} cos\theta}{Q}\right) \tag{2.6}$$

with the velocity of sedimentation v_{sed} and the inclination angle of the capillary θ. Correspondingly the transport can be maximized by selecting a high gas flow rate, a short capillary or a small capillary diameter. Nevertheless, the main source of losses are turbulences due to perturbations of the laminar flow, e.g., at transitions from one capillary diameter to another. The recirculation of the gas creates turbulences and thereby pushes the axial flow onto the curvatures outer face. Thus the diameter of the capillary plays an important role. The induced losses increase with larger particle mass as well as larger Reynolds number. The transport efficiency can then be estimated by:

$$\eta_{turb} \propto exp\left(-\frac{\pi d_c L Re St^2}{Q}\right) . \tag{2.7}$$

Furthermore, these losses are intensified by the Brownian motion. Additionally significant losses occur because of particle impactions onto the capillary walls at abrupt bendings, e.g., at switch points. Assuming a laminar flow, the transport efficiency is given by

$$\eta_{bend} = \left[1 + \left[\frac{St}{0.171}\right]^{0.452 \cdot \frac{St}{0.171} + 2.242}\right]^{-\frac{2\varphi}{\pi}} . \tag{2.8}$$

φ denotes the bending radius of the curve. The transport efficiency reaches its maximum with a laminar gas flow and Stokes numbers below 0.05. Thus abrupt bendings should be avoided in order to reduce losses caused by impacts.

Basics of aerodynamic focusing

A gas-jet guides aerosol particles to subsequent experimental devices that are usually operated in vacuum. The transition between these regions of different pressure is intricate as the aerosol expands as it leaves the capillary and enters the vacuum. Thereby the opening angle of light gas molecules is significantly larger than that of the heavy aerosol particles. However, as the working conditions usually require a low pressure, the carrier gas has to be removed while the aerosol particles should be

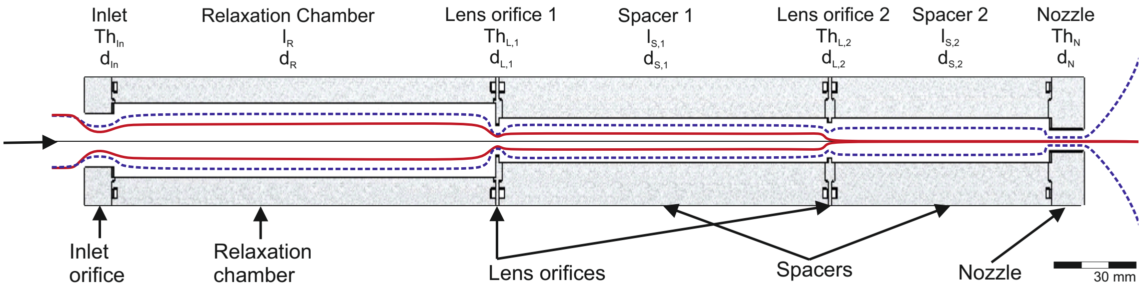

Figure 2.4: Section view of an aerodynamic lens with labeled components [Gru16]. The trajectory of the carrier gas is depicted in dashed lines. The aerosol particle trajectory (red) is collimated by each lens orifice thereby reducing its opening angle.

preserved. Commonly, pumping barriers with a small orifice are inserted. Whereas heavy particles pass the orifice, the carrier gas can be pumped away. To maximize the transmission of aerosol particles through the small aperture it is useful to reduce their opening angle. Aerodynamic focusing is a widely used principle to generate a collimated beam of particles that neither possess an electrical charge nor a magnetic moment. Collimation allows to sustain a narrow particle beam over a long distance. To enable aerodynamic focusing, the flow has to be laminar, subsonic and behaving as a continuum. An unstable flow would generate turbulences, thereby destroying any focussing. An aerodynamic lens employs several stages of focusing as depicted in fig. 2.4. Aerosol particles enter it through an inlet that determines the mass flow inside the lens system. It is followed by a relaxation chamber and subsequent focusing lens orifices separated by spacers. The nozzle accelerates the gas flow to its final velocity. By passing the relaxation chamber or each spacer, the gas expands and is thereby decelerated. The inner diameter of the lens orifices are smaller, thus the gas flow comprising the aerosol particles is accelerated. An alternately converging and diverging gas flow arises. The resulting gas stream lines and the trajectory of heavier aerosol particles are depicted in fig. 2.4. During each acceleration stage, they are pushed towards the axis but do not follow the gas stream lines thoroughly during the subsequent deceleration. Thus with each step their trajectory is shifted to the central axis and their opening angle is reduced simultaneously. The degree of particle collimation strongly depends on their mass or size and thereby on their Stokes number. The latter is also affected by the tube diameter (see eq. 2.3), thus it decreases in regions of contraction and increases after subsequent expansion. Aerodynamic focusing occurs for particles with $St > 1$ within the regular flow and $St < 1$ during contraction. The Stokes number of larger particles is $\gg 1$ at all times, thus they are not affected by the gas streamlines. Small particles with diameters below 25 nm tend to follow the gas stream lines and are thus hard to collimate. Particles with diameter above 2500 nm are too inert to follow the stream lines, thus a major part of them gets lost due to impacts onto the orifices.

Typically particles in the range of 25 nm to 250 nm are focused into a narrow beam by a series of three to five lenses [Wan06]. The design of most lens systems employed today is similar to that introduced in [Liu95b]. Besides the particle size, the gas flow rate and the pressure up- and downstream of the lens are crucial for the performance of the lens [Zha04]. The original aerodynamic lens design operated at a pressure of around 2 mbar with a pressure drop of around 50 % across an orifice [Liu95a]. However, the design of an aerodynamic lens has to be adapted to the given experimental conditions, as its collimation ability is strictly limited to a certain set of operation parameters. As one or more conditions are changed, dimensions of the lens have to be readjusted, e.g., the length of the spacers or the inner diameter of the orifices.

2.2 Surface ionization

Since several decades ion sources play an important role, e.g., in ISOL (Isotope Separation On Line) facilities. Different types have been employed for various applications like ion implantation or nuclear spectroscopy [Bey71, Man13, Joh73, Kir81, Bro04]. Within this work, the technique of surface ionization inside a hot cavity will be discussed since it is a major part of this work. That type of ion source is widely used at ISOL facilities, where it is crucial to form a radioactive ion beam for subsequent experiments. Although competing techniques have come up in the last decades, surface ionization is still in use and developments and optimizations are ongoing [Kir03, Kös08, Sto13]. Characteristic features of this kind of ion sources are high working temperatures and small dimensions of the ionization chamber. One of the most essential advantages is the purity of the produced ion beams, which are free of multi-charged or residual gas ions. Furthermore the amount of required atoms is rather low as well as the energy spread of the produced beam. Additionally they offer high ionization efficiencies with simultaneously short residual times of the ions inside the hot cavity, which is essential for short-lived nuclei [Tur12]. Surface ion sources are not only used for producing an ion beam of radioactive nuclei, but also as a tool for measurement of fundamental atomic properties. For instance the first ionization potential of an element can be determined to gain direct information about the binding energy of an electron in the outermost orbital of an atom. The ionization potentials of heavy nuclei are of major interest since not all electron configurations are known. Lately an important progress has been made by the investigation of the first ionization potential of the heaviest actinide lawrencium [Sat15a]. A surface ion source can also be used for determination of adsorption enthalpies of selected elements on a chosen material.

The physical process of thermal ionization takes place on a solid surface that is heated to temperatures above 1200 °C. An atom adsorbs onto the hot surface for a certain duration that is long enough to reach thermal equilibrium (typically 10^{-5} s to 10^{-3} s). The ionization efficiency I_{eff} that denotes the degree of ionization, is given by the ratio between the number of ionized atoms n_+ and total number of atoms before ionization n_0. It strongly depends on the temperature T of the hot surface and declines rapidly below a certain temperature. The latter is material dependent and describes the energy required for an electron to escape a solid surface. The ionization of alkali metals on tungsten surfaces has been studied extensively since the pioneering researches of Langmuir et al. [Lan25], who conceived the well known Saha-Langmuir equation for determination of ionization efficiencies [Dre68, Zan59, Dat56, Kir81]:

$$I_{\mathit{eff}} = \frac{n_+}{n_0} = \frac{g_+}{g_0} \cdot \exp\left(\frac{\varphi - IP}{k_B T}\right) \tag{2.9}$$

Here, g_+ and g_0 denote the statistical weights of the investigated element species in its ionic or atomic state, k_B the Boltzmann constant and IP represents the ionization potential of the observed element. The state of an evaporating particle is also determined by the probability of an incident beam atom reaching equilibrium with the surface. This probability can be taken into account by the insertion of a reflection coefficient for the incident atom, but can be neglected in the case of alkaline metals on tungsten. In this case particle reflections do not occur due to numerous vacancies in the band structure 6s^2 5d^4 of tungsten [Dat56]. The Saha-Langmuir equation can also be corrected for low lying excited states of the particles. Unfortunately it cannot consider the presence of chemical reactions, the presence of unknown contamination on the surface or the lack of thermal equilibrium.

In the case of hollow tube surface ion sources, the experimentally observed ionization efficiency can reach much higher values than expected from eq. 2.9. It can be explained if charged particles are confined in a potential well created inside the hollow tube and therefore prohibited from further wall contacts and re-neutralization [Kir90]. Based on the Saha-Langmuir equation an analytical method [Sat15a] describes this process in a hollow tube type ion source. The ionization efficiency I_{eff} can then be expressed as:

$$I_{\mathit{eff}} = \frac{N \cdot \exp\left(\dfrac{\Phi - \mathrm{IP}_1^*}{k_B T}\right)}{1 + N \cdot \exp\left(\dfrac{\Phi - \mathrm{IP}_1^*}{k_B T}\right)} \tag{2.10}$$

The parameter N depends on the mean number of wall collisions κ a particle undergoes in the cavity before escaping through the exit orifice. It has to be taken into account that not every ionized particle leaves the cavity as an ion. This happens with a probability $\rho < 1$, which considers that a particle may not be trapped at all in the volume or that a confined ion has the chance to discharge at the surface walls again. Thus, N can be denoted as the effective number of atom-surface interactions that neutral particles undergo in the cavity, given by $N = \kappa \cdot \rho$. The effective ionization potential IP_1^* is related to the the ionization potential IP by

$$\mathrm{IP}_1^* = \mathrm{IP}_1 - k_B T \ln\left(\frac{Q_+}{Q_0}\right) \tag{2.11}$$

with the partition functions Q_+ and Q_0 at a given temperature that can be calculated by

$$Q_{+/0} = \sum_j g_{+/0}^j \cdot \exp\left(\frac{E_{+/0}^j}{k_B T}\right) . \tag{2.12}$$

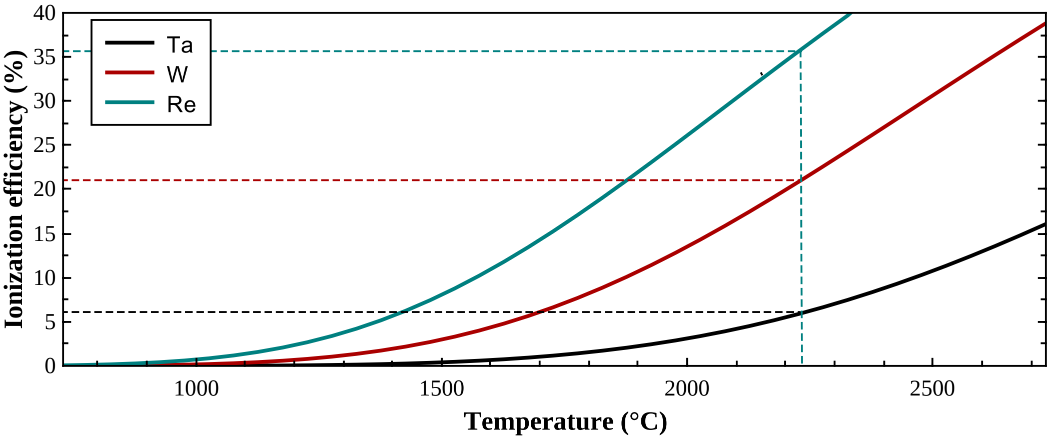

Figure 2.5: Dependence of the ionization efficiency of strontium on different ionizer materials, calculated by eq. 2.10. The number of atom-surface interactions N has been set to 50. The higher the work function of the refractory metal(Ta: 4.25 eV; W: 4.54 eV; Re: 4.72 eV), the more efficient the ionization of strontium.

g_+ and g_0 are the statistical weights of the j^{th} quantum state of the ion respectively the atom with the energies E_+^j. Excited states whose excitation energies are much higher than k_BT can be neglected since the exponential term is approaching zero. The electronic ground state of alkaline metal atoms is a doublet state, hence its statistical weight is 2 and its ratio of w_+/w_0 is 1/2 [Dat56]. The analogue statistical weight of alkaline earth metals is 1.

The concept of surface ionization involves the interaction between a low ionization potential element and a high work function surface that is hot enough to desorb the ions thermally. According to eq. 2.9, the $\Phi - IP^*$ difference and thus the choice of ionizer material is decisive as it defines the magnitude of ionization efficiency. The combination of alkaline metals with comparably low ionization potentials around 4 eV to 5 eV and refractory metals as ionizer materials such as W, Mo or Ta promises adequate ionization efficiencies. Figure 2.5 shows the ionization efficiency of strontium for the ionizer materials tantalum ($\varphi = 4.25\,\mathrm{eV}$), tungsten ($\varphi = 4.54\,\mathrm{eV}$) and rhenium ($\varphi = 4.72\,\mathrm{eV}$), calculated by eq. 2.10. These materials have been selected because they were employed at most of the various ion source facilities and also have been used during former commissioning experiments at TRIGA-TRAP. The difference between the ionization potential of strontium and the work function of the ionizer material increases in the order Ta<W<Re and the number of generated

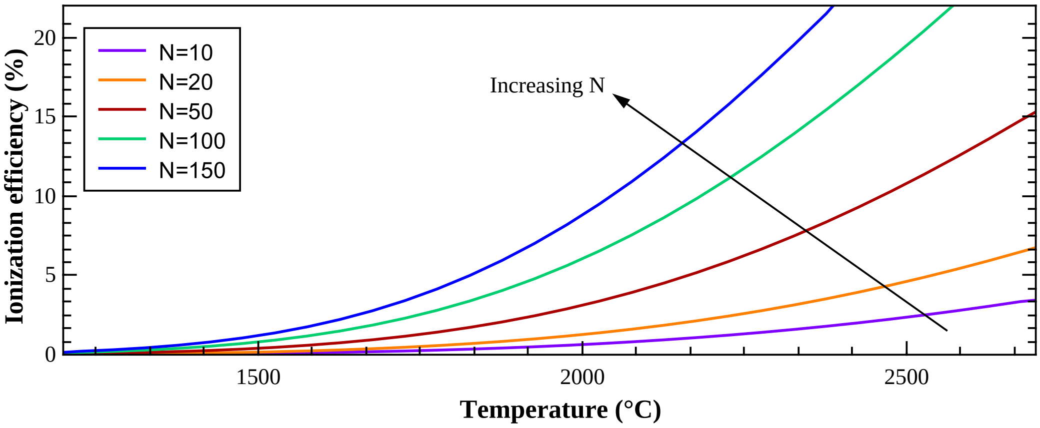

Figure 2.6: Ionization efficiency of strontium on a tantalum surface in dependence on the temperature. The effective number of atom-surface interactions N has been set to values in the range of 10 to 150.

ions rises correspondingly. Although the work functions of the considered elements are similar, the difference of their ionization efficiency is substantial. It deviates by several percent already at low temperatures, reaching a difference of a factor 3.5 between tantalum and tungsten and a factor of 6.1 between tungsten and rhenium at 2230 °C, respectively. If the ionization potential of the investigated species is too high or rather higher than the work function of the hot cavity, the main fraction of atoms entering the ionizer remains neutral. In general the process is assumed to produce only singly charged ions, since the second ionization potential is usually significantly higher than the first one. The other key parameter that determines the ionization efficiency is the effective number of atom-surface interactions N. It depends on several parameters, e.g., the temperature, the surface material of the ionizer or the geometrical configuration of the ion source. The magnitude of N affects the ionization efficiency slope, as indicated in fig. 2.6. The amount of ionized particles rises with increasing N. As this value depends on the exact geometrical configuration of the ion source it differs within each operation or even the temperature. Thus it has to be estimated for each measurement series, but is usually in the range of 30 to 100 for the type of ion source used within this work and by T. K. Sato et al. [Sat15a, Sat17].

Figure 2.7 depicts the ionization efficiency for different elements on a tantalum surface. The selected ion species are available at the TRIGA-TRAP experiment

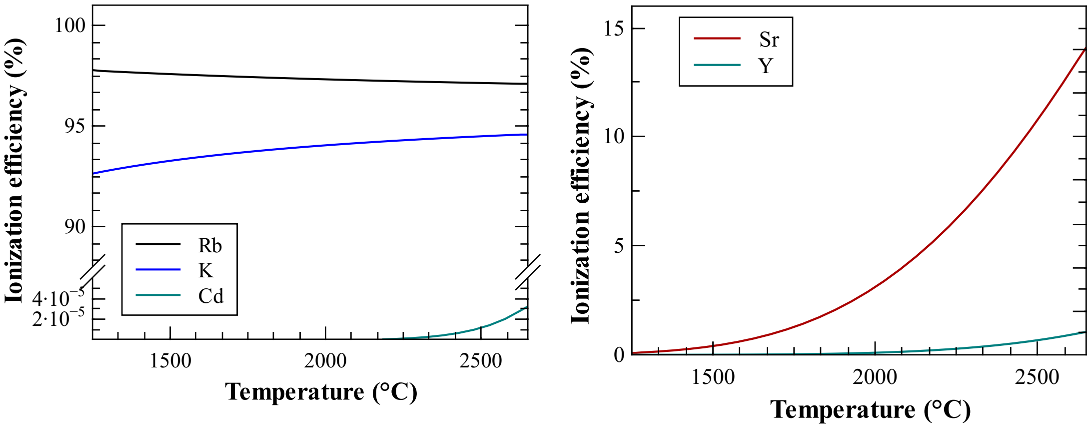

Figure 2.7: Ionization efficiency of different element species on a tantalum surface in dependence on the surface temperature. N has been set to 50.

and have comparably low ionization potentials (table 2.1). Except for rubidium, the ionization efficiency increases with rising temperature. As the effective ionization potential IP^* increases with the temperature, the difference to the work function of tantalum decreases. In the case of rubidium, this difference is small at low temperatures and finally vanishes above 1000 °C. Accordingly the fraction of non-ionized atoms increases.

Table 2.1: Ionization potentials (IP) of selected elements [Hay14].

Element	IP (eV)
Rubidium (Rb)	4.18
Strontium (Sr)	5.70
Potassium (K)	4.34
Yttrium (Y)	6.22
Cadmium (Cd)	8.99

2.3 Particle trapping

Electrically charged particles can be trapped in an electrical field configuration that possesses a potential minimum at some point in space. The corresponding forces then have to direct towards that point from all three dimensions. Following the Maxwell equations, it is not possible to create an electrostatic field minimum without the presence of electrical charges, i.e., it is not possible to create a field minimum in the free space between electrodes. One option to avoid this limitation is the application of an oscillating electric quadrupolar field in an adequate geometry to create an effective field minimum. This type of construction has been introduced by Wolfgang Paul and Hans Georg Dehmelt, who received the Nobel price in 1989 for "the development of the ion trap technique". Another method is the superposition of a static electric quadrupolar field with a homogeneous magnetic field. This configuration is called *Penning trap* and has been developed by Hans Georg Dehmelt. Nowadays it is widely used for determination of atomic masses or other fundamental properties, e.g., the g-factor [Stu13]. Since both techniques are employed at TRIGA-TRAP for different purposes, sketches of their working principles will be briefly discussed in the following sections.

2.3.1 Electrodynamic Paul-trap

Paul traps are well known and widely used in nuclear physics and spectroscopy as they offer a simple way to confine electrically charged particles. Such a trap consists of a ring electrode and two endcaps with hyperbolical shape, see fig. 2.8 (a). Applying an alternating voltage with a high frequency between the ring electrode and the two endcaps creates an oscillating quadrupole field. Ions inside this electrode configuration experience oscillating forces with the chosen field frequency: focusing ones in radial direction and simultaneously defocusing in axial direction, in alternation with the opposite. By choosing the frequency and amplitude in a specific parameter range for a given m/q, the time-averaged forces can create an effective focusing of ions all three dimensions [Pau90]. The linear Paul trap uses a different design that offers a higher ion storage capacity, but is still based on the same principle. It consists of four hyperbolically shaped rods arranged parallel to each other around a centered axis (see fig. 2.8, (b)). Each rod is split into three or more segments that are separated from each other by electrical insulators. By application of an RF voltage between adjacent rods a quadrupole field is formed thereby creating a dynamical radial confinement of inserted ions (see fig. 2.8, (c)). At the same time, axial confinement is reached by applying DC voltages to the rod segments in a way that a potential well is formed.

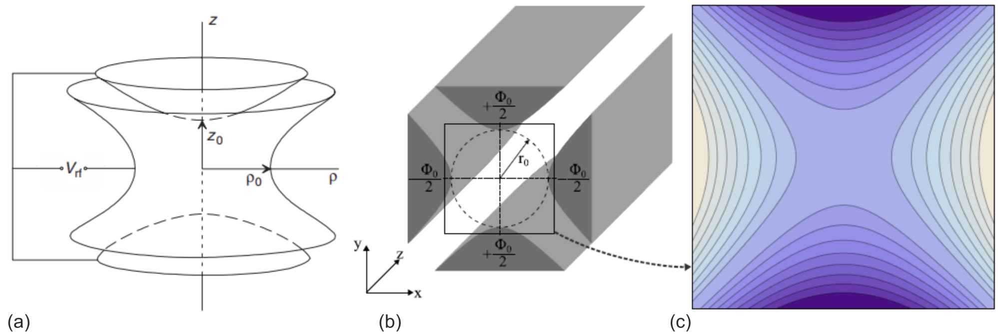

Figure 2.8: Electrode configuration of (a) a hyperbolically shaped Paul trap, adapted from [Bla06] and a linear Paul trap [Bey14a]. In (c) the equipotential lines of the quadrupole potential between the hyperbolical electrodes is shown.

Buffer gas cooling

The combination of a linear Paul trap with collisional cooling is called a radio frequency quadrupole (RFQ) beam cooler. It offers the possibility to reduce the emittance of a particle beam. Therefore, the Paul trap is filled with a light, neutral and inert gas – usually He – to reduce the kinetic energy of an incoming ion ensemble, effectively reducing their "temperature" to the temperature of the buffer gas. Confined particles are thus thermalized via multiple weak, elastic collisions with the cooling gas that has a lower temperature. Each ion-gas contact leads to an energy transfer and thus the equilibration of the ion temperature to that of the gas. The latter is obviously the lower temperature limit that can be reached by this technique. Simultaneously the energy spread of the ion ensemble is reduced, thereby improving their subsequent transport through a connected experimental setup. This enables studies on species available at comparably low rates. As the cooling takes place in a confining field, the thermal diffusion that results from atom-ion interactions is counteracted and a narrow ion beam is generated.

2.3.2 Magnetostatic Penning-trap

Instead of oscillating electric fields, a static magnetic field is used in a Penning trap to confine charged particles in three dimensions. The design of such a trap looks similar to that of a Paul trap and is employed at TRIGA-TRAP in both hyperbolical and cylindrical structure. The former consists of three hyperbolically

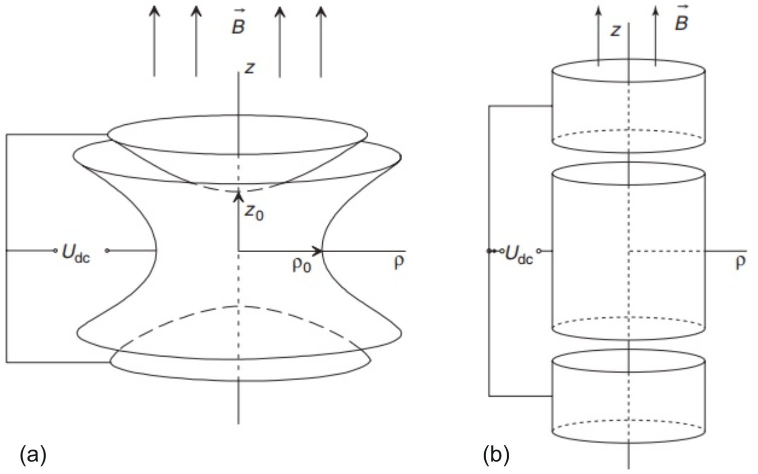

Figure 2.9: Electrode configurations of Penning traps [Bla06]. They consist of two end electrodes and a centered ring electrode that is either cylindrically or hyperbolically shaped.

shaped electrodes: a ring-electrode and two identical endcaps (see fig. 2.9(a)). On the contrary a cylindrical Penning trap is formed by three cylindrically shaped electrodes (see fig. 2.9(b)). The size of such a trap – independent from its shape – depends on its application purpose and is usually in the range of several millimeters up to a few centimeters. Both designs offer advantages: whereas the field is uniform in a larger volume in hyperbolical Penning traps, a cylindrically shaped Penning trap is easier to manufacture. However, independent from their design, a Penning trap is placed within a strong and homogeneous magnetic field. An electrical voltage is then applied between the ring electrode and the end caps.

Ion motions in a Penning trap

An ion that is guided into a homogeneous magnetic field $\vec{B}$ with its velocity $\vec{v}$ is deflected with a force perpendicular to the field lines. This force is named *Lorentz force* and can be expressed by $F_L = q\vec{v} \times \vec{B}$. In a homogeneous field it acts as centripetal force, leading to the so-called free cyclotron frequency

$$\omega_c = \frac{q}{m} \cdot \vec{B} \tag{2.13}$$

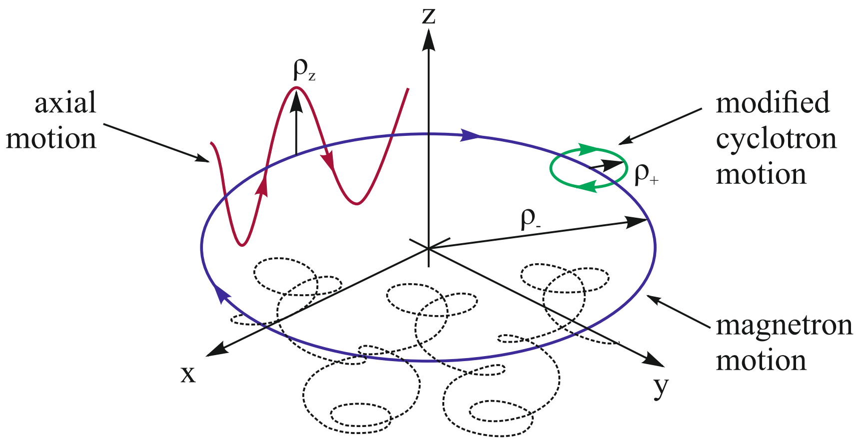

Figure 2.10: Sketch of the ion motion in a Penning trap adapted from [Rep12] with the magnetic field aligned to the z-axis. The ion motion can be resolved into three independent eigenmotions: Modified cyclotron (green), magnetron (purple) and axial motion (red). The dashed line shows the superposition of all three eigenmotions with their amplitudes ρ_+, ρ_- and ρ_z.

for a ion with a mass-to-charge ratio m/q. It describes the frequency with which a particles orbits around a magnetic field line. If the particle has kinetic energy axial to the magnetic field lines, it follows the field line in an helical trajectory. In a Penning trap, this is prevented by a trapping potential between the ring electrode and the end caps. With a hyperbolical shape of the electrode, the superposition of magnetic and electric field results in an ion motion as shown in fig. 2.10 (dashed line). It can be resolved into three independent eigenmotions, two radial motions and one axial motion. The axial motion of the ion is independent from the magnetic field strength and can be described as a classical harmonic motion with the frequency

$$\omega_z = \sqrt{\frac{qU_0}{md^2}}\,. \tag{2.14}$$

Here, d is the so-called trap parameter, determined by the minimal distance between the center of the trap and the end caps. The superposition of the magnetic field with the electrostatic quadrupolar field influences the radial motion of the ion. The decrease of the centripetal force results in two circular motions with frequencies

$$\omega_+ = \frac{1}{2}(\omega_c + \sqrt{\omega_c^2 - 2\omega_z}) \tag{2.15}$$

and

$$\omega_- = \frac{1}{2}(\omega_c - \sqrt{\omega_c^2 - 2\omega_z})\,. \tag{2.16}$$

These motions are named reduced cyclotron motion ω_+ and magnetron motion ω_-. The magnetron motion is in leading order independent from mass or charge of the ion, and can thus be assumed constant in most cases. For ideal Penning traps the mentioned eigenfrequencies are simultaneously connected via

$$\omega_c = \omega_+ + \omega_- \tag{2.17}$$

and

$$\omega_z^2 = 2\omega_+\omega_-\,. \tag{2.18}$$

In real Penning traps, with imperfections in the geometry or field configuration, eq. 2.17 no longer holds true and one has to use the so-called invariance theorem [Bro86], to connect the frequencies:

$$\omega_c^2 = \omega_+^2 + \omega_-^2 + \omega_z^2\,. \tag{2.19}$$

Thus, with eq. 2.17 or eq. 2.19 the cyclotron frequency of a free particle can be determined by measurement of the eigenmotions of the same trapped particle. Furthermore, if the magnetic field strength and the charge of the particle is known, the free cyclotron frequency can be used for measuring the particle mass.

Ion motion manipulation

The radii of individual motions can be selectively manipulated by the use of radio frequency fields. These are typically directly applied to the trap electrodes to create dipolar or quadrupolar fields, which in case of the circular motions requires to split the ring electrode into several segments. Dipolar RF fields affect the eigenmotion in resonance whereas quadrupolar fields at the sum of two eigenfrequencies couple the two eigenmotions. The former increases or decreases energy in the motion and the latter continuously converts energy between the two coupled motions. Thus, ion motion manipulation can be used to determine the eigenmotion frequencies. A dipolar excitation is applied, e.g., to determine the frequency of the magnetron motion. The ions transmitted through the small end cap orifice of the Penning trap are counted by a subsequent detector. Resonant excitation enlarges the radius of the magnetron motion – independently from the ion species. Thus the magnetron frequency can be determined by varying the excitation frequency until the transmitted ion rate is minimal.

The combination of dipolar and quadrupolar excitation with a small amount of inert gas leaking into the trap can be used for so-called resonant buffer gas cooling, which offers mass selection as well as ion centering [Sav91, Kre08a]. It exploits the occurrence of collisions between gas molecules and trapped ions, during which excitation energy of the ions is transferred to the surrounding gas. This technique can also be used for low-precision measurements of the cyclotron frequency as well as for removing isobaric contamination inside the trap with a high resolving power. While the axial motion behaves like a damped oscillator [Kre08b], the remaining eigenmotions are manipulated by applied electrical fields. Initially, all trapped ions are excited to a magnetron motion by a dipolar RF excitation pulse at the magnetron frequency ω_-. Afterwards, a second quadrupolar RF pulse with ω_{RF} is applied. If this frequency equals the sum of the magnetron frequency ω_- and the modified cyclotron frequency ω_+, the two motions are coupled to each other and kinetic energy is transferred from one to the other and vice versa. Because ω_+ is much larger than ω_-, orbital velocities are larger and kinetic energy is much faster dissipated by collisions with the buffer gas. Therefore the energy conversion between the two motions is mostly unidirectional and in total the ion loses its initial magnetron radius and is nearly brought to rest in the center of the trap. Thus the ion species of interest can be centered within the trap whereas contaminating ions remain on a larger magnetron radius.

2.3.3 Measurement techniques employed at TRIGA-TRAP

Masses of ions can be determined by distinct excitation of certain ion motions with subsequent ion detection. Measurement instrumentation employed at TRIGA-TRAP – as well as at various other mass spectrometry facilities – is divided into destructive and non-destructive methods, which will be introduced in the following. **T**ime-**o**f-**f**light **i**on **c**yclotron **r**esonance method (ToF-ICR) and **p**hase-**i**maging **i**on **c**yclotron **r**esonance technique (PI-ICR) are examples of the former section, whereas the narrow-band **f**ourier **t**ransformed **i**on **c**yclotron **r**esonance technique (FT-ICR) is one for the latter. In all these methods the cyclotron frequency ω_c is the relevant parameter to observe in order to investigate the nuclear mass, since they are connected by eq. 2.13.

(a) ToF-ICR

The ToF-ICR technique has already been introduced in 1980 [Grä80], ever since continuously developed and successfully deployed at TRIGA-TRAP since 2008 [Ket08, Geo07a, Geo07b]. A dipole excitation at $\omega_{\text{dipole}} = \omega_-$ is applied to two opposing segments of the trap ring electrode, leading to a defined increase of the stored ions magnetron radius. A subsequent application of a radio frequency for a certain time period T_{ex} on the segmented ring electrode of the Penning trap converts the magnetron motion into the reduced cyclotron motion if the excitation frequency matches $\omega_c = \omega_+ + \omega_-$. The duration of the dipole excitation usually lasts a few seconds. The applied radio frequency ω_{quad} is around the expected cyclotron frequency ω_c. Afterwards, the trap is emptied and the ions are sent onto a detector, which detects the ions and allows measuring their time of flight [Fer07]. By passing through the magnetic field gradient, ions experience an acceleration whose magnitude depends on the initial angular momentum $\mu = \frac{1}{2}\, q\, \omega\, r^2$. Because the radius is conserved during the conversion, and $\omega_+ \gg \omega_-$, ions fully converted to a reduced cyclotron motion experience the strongest acceleration [Kön95]. By recording the time of flight as a function of the frequency ω_{quad}, a resonance spectrum as shown in fig. 2.11 (left) is generated, in which a minimum in the recorded resonance indicates the cyclotron frequency of the ion. The general shape of the resonance is given by the Fourier transformation of the excitation pulse. The sinc(x) function corresponds to an excitation pulse with constant amplitude and can be fitted to the experimental data to determine the cyclotron frequency [Bla06], [Bol90]. The uncertainty of the fit

$$\Delta(\omega_c) \propto \frac{1}{\sqrt{N_{ion}}} \cdot \frac{1}{T_{ex}} \tag{2.20}$$

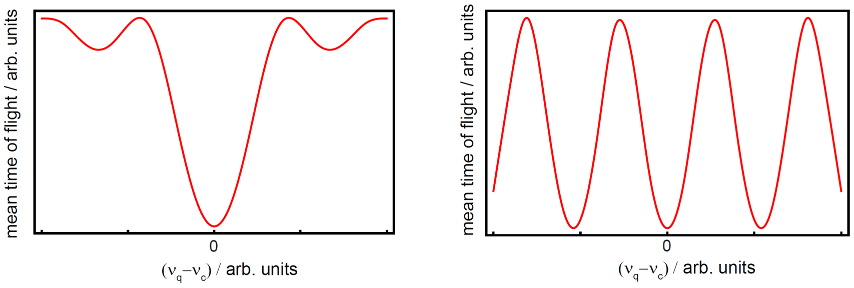

Figure 2.11: Recorded resonances with continuous excitation (left) and Ramsey excitation (right) [Ren16].

depends on the number of detected ions N_{ion} and the excitation time T_{ex}, thus a longer conversion time is usually preferred.

Since ions are ejected, they are lost after each measurement cycle and a reloading of the trap is required. This measurement cycpe is repeated for a range of excitation frequencies to acquire a spectrum as in fig. 2.11. Because it is desirable to only trap one particle at a time, the frequency range has to be scanned several times until an appropriate amount of counts are accumulated, typically several hundred to thousand ions. The number of ions is oftentimes limited and an extension of the excitation time to minimize the statistical uncertainty is not always possible. Longer excitation times imply prolonged storage times, which increase the risk of collisions between ions with the residual gas atoms. The latter results in particle losses or a damping of the reduced cyclotron motion and correspondingly μ. Then, the time of flight increases due to less acceleration within the magnetic field gradient. Thus the minimum in the determined resonance is less significant yielding a higher uncertainty. Magnetic field fluctuations, which also increase the measurement uncertainty are another argument against long storage times. Thus it is necessary to find a suitable compromise to minimize the duration of the measurement cycle and simultaneously extend the conversion time to get the maximum gain in precision. A method to reduce the uncertainty is the utilization of the so-called Ramsey excitation scheme of separated oscillatory fields [Geo07a] (and references therein): In contrast to the continuous excitation outlined above, the excitation pulse is split into two pulses, whereas the integral of these pulses is kept constant in comparison to the continuous operation scheme (see fig. 2.11), to enable a complete conversion of the two ion motions. The change in the excitation scheme results in an enlargement

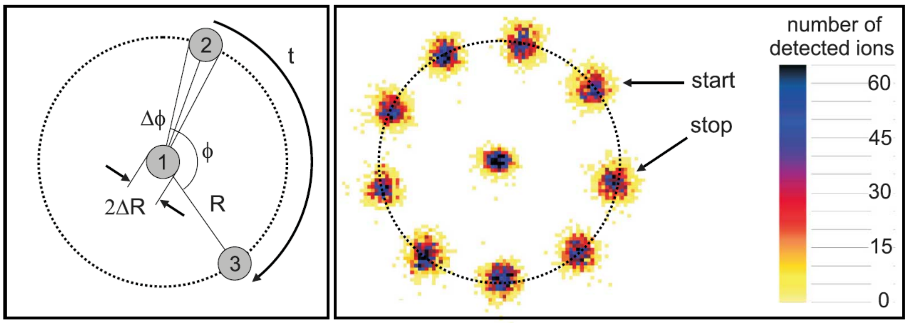

Figure 2.12: Left: Principle of the PI-ICR-measurement technique. Right: Experimentally recorded projections of ^{130}Xe^{+} ions, measured at SHIPTRAP [Eli13]. For details, see text.

of the two sidebands but also in a reduced linewidth, which results in a gain in precision about a factor of three [Kre07, Geo07b].

(b) PI-ICR

A novel technique to execute mass measurements of short-lived nuclides is the PI-ICR technique. It is based on the projection of the radial motion of the trapped ion onto a position sensitive detector that is located behind the Penning trap [Eli13]. The cyclotron frequency of the ion is given by the sum of its eigenfrequencies $\omega_c = \omega_+ + \omega_-$, similar to ToF-ICR. But in contrast, the magnetron ω_- and modified cyclotron ω_+ frequencies are determined by two independent measurements using the PI-ICR technique. As the measurement cycles for both motions are similar the subscripts + and − that distinguish both frequencies will be omitted in the following. The principle of this measurement technique is shown in fig. 2.12. First, the center of the radial motion is defined by ejecting a non-excited ion onto a position sensitive MCP-detector, yielding a spot at position 1, fig. 2.12. Subsequently a radio frequency-field with a defined amplitude and initial phase is applied at the radial motion frequency ω to increase the radius of the ion motion R, thereby generating a reference phase of the radial motion (fig. 2.12, position 2). After a certain evolution time T, the radial motion of the ion accumulates a total phase of $\phi + 2\pi n = 2\pi\omega T$, depicting the *final phase* of the radial motion (fig. 2.12, position 3), whereas ϕ describes the polar angle between positions two and three. n denotes the number of full revolutions that the ion has performed in the observed time interval. The investigated frequency of the radial motion can be calculated according to

$$\omega = \frac{\phi + 2\pi n}{T} \tag{2.21}$$

by determination of the angle ϕ for a chosen accumulation time. To ascertain the number of full revolutions n that the ion executes in the given time T, it is required to perform a preparatory measurement to investigate the radial-motion frequency with a moderate precision. PI-ICR is a destructive method like ToF-ICR but requires a lower rate of ions and is up to 25 times faster. The coordinates of the center and the reference phase remain constant during a long time period. The measurement cycle is therefore reduced to measurements of the final phase for the magnetron and cyclotron motions. Implementation of this technique is expected to result in a 40-fold increase in resolving power and fivefold gain of the precision of the cyclotron-frequency determination [Eli13]. First results of the implementation of this technique at TRIGA-TRAP are reported in the thesis of J. van de Laar [Laa15].

(c) FT-ICR

A different measurement method is the so called FT-ICR, which detects image charges, induced by the oscillating charge of a trapped ion. In contrast to the already introduced ToF- or PI-ICR techniques it is non-destructive. Thus the ion species of interest is stored within the Penning trap during the whole measurement procedure. This technique is highly sensitive and requires a minimum amount of ions, thus it is suited for identification and characterization of nuclides with very low production rates [Web05]. Using a narrow band detection system with large amplification, a complete measurement cycle can be performed with a single ion. The duration of a measurement cycle is determined by the pressure inside the trap as well as the half-life of the nuclide. Usually this method is limited to nuclides with half-lives above one second. The most challenging part is the suppression of electrical noise, e.g., creating a sufficiently high signal-to-noise ratio, since the magnitude of the observed image-charge is only about a few fA [Ket09]. A cryogenic environment at 4 K is most suitable to limit thermal noise, but an implementation at 77 K is foreseen at TRIGA-TRAP. First results are presented in [Eib13] while details of its upcoming implementation will be reported within the thesis of S. Lohse [Loh17].

Chapter 3

Experimental setup

The mass spectrometry experiment TRIGA-TRAP, which is located at the research reactor TRIGA Mainz, consists of several stages that contribute to the production of a low energy ion beam. A photograph of the reactor hall is given in fig. 3.1, whereas a technical drawing of the setup is shown in fig. 3.2 .

Short-lived fission products are produced in a target chamber containing fissionable material located close to the reactor core. They are extracted by a gas-jet system, focused by an aerodynamic lens and transformed into an ion beam by surface ionization. The generated beam is extracted, accelerated and guided by an ion-optical system to a dipole mass separator magnet. After mass separation the ion species of interest is guided into a gas-filled radio frequency quadrupole (RFQ) trap and transformed into ion bunches. An attached pulsed drift tube decelerates these bunches and enables trapping of the ions in Penning traps, where the cyclotron frequency – therefore the mass of the ions – can be determined. Detailed descriptions of the individual parts are given in the following sections.

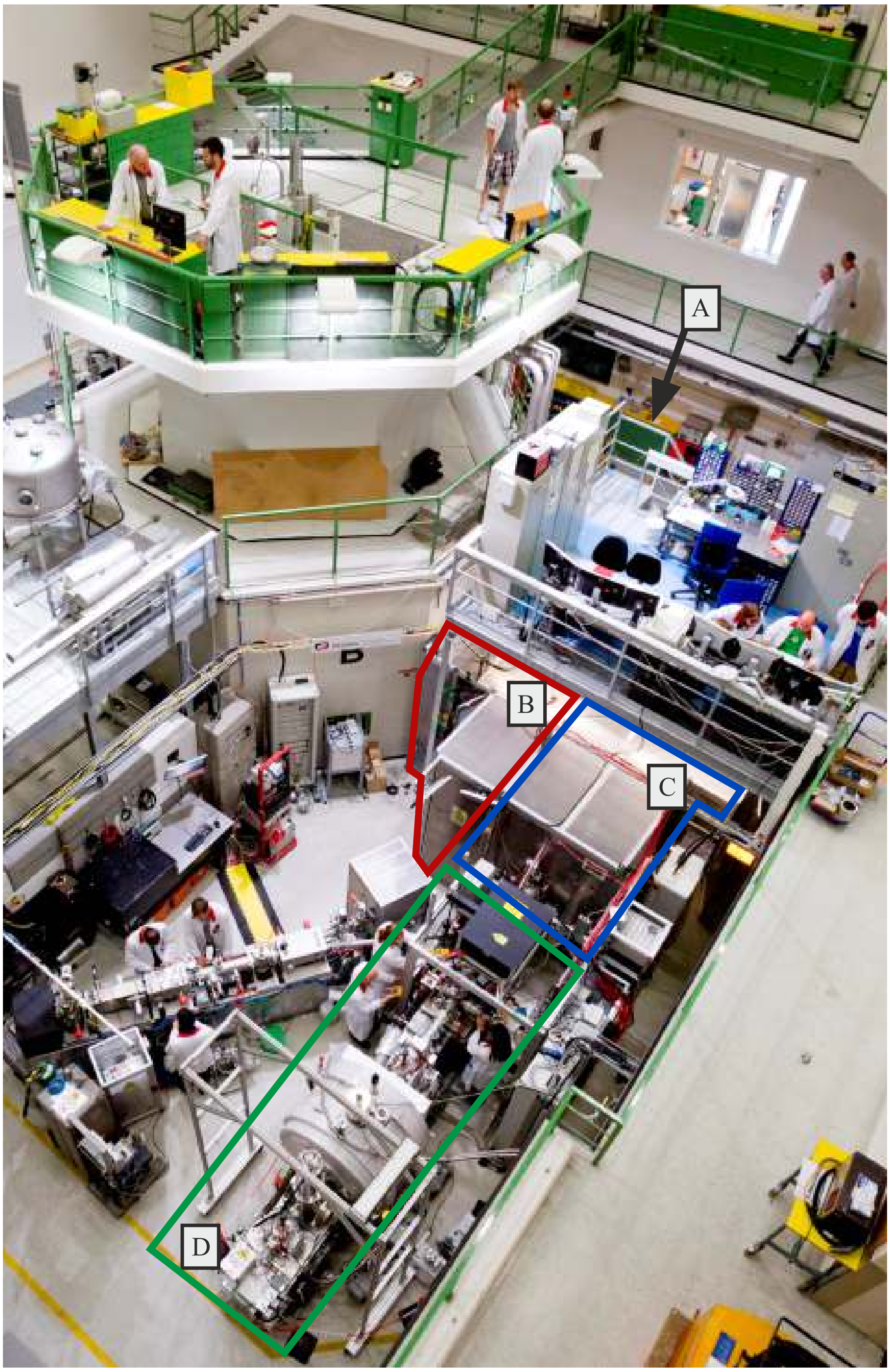

Figure 3.1: View into the TRIGA reactor hall onto the TRIGA-TRAP experiment. The experiment can be divided into three sections. (A): gas-jet system in front of beam port A (not seen in the picture). (B) gas-jet injection, ion beam production and acceleration. (C): mass separation, cooling and bunching within an RFQ and subsequent deceleration. (D): trapping of ions inside the strong magnetic field of the superconducting magnet.

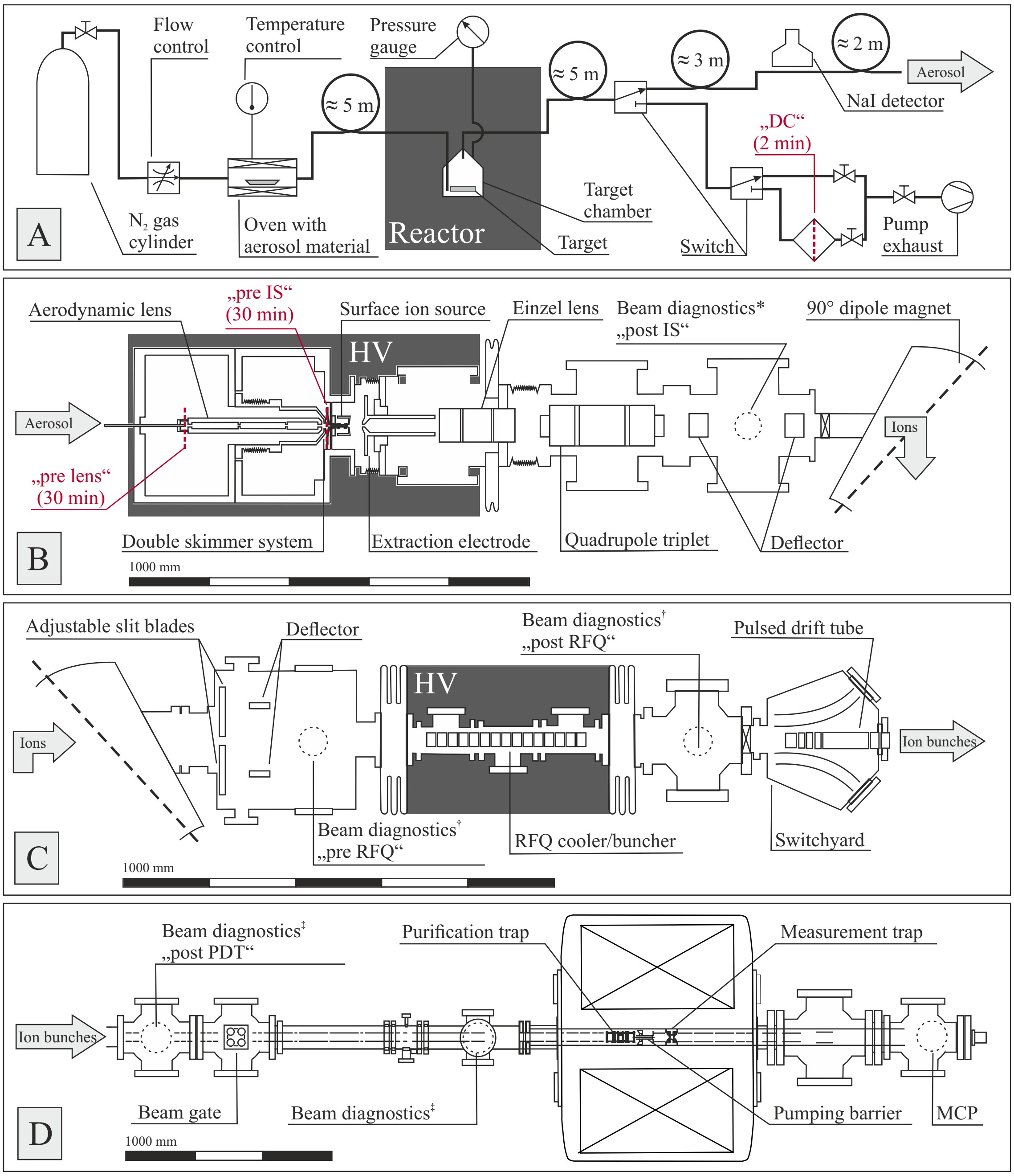

Figure 3.2: Detailed drawings of the different stages of TRIGA-TRAP, see fig. 3.1. Section A: aerosol-based gas-jet system for fission product transport. Section B: fission product collimation in an aerodynamic lens, ionization and subsequent acceleration. Section C: mass separation by a 90° dipole magnet, cooling and bunching of ions by an RFQ with subsequent deceleration. Section D: Penning-trap system for high-precision mass measurements on ions.
Different beam diagnostic types are indicated by *: catching station (CS) + Faraday cup (FC), †: CS+FC+MCP or ‡: MCP. The minimum time between the end of a fission product collection and the start of the corresponding γ measurement amounts to 5 min (*) or 1 min (†). Further filter positions for fission product collections and their time constraints are indicated in red.

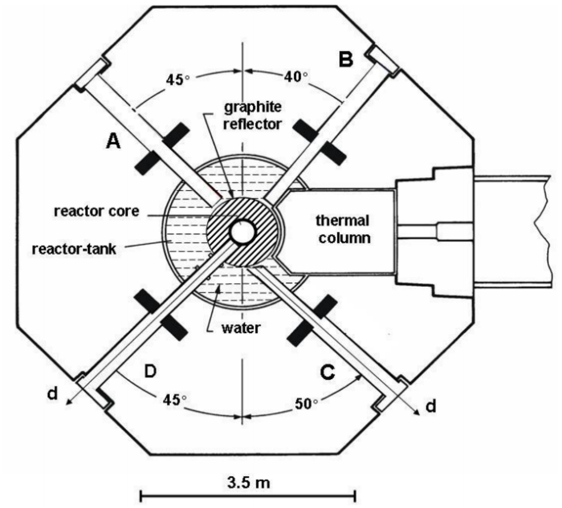

Figure 3.3: Sectional view of the TRIGA Mainz, indicating the four beamports A,B,C and D [Ham10]. The TRIGA-TRAP experiment is connected to beamport A.

3.1 Radionuclide production and extraction

Research reactor TRIGA Mainz

The TRIGA Mark II reactor at the Institute of Nuclear Chemistry at the University of Mainz is a swimming pool reactor with a graphite-reflected core. The fuel elements consist of an uranium zirconium hydride alloy, each fuel element containing about 36 g of ^{235}U. The reactor can be operated in either continuous mode with a thermal power of 100 $\mathrm{KW_{th}}$ or in pulsed mode. Four to five pulses with a peak power of 250 $\mathrm{MW_{th}}$ and a pulse width of 30 ms can be initiated per hour [Men75]. The TRIGA Mainz has a central experiment tube, three pneumatic transfer systems and a rotary specimen rack with 40 positions, for irradiation of samples with different neutron fluxes for short periods of only a few seconds up to several days. Furthermore, there are four beamports available, each penetrating the surrounding biological shield, and offering irradiation positions for long-term experiments (see fig. 3.3). These beamports are accessible from the ground floor of the reactor hall. The TRIGA-TRAP experiment is connected to beamport A, thus having access to a thermal neutron flux of $1.05 \cdot 10^{11}\,\mathrm{cm^{-2}s^{-1}}$ [Ren16]. For future measurements, beamport B is also available and of major interest, since the neutron flux is about a factor two higher ($1.8 \cdot 10^{11}\,\mathrm{cm^{-2}s^{-1}}$ [Rea89]).

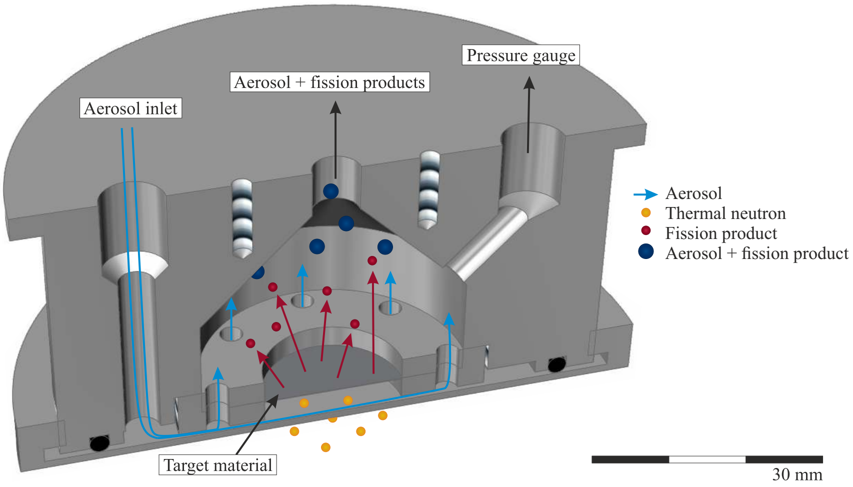

Figure 3.4: Technical drawing of the target chamber which is placed inside of the reactor close to the reactor core. Aerosol particles (blue line) enter the chamber through the inlet on the left. Radionuclides (red) produced by neutron induced fission adsorb at the aerosol particles (blue) and are extracted through the central port.

Fission target

To access short-lived neutron-rich radioisotopes produced by neutron induced fission, a target chamber containing fissionable material is placed closed to the reactor core. It is inserted into the reactor via beam port A, which is depicted in fig. 3.3. A section view of the target chamber is shown in fig. 3.4. It has one inlet and two exhausts, which are connected to PTFE (polytetrafluoroethylene) capillaries for several purposes: The aerosol produced by the gas-jet system is guided into the target chamber via the inlet. Several holes are surrounding the target material to enable the aerosol to uniformly flush the inner volume of the target chamber. The resulting main stopping volume amounts to 54 ml. After fission products are thermalized within the chamber, they adsorb on the aerosol particles and are guided with the gas stream out of the central aperture to the following experimental devices.

The pressure inside the target chamber is monitored continuously via a connection to a pressure gauge. The pressure is a crucial parameter, since the stopping power strongly depends on it. If either pressure or stopping power is too low, major losses occur due to impacts of the fission products onto the chamber walls. Increasing the pressure includes the risk of a leakage and thus a decrease in the target lifetime. Changing the pressure by varying the gas flow rate is the method of choice, but it

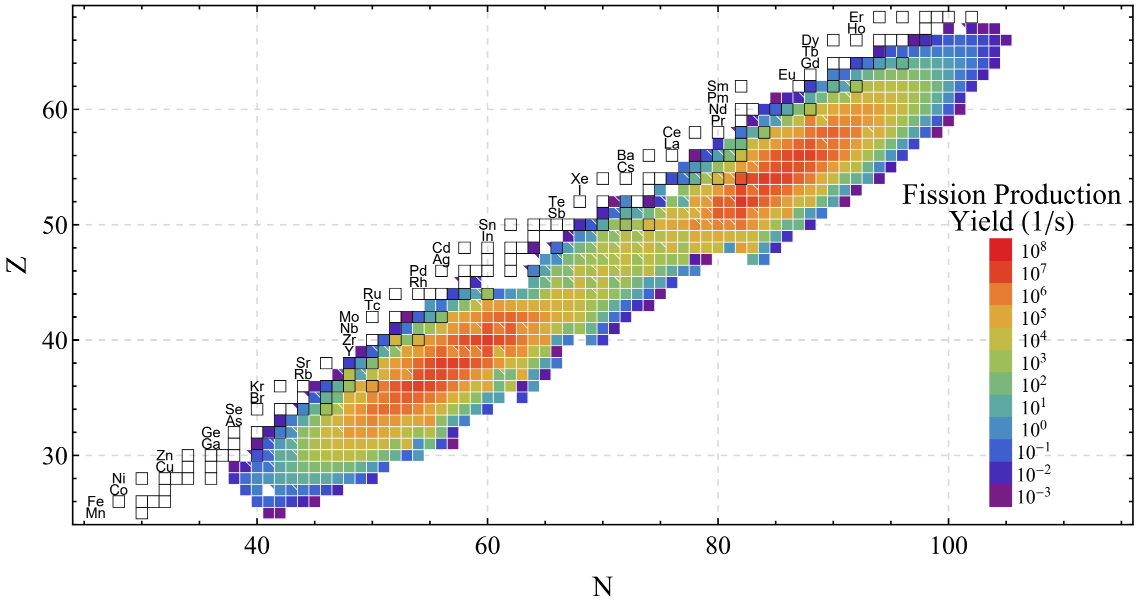

Figure 3.5: Independent fission yields of a target containing 1440 µg ^{235}U at a neutron flux of $1.05 \cdot 10^{11}\text{cm}^{-2}\text{s}^{-1}$.

has to be considered that the gas flow is hardly an independent parameter. It affects the aerosol particle formation, the transport time as well as the pressure inside of the experimental setup, i.e., the aerodynamic lens and the ion source. Therefore finding the optimum parameters is of major interest.

The fissionable material used within this work is ^{235}U, which is covered with a thin aluminium foil. Fission yields corresponding to a target containing 1440 µg ^{235}U are given in fig. 3.5. The distribution of produced radioisotopes shows a maximum in the light branch around mass number $\text{A} = 100$ and another one in the heavy branch around $\text{A} = 140$. The energy release during one fission process of ^{235}U amounts to $\Delta E \approx 200\,\text{MeV}$ corresponding to $0.8\,\text{MeV/A}$ to $0.9\,\text{MeV/A}$ [Lie91]. This energy is split among all particles released during the fission, i.e., neutrons, γ rays or the two main fission fragments. The latter gain in sum a kinetic energy of around $170\,\text{MeV}$ [Sch66]. Due to the momentum conservation light fission products gain an energy of $\approx 100\,\text{Mev}$ whereas the heavier ones gain $\approx 70\,\text{MeV}$ [Sch66]. The heavy fission branch populates radioisotopes with comparably long half-lives and would contaminate the whole setup, which is still under development and various parts have to be exchanged regularly. An aluminium foil of appropriate thickness holds back the heavy fission fragments completely, thereby prohibiting a prolonged contamination. The lighter fission products are stopped as well, but due to their higher energy a part of them passes the Al foil. The transmitted fragments are slowed down, thus an absolute pressure around 1.1 bar inside the target chamber is sufficient to thermalize nuclides within the given volume. This allows to operate the gas-jet at low gas flow rates without a loss in yield.

Four ^{235}U-targets have been used during the commissioning phase of TRIGA-TRAP and within this work: Whereas the geometrical size of them has been kept constant at a diameter of 15.0 mm, certain parameters have been changed as listed in table 3.1, i.e., the mass of the fissionable material and the thickness of the aluminium cover. The change from target A to target B has been made to improve the yield of fission products by a significantly increased amount of target material and simultaneously a thinner Al degrader. Whereas target A has been covered with a 13 µm Al foil, a reduced layer of 10 µm Al has been used for subsequent targets. This reduced thickness is sufficient to thermalize the generated radionuclides completely, as simulated by Ziegler et al. with SRIM2013 [Zie13]. Under these circumstances the release of produced light fission products into 1 bar N_2 amounts to around 3 % to 8 % depending on their mass [Ren16]. According to those simulations, the mean range of ^{91}Rb ions recoiling out of the target amounts to 11.9 mm. The minimum distance between a chamber wall and the target itself is about 16 mm, so all fission products should be stopped within the gas volume.

For subsequent experiment runs, the target had to be substituted two more times, due to external circumstances. A yield measurement has been performed with target B and target D to verify the total amount of fission products available. Results of these measurements are given in sec. 4.1.

Table 3.1: Parameters of the targets used during commissioning of TRIGA-TRAP.

	Target A	Target B	Target C	Target D
Year	2014	2015	2016	2017
Surface diameter (mm)	15.0(5)	15.0(5)	15.0(5)	15.0(5)
Target amount ^{235}U (µg)	310(16)	1258(63)	1256(63)	1440(72)
Areal density ^{235}U ($\mu g\,cm^{-2}$)	175(9)	712(36)	711(36)	815(41)
Thickness Al foil (µm)	13(2)	10(3)	10(3)	10(3)

Future measurement campaigns investigating nuclides of the heavy fission branch will require using a non-covered target ore one covered with a thinner aluminium foil. Here, the requirement of a higher pressure arises as a consequence of the lacking covering, since a major contribution to the thermalization is absent.

Aerosol-based gas-jet system

Most fission products are not transported sufficiently in pure gas (see sec. 4.1.4). Therefore an aerosol-based gas-jet system is used to extract produced fission products out of the target chamber and transport them through the biological shield. A schematic sketch of this system comprising the main components is shown in fig. 3.2.

The carrier gas of choice is nitrogen as it provides both a minor collision ionization and a low activation by neutron capture at the same time. Simultaneously it has a high molecular mass and thereby a high stopping power. Gas flow rates in the range of 300 ml/min to 800 ml/min have been used, depending on the type of measurement. Most of the measurements in this work were performed at 400 ml/min, thus the gas flow rate is only noted if it deviates from this value. The aerosol material of choice is CdI_2, which is placed in an oven and heated up to a temperature of 290°C. In previous works [Ren16, Bey14a, Gün93], KCl was used instead ($\rho = 1984\,\mathrm{kg/m^3}$, $IP_K = 4.341\,\mathrm{eV}$), but due to better physical properties, it was replaced by CdI_2. Its comparably high density of $\rho = 5640\,\mathrm{kg/m^3}$ leads to the formation of heavy particles, which improves aerodynamic focusing and maximizes the transport efficiency. The ionization potential of cadmium amounts to $IP_{Cd} = 9.0\,\mathrm{eV}$, thus only traces of the material are ionized within the hot cavity thereby reducing the background of subsequent measurements significantly.

The aerosol is guided to and from the target chamber through the biological shield by PTFE capillaries with inner diameters of 4.0 mm and 0.86 mm, respectively. In both cases, their length amounts to $\approx 5\,\mathrm{m}$. Fission products adsorb on the CdI_2-particles and are guided through the biological shield to a fume hood. There, a switch enables to either inject the aerosol into the experiment beamline or guide it to a waste channel where it is pumped away. The latter is used whilst preheating of the oven, during maintenance at the experimental setup or when the reactor is out of operation. For fission product measurements, the aerosol is either guided to the aerodynamic lens or to a dedicated collection position (abbreviated “direct catch”, DC) inside the fume hood at which glass fiber filters can be inserted. Embedded aerosol particles collected on these filters allow yield measurements or efficiency determinations. Results of these studies will be discussed in sec. 4.1.4.

When the aerosol is guided through the PTFE capillary (inner diameter $= 1.2\,\mathrm{mm}$, length $\approx 5\,\mathrm{m}$) to the aerodynamic lens, it passes a sodium iodide-based γ-ray detector, which is used for two purposes: by taking data once a second, slow changes in the transport efficiency can be traced. Or by taking data once a millisecond, only a short interval of 16 seconds can be investigated, but with much better time resolution. Thus, rapid changes in the yield due to particular occurrences can be observed, e.g., prompt γ rays and subsequently transported activity produced by a reactor pulse.

The transport time of the nuclei is of major interest as it limits the range of accessible species. It has to be sufficiently short to prevent the nuclei of interest from decaying before investigation. But as the flow rate of the carrier gas influences the pressure inside the target chamber and thereby the thermalization process, it is important to find the optimum conditions for the setup and simultaneously find the limits of accessible nuclides. The installed γ-ray detector can be used for such a determination of the transport time. These measurements require no changes to the experimental setup and could be carried out in parallel. The only requirement is a distinct start, for which the pulsed operation of the TRIGA reactor was used. Results of the transport measurements will be discussed in sec. 4.1.5. Thereby it offers the chance of either having a continuous online monitoring over the amount of passing fission products or make transport time measurements.

After passing the capillary system, the fission products enter the vacuum chamber that is mounted on a high voltage platform. They are guided through an aerodynamic lens to produce a collimated particle beam to maximize the injection efficiency into the surface ion source. A detailed drawing of this part of the gas-jet is given in fig. 3.6. Fundamentals of aerodynamic focusing and the aerodynamic lens are described in sec. 2.1 as well as in [Gru14] and [Gru16]. It is possible to place a glass fiber filter in front of the aerodynamic lens, behind the lens or in front of the ion source as indicated in fig. 3.2 as “Filter Position” to collect the transported

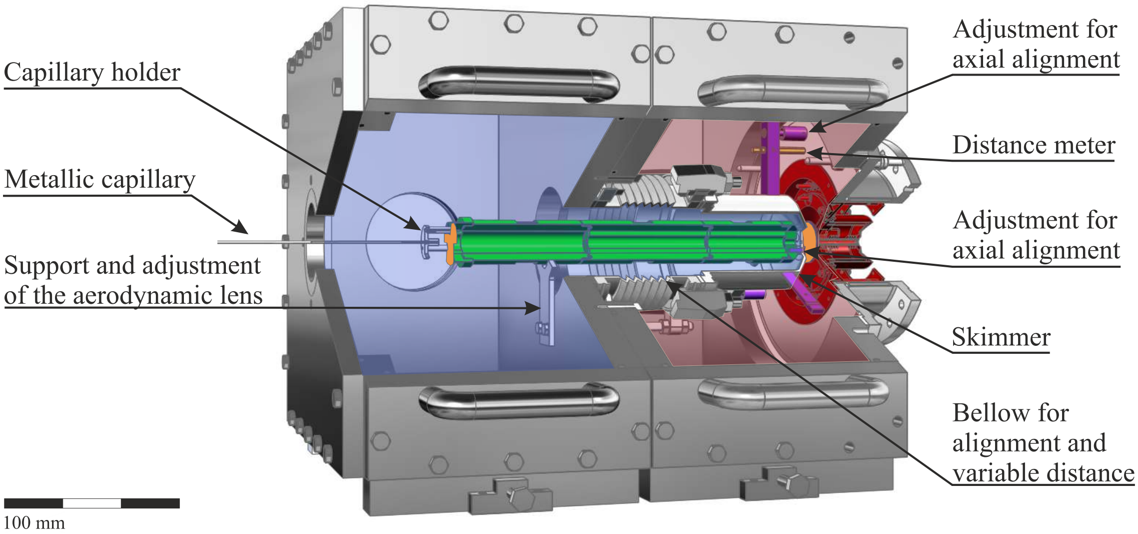

Figure 3.6: Detailed drawing of the vacuum chambers housing the aerodynamic lens (green) inside of a bellow-skimmer-combination. The chamber is separated into two parts (blue and red volume), which are pumped separately. Several tools for axial alignment (purple) are available. The system is connected to the surface ion source (dark red). Two glass fiber filters (orange) were added in front of the lens and the ion source to indicate the catching positions. For more details, see text.

activity for efficiency studies. Results will be discussed in sec. 4.1.4.

The custom made vacuum chamber, that contains the aerodynamic lens, is split into two parts that are separated by a partition panel but connected with each other by the skimmer. Its side panels are detachable to enable access to the inner parts, e.g., for alignment or maintenance. The low vacuum side is coupled to the capillary coming out of the target chamber and the high vacuum side is attached to the surface ion source (see sec. 3.2). Each chamber is pumped down separately: The low vacuum side including the inner volume of the bellow is connected to a large roots pump (Edwards EH2600; pumping speed $\approx$ 500 m^3/h) due to the high gas load and reaches pressures around 10^{-2} mbar during gas-jet operation. The high vacuum side is pumped down by a combination of pre- and turbomolecular pump to reach a pressure of around 10^{-5} mbar. Thus the necessary pressure drop for aerodynamic focusing is created. Before entering the vacuum chamber, the PTFE capillary is coupled to a steel capillary with an inner diameter of 1 mm. This transition is necessary since only the latter can be connected to a vacuum-tight feedthrough, which is mandatory for the insertion of the aerosol into the vacuum. It ends inside a capillary holder at a distance of 4 mm to the entrance of the aerodynamic lens and enables an axial injection of aerosol particles. The lens itself is located in a combination of a bellow and a skimmer, and directly connected with the latter to ensure proper axial alignment. The design of the lens has been revised compared to the design described in [Gru14] to reduce the weight, however it still has to be stabilized by an adjustable holder. The skimmer is required to separate the carrier gas from the particles, thereby reducing the pressure inside of the ion source. It has only a small opening orifice with a diameter of 2 mm, whereby the collimated particle beam passes whereas the major fraction of the carrier gas is pumped away. The distance between the entrance of the ion source and the skimmer is variable due to the mounted bellow. The absolute value of this distance is indicated by the distance meter and was adjusted to 4 mm. Axial alignment between skimmer and ion source is ensured by three wings with small rods, which are attached to the skimmer and whose tapered counter pieces are mounted on the ion source flange. Thus these parts can easily fitted together, which is crucial since the setup has to be opened at this position frequently for maintenance of the ion source, which will be described in the following section.

3.2 Surface ionization source

Nuclides produced by neutron induced fission show a broad charge state distribution [Woh78], but neutralize in the moment of aerosol particle attachment inside the target chamber. Their subsequent ionization is mandatory in order to enable a manipulation of their movement by electrical or magnetic fields. The first attempt to combine a gas-jet with an ion source at TRIGA-TRAP has been made with an electron-cyclotron-resonance ion source [Smo12]. But the plasma inside this source was not dense enough to break up passing aerosol particles to release and ionize the fission products. Subsequently a surface ion source has been developed at TRIGA-TRAP [Ren16], which was based on the HELIOS setup used in the 1980's at the TRIGA reactor [Maz81, Brü83, Brü85]. It was proved that this type of ion source is able to release and ionize fission products sufficiently. But although its

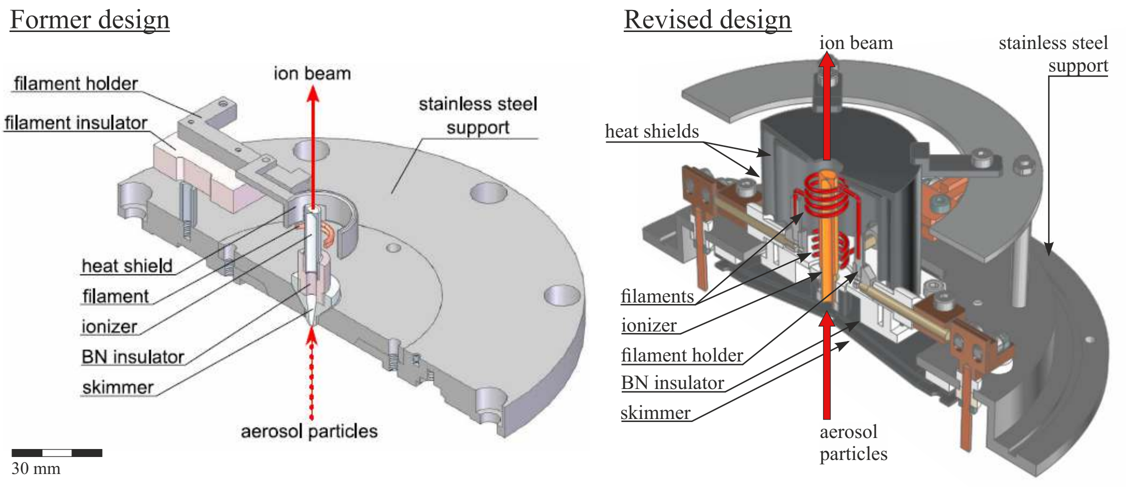

Figure 3.7: Technical drawings of the former design [Ren16] and the design revised within this work. Both drawings are shown in the same scale to allow for a direct comparison.

design has been simple (fig. 3.7, left), its installation was tricky and its operation was barely reliable. Within this work, a new surface ion source (fig. 3.7, right) has been built to ensure a stable and fail-safe operation. Its design has been developed in collaboration with JAEA/Tokai, Japan [Sat15b] and was adapted to the experimental conditions and safety requirements given at TRIGA-TRAP. Although the revised design is more complex in comparison with the former design, the fundamental structure – consisting of skimmer, ionizer, filaments and heat shield – remains the same. A detailed drawing of the new ion source is shown in fig. 3.8. The design has been optimized for reliable operation at temperatures above 2300 K, thus the materials used for individual parts (table 3.2) were chosen to be highly heat-resistant. To improve the ionization efficiency, the ionizer has an extended length

Table 3.2: Materials of individual parts employed in the renewed design

Part	Material
Ionizer	Ta
Filament holder	Mo
Filaments	W
Heat shields	Mo
Skimmer	Mo
Insulator	BN
Electrical feedthrough	Cu

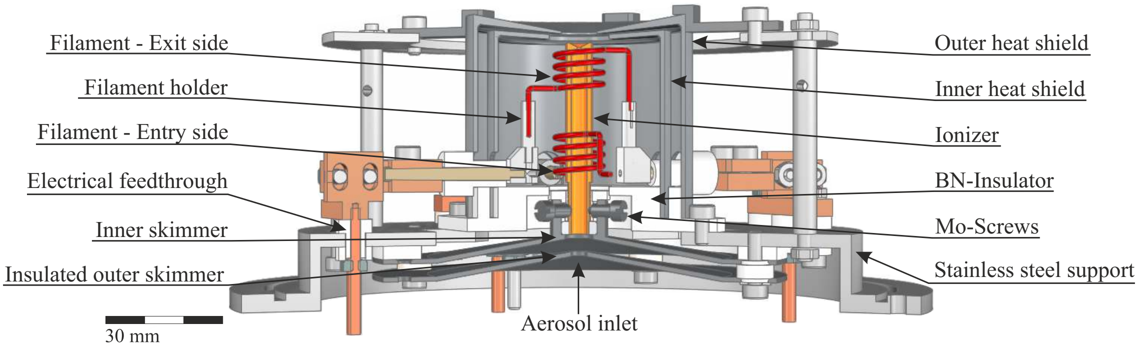

Figure 3.8: Technical drawing of the redesigned surface ion source with labeled central parts.

of 44 mm. The inner diameter of the cavity is 4 mm, the wall thickness is 0.5 mm at the entrance and 1 mm at the exit, and the exit orifice diameter is 1 mm. The front of the tantalum tube is tapered to reduce the thermal contact with the surrounding parts. It is connected to the inner skimmer via three Mo-screws without having an additional point of contact. The minimized thermal contact suppresses aerosol material deposits at the ionizer entrance or the skimmer orifices. Due to the long length of the ionizer it is not possible to create a homogeneous temperature distribution with only one filament. Thus it is surrounded by two filaments made from 1-mm diameter W wires. Each filament consists of 3.5 loops with a diameter of 11 mm. Both filaments are electrically separated from the remaining components, i.e., the ionizer, by BN-insulators.

Resistive heating of the filaments to high temperatures induces the emission of electrons. Applying a potential difference between the filaments and the ionizer ($U_{ionizer} - U_{fil} \approx 300\,V$) accelerates the electrons onto the ionizer surface, which is thereby heated to temperatures above 1700 °C. This technique has been developed in 1959 by A. Calverley [Cal59] and is called “electron bombardment” (EB). The magnitude of heating depends on the quantity of emitted electrons and thereby the heating current of the filaments as well as the applied potential difference. The wiring diagram of the ion source is shown in fig. 3.9. The complete assembly including the vacuum vessel is installed on a 30 kV platform, insulated from the remaining setup. The use of two independent voltage supplies for electron bombardment offers the ability to fine tune the heating power of the entry and exit side of the ionizer.

Filaments and ionizer are encased by two shields in order to reduce heating losses.

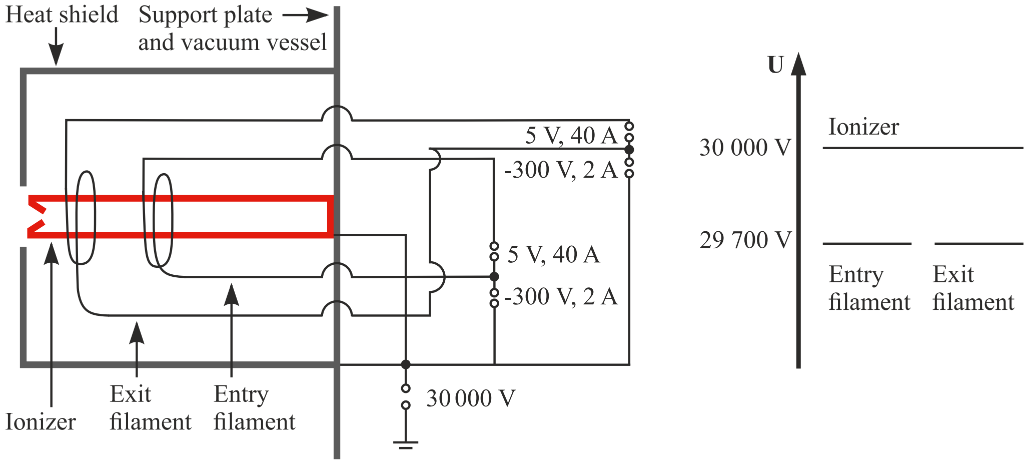

Figure 3.9: Wiring diagram of the surface ion source. A high voltage of 30 kV is applied to the ion source and the vacuum vessel, while the potential of the filaments is around 300 V lower.

Their thermal contact among each other as well as to surrounding components is minimized. They are inserted into two milled slots within a boron nitride insulator and fixed by four small molybdenum brackets. The latter are connected to the support plate by four steel rods. This configuration minimizes the heat transfer from the heat shields to the support plate and thereby to the skimmer. The heat shields are held on the same potential as the ionizer and thereby shield the emitted electrons from outer electric fields. They additionally minimize the direct thermal radiation from the ion source. Fission products transported into the hot cavity disintegrate from the aerosol clusters as they touch the hot surface and transform into ions via surface ionization (see sec. 2.2). The created ions are extracted through a strong electric field created by a following electrode.

Besides ionization of nuclides transported by the gas-jet, there is also the option to deposit material directly inside of the ionizer. It offers the advantage to ionize an element species of choice and simultaneously renders the time consuming gas-jet operation unnecessary. Within this work this method was used for calibration of the mass separator (see sec. 4.3).

The major advantages of the new ion source are its straightforward assembly and its reproducible alignment that enables a reliable operation and also increases its lifetime. Assembling and heating of the former ion source (3.7, left) has been challenging. The installation of the various ion source components had to take place inside a vacuum chamber of the beamline, thus it was complicated due to the limited available space. A tilted filament was not uncommon and regularly induced short circuits due to contact to the ionizer. Oftentimes neighboring loops of the filament fused during the heating process since the ion sources design intends to assemble the wire under tension. The new design avoids these difficulties: the ion source is assembled completely outside of the experimental setup, thus every component is accessible and can easily be aligned and tightened. The ion source components are mounted on a support plate, which fixes the ion source inside the beamline with four small screws. The filaments are produced with the required angles, thus they can be installed without tension. The distance between the loops is large enough to prevent a fusing during the first heating process.

The temperature of an ion source is the central parameter. Thus it is important to know this parameter during operation. The temperature ranges of direct measurement techniques, e.g., with thermocouples or resistance thermometers, are usually limited to lower temperatures. Such techniques also require a direct contact to the hot surface, which is difficult to realize, e.g., as there are only few materials that withstand temperatures above 2000 °C. The range of non-contact techniques is wider and therefore more suitable for monitoring of the ion source temperature. A pyrometer (Sensotherm Metis MI13), which determines the temperature by the light emitted by the ion source, is installed permanently at a viewport of the dipole magnet with direct line of sight onto the ion source. It allows a continuous monitoring of the temperature, even though the pyrometer itself is located inside a HV-cage and not accessible during RFQ operation.

Results of the extended characterization studies of the new ion source will be discussed in sec. 4.2.

3.3 Ion beam optics

As a collimated ion beam is needed for efficient transport, guidance and focusing by electric or magnetic fields is required. For this purpose several ion optical devices are installed at TRIGA-TRAP (see fig. 3.10), which will be discussed briefly within this section. More details will be presented in the thesis of P. Naubereit [Nau17].

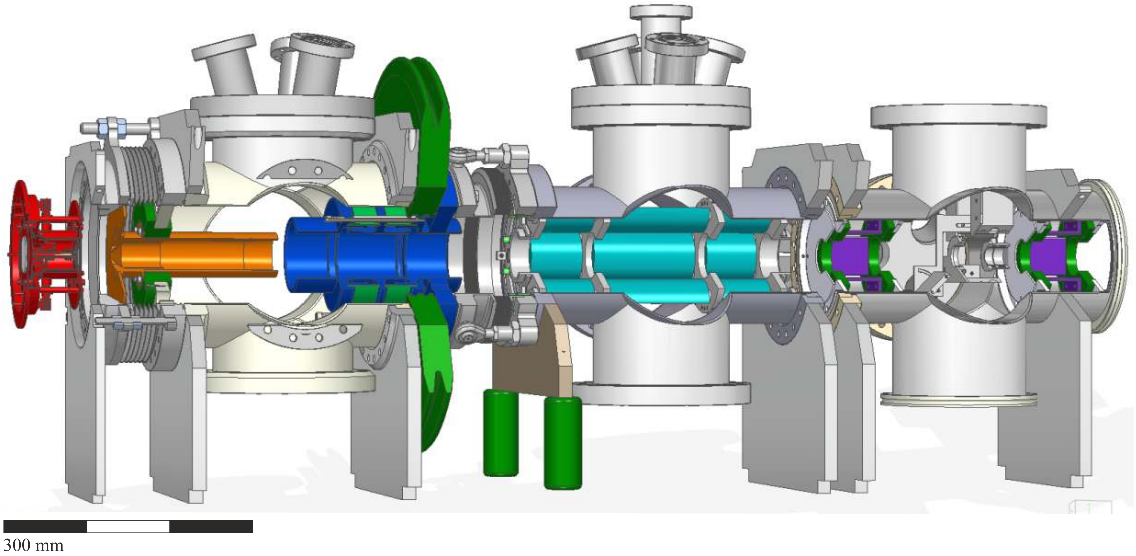

Figure 3.10: Ion optics: Ion source (red), extraction electrode (orange), einzel lens (blue), quadrupole triplet (cyan), deflectors (purple), insulators (green). For details, see text.

The ion source and correspondingly the vacuum chamber containing the aerodynamic lens is mounted on a high voltage platform with a potential of +30 kV with respect to ground potential. The high voltage platform is electrically separated from the remaining setup, which is held on ground potential. Thus ions are accelerated on their way to the dipole magnet. Simulations show that the diameter of the generated ion beam increases from 1 mm to 20 mm after 1 m beamline [Ren16] in the absence of any electrical or magnetic field. By installation of an extraction electrode in Pierce geometry [Bro04] behind the ion source and thereby producing a collimated beam, the divergence can be reduced significantly. In 2016 an extraction electrode with an inner diameter of 33 mm and an entrance orifice of 6.5 mm diameter has been installed in 40 mm distance to the ionizer exit. It is set to a changeable potential kept significantly lower than the high voltage of the ion source. This potential is chosen depending on the operating conditions. The produced ions are thus extracted and accelerated, thereby generating a collimated particle beam. It is guided to a subsequent einzel lens [Lie08], that is installed at a distance of 70 mm from the extraction electrode. It consists of three sets of cylindrical apertures (length = 46 mm/66 mm/46 mm, inner diameter = 75 mm). The first and the third electrodes are kept at ground potential whereas a voltage is applied to the

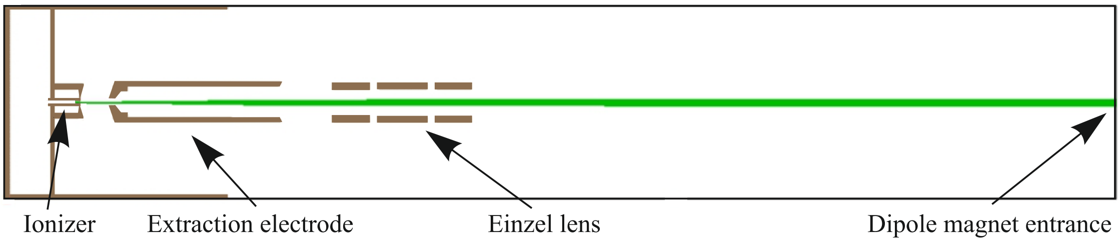

Figure 3.11: Simulation of the ion beam trajectory [Nau17], performed with SimIon [Man08]. The chosen voltages (HV: 28 kV / Extraction: 17 kV / Einzel lens: 0 V/8.3 kV/0 V) result in a beam diameter of ≈ 10 mm at the dipole magnet entrance.

central tube. The electrical field between the first and the second electrode decelerates the ions and pushes them outwards. The subsequent field between the second and third electrode re-accelerates the ions to their initial energy and radially pulls them inwards. Since the energy of ions is higher in regions of defocusing, the ion beam is focused after passing the einzel lens. The degree of focusing depends both on the kinetic energy of the ions and the potential difference between the electrodes. The simulated trajectory of the generated particle beam is shown in fig. 3.11. This trajectory refers to an ion source potential of +28 kV and a corresponding voltage of +17 kV applied to the extraction electrode. The inner electrode of the einzel lens is set to +8.3 kV while the outer electrodes remain on ground potential. With this configuration a parallel ion beam is generated, whose diameter amounts to ≈ 10 mm at the dipole magnet entrance. It improves the resolution of its mass separation and simultaneously focuses the ion beam onto the adjustable slit blades behind the magnet (see fig. 3.2, B). At this stage the beam diameter should amount to 0.5 mm to 1.8 mm in x-axis, which represents optimum conditions for the subsequent RFQ performance. During beamtime at TRIGA-TRAP the ion source has been set to +30 kV. The highest ion current behind the magnet was then achieved by applying a potential of +11.2 kV on the extraction electrode and +15.6 kV on the center electrode of the einzel lens while the outer electrodes remain on ground potential.

After these two focusing steps, the ion beam is guided to a subsequent quadrupole triplet to counteract a potential astigmatic focusing of the separator magnet. It consists of three sets of four rods arranged symmetrically around the central axis. However, as the alignment of the installed ion optics is sufficiently accurate, the shape of the produced ion beam is circular before and after mass separation. Thus it was not necessary to use this triplet for additional focusing. For further adjustment of the ion beam, two deflection stages are installed behind this quadrupole and directly in the front of the entrance into the dipole magnet. These stages consist of four parallel plate electrodes each, arranged symmetrically around the center axis. By applying a DC voltage between two opposing plates, the ion beam is deflected in the desired direction. Thus it neither changes the energy of the ions nor generates focusing of the beam, but it can optimize the injection into the dipole magnet.

3.4 Mass separation by a dipole magnet

The ion beam, created by the surface ion source and collimated by the ion optics, contains various species of radioactive as well as stable nuclei, whose abundances differ by several orders of magnitude. To investigate only one single ion species, the beam has to be separated by the mass to charge ratio, since contaminating species increase the measurement inaccuracy or even impede the feasibility.

For this a sector field dipole magnet is used at TRIGA-TRAP to perform mass separation by use of the Lorentz Force. The ions are injected as a parallel beam with a kinetic energy of 30 keV into the 90° dipole magnet with a bending radius of $\rho = 500\,\mathrm{mm}$ and a maximum magnetic field strength of $B = 1.12\,\mathrm{T}$. The transmitted mass to charge ratio m/q can be determined by

$$\frac{m}{q} = \frac{\vec{B}^2 \cdot \rho_0^2}{2 \cdot U}\,. \tag{3.1}$$

The highest separable m/q-value for 30 keV is 500 u/e. The mass resolving power of such a system is defined as the ratio of the mass m and the full-width-half-maximum of its observed mass peak Δm:

$$R = \frac{m}{\Delta m} \tag{3.2}$$

It represents the ability of a mass separator to distinguish two neighbouring mass peaks and depends on the bending radius of the magnet, its field homogeneity as well as properties of the ion beam [Wol12]. The magnet used at TRIGA-TRAP is double-focusing with a focal plane 500 mm behind the magnet. Extensive studies and characterization of the magnet's properties have been made within the work of T. Beyer [Bey14a]. To achieve maximum resolving power, usually a slit is installed at the exit focal plane, transmitting only one m/q trajectory. Due to space restrictions, it was not possible to install a slit at exactly this position, but only further away from the magnets exit face. The distance between the two sheet blades creating the slit is variable and can be reduced or enlarged if required. Usually it is optimized to achieve maximum resolution without losses in beam current.

3.5 The radio frequency quadrupole cooler and buncher

After mass separation, the ion species of interest is guided into a radio frequency quadrupole (RFQ), which was implemented and characterized by T. Beyer [Bey14a]. It is an efficient tool for cooling, accumulating and bunching of radioactive ion beams. The advantages of cooling and bunching a beam of radioisotopes, in particular in connection with subsequent collinear laser spectroscopy or ion trap experiments are well known and widely used at existing online facilities [Jok02, Jok03, Lav07].

The structure of a radio frequency quadrupole is based on the principle of a linear Paul trap. It consists of four rods that are 15-fold segmented and symmetrically arranged around a central axis. Opposing electrodes are fed with the same polarity RF signal, whereas neighboring electrodes have opposite polarity, resulting in a electric quadrupole field in the xy-plane.

The RFQ can be operated in either continuous or pulsed mode. Using the linear Paul trap as a quadrupole ion guide with buffer gas cooling produces a continuous ion beam with a reduced emittance and with a beam current up to several nanoamperes. This so-called *continuous mode* is mainly used for commissioning purposes. For loading of the Penning traps with ions, an accumulation and transformation of the continuous beam into short bunches is essential. During this *pulsed mode* operation, ions are trapped and accumulated over a defined time interval. It is realized by applying an electrostatic DC field gradient with a negative slope along the electrodes 1 to 14, which guides the ions toward the exit of the RFQ. The potential

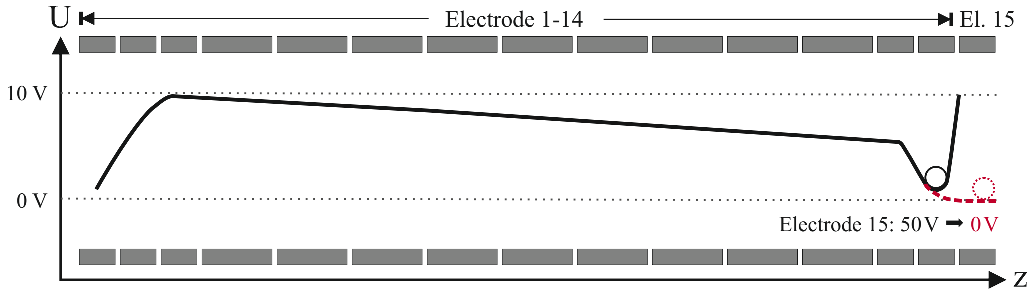

Figure 3.12: Sketch of RFQ: DV potential slope drawn between the segments of the quadrupole rods. Solid line during accumulation; dashed line during ejection of the ion bunches. Potentials are referring to the high voltage of the RFQ.

gradient is shown in fig. 3.12. Confinement in z-axis (axial) is realized by applying a high electrostatic potential at the last electrode – electrode 15 – thereby forming a potential well located close to the outlet. The high potential applied to electrode 15 effects that ions are repelled and reflected to the entrance of the RFQ. If the ion injection energy is sufficiently small ($< 20\,\mathrm{eV}$), they lose enough energy to the buffer gas that they are trapped and cannot leave the RFQ anymore. Thus the ions are trapped and accumulated within the potential well ("bunched"). The ions are stored for a certain *cooling time* to fully thermalize them with the buffer gas. The duration of this period depends on the ion species, their initial energy, the buffer gas species and its density as well as the potential slope. During cooling, the injection of ions into the RFQ is interrupted, thereby guaranteeing sufficient cooling, even for the ions captured last. When the ions are fully thermalized, electrode 15 is rapidly switched to a lower potential, thereby forming a slope that ejects the accumulated ions. Because gas escaped through the ions entry and exit orifices of the RFQ it has to be fed and pumped away constantly. Typical parameters for the He gas flow are 0.16 mbar l/s to 0.18 mbar l/s during continuous operation and 0.14 mbar l/s to 0.16 mbar l/s for ion bunching. The bunching frequency is typically set to 1 Hz to 40 Hz, with a accumulation times of 25 ms to 1 s. The cooling time is set to 4 ms to 20 ms, depending on the m/q-ratio of the observed ions. Detailed parameters for studies in the region of 89-95 u are listed in table 3.3. The RFQ is connected to a switchyard with three separate outlets to transfer the prepared ions to adjacent experimental devices. This allows the use of the generated ion beam for different experimental facilities. Ions can be either guided through the centre exit towards

Table 3.3: Adjusted RFQ parameters for cooling and bunching ions in the mass region of 89 u to 95 u.

Radio frequency	1.05 MHz
RF amplitude	300 V
Capture voltage	60 V
Buffer gas pressure	0.18 mbar l/s
Accumulation time	95 ms
Cooling time	4 ms
Ejection frequency	10 Hz
Ejection voltage	0 V
Ion injection energy	20 eV

the Penning trap, or to any other device, which can be coupled to one of the two outlets located at a 45° angle on both sides. The switchyard and the possible ion beam trajectories are indicated in fig. 3.13. Which way the ions are guided can be selected by a deflection electrode that is located in front of the switchyard and deflects the ion beam by an initial angle of 8° into the curved, main 37° deflection electrodes [Krä10]. Currently, the left port is inaccessible due to space restrictions, but the right port could be used to connect another experiment beamline or additional detection systems.

3.6 The electrostatic deceleration stage

Because the potentials of the Penning traps are not deep enough to trap particles with more than a few eV beam energy the difference between the kinetic energy of produced ions and the potential of the trap has to be low. Since it is undesirable to mount the trap section of TRIGA-TRAP on a potential of 30 keV, the kinetic energy of the ions has to be reduced distinctly. For this purpose, a deceleration stage is used at TRIGA-TRAP. It consists of a drift tube which is pulsed to a lower potential when the ion bunch is traversing. It is installed in the center pathway of the switchyard (see fig. 3.13). To optimize the injection into the pulsed drift tube (PDT), a segmented deflection electrode and three electrodes are installed in front of it. The potential of these focussing electrodes is usually 3 - 5 kV below the high voltage potential of the RFQ. The PDT is a 200 mm long cylindrical tube,

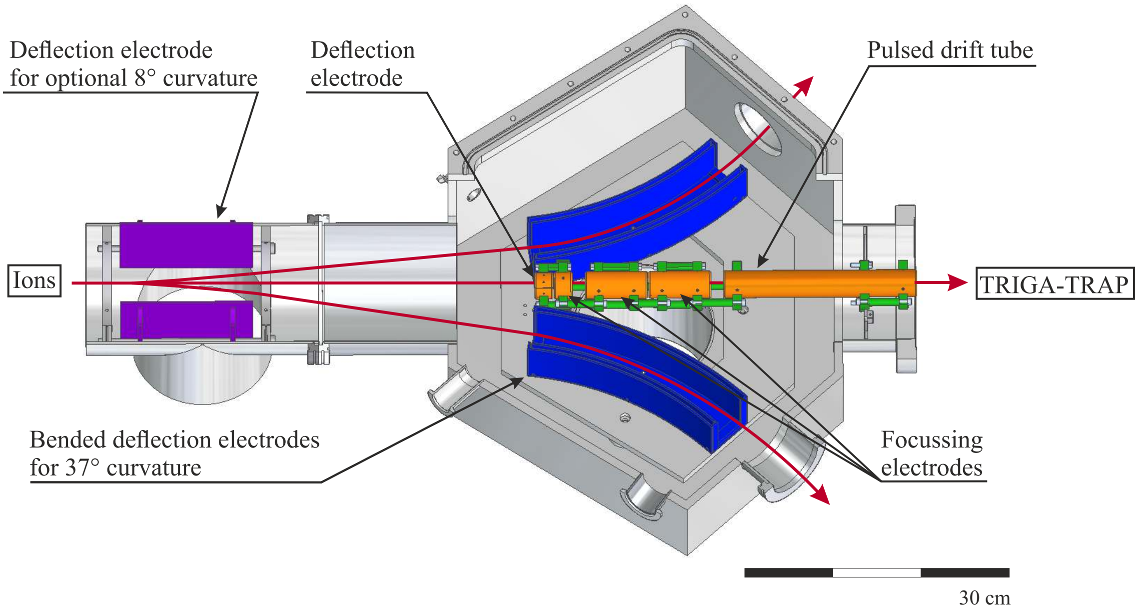

Figure 3.13: Technical drawing of the switchyard, containing the deflection electrodes (purple) to guide the ions either to the pulsed drift tube (orange) or to a different experimental setup. The latter require the bended deflection electrodes (blue) for a 37°curvature of the ion beam.

which is biased to $U_{high} = 28.9\,\text{kV}$, i.e., about 1 kV below the RFQ-potential. A schematic drawing of the electrode potentials and the kinetic energy of the ions within the deceleration stage is shown in fig. 3.14. Ion bunches entering this electrode experience a deceleration to an energy of 1.1 keV. When they are in the center of the PDT, its potential is changed by a high-voltage switch (Behlke HTS 301-03-GSM) in less than 200 ns to a potential of $U_{low} = \text{-}1.1\,\text{keV}$. Thus the potential energy of the ion bunch is reduced by

$$\Delta E_{pot} = q \cdot (U_{high} - U_{low}) \tag{3.3}$$

and a re-acceleration when leaving the PDT is suppressed.

Detailed simulations of the pulsed drift tube are described in [Smo12]. Two main sources of ion losses were identified, excessive bunch length and pulsing duration. As an ion passes the PDT within 4 µs the transmission of ion bunches decreases if their length exceeds 4 µs. Transmission efficiencies of 35 % to 70 % were simulated for ion bunches of 5 µs to 2 µs bunch length, respectively. In the same manner, if the pulse down of the PDT takes longer than a few µs, ions will not be fully decelerated, therefore cannot be captured within the Penning traps. A capacity measurement

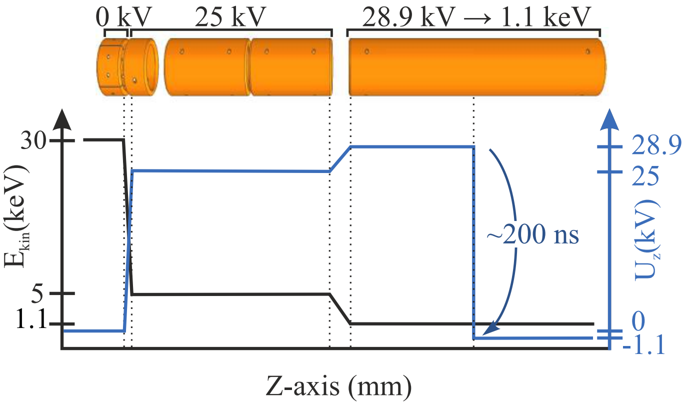

Figure 3.14: Potential within the deceleration stage (blue) as well as the kinetic energy of the ion bunches (black).

yielded $C_{PDT} = 41\,\mathrm{pF}$ for which transient times shorter than 200 ns are expected, eliminating this source of losses. It was shown in its commissioning [Bey14a], that this deceleration device is able to slow down ion bunches, albeit with a very low efficiency. These results will be compared to values taken within this work in sec. 4.1.

3.7 Double Penning-trap setup

The cooled, pulsed and decelerated ion bunches with a kinetic energy of 1.1 keV are guided successively into two separate traps, which have been designed within [Web03] and installed at TRIGA-TRAP since 2007 [Ket08]. A technical drawing of the double trap setup, which is located within a vacuum tube inside of a superconducting 7 T magnet, is shown in fig. 3.15. The trap electrodes are surrounded by a liquid nitrogen cryostat to enable cooling to a temperature of 77 K. During the measurements presented within this work, the traps have been operated at room temperature. The first trap has cylindrically shaped electrodes with a total length of 212.5 mm and an inner diameter of 32 mm to gain a high pumping cross-section that ensures a comparatively low pressure during operation. Since it is loaded with a He gas flow rate of $2 \cdot 10^{-5}$ mbar·l/s to enable mass-selective buffer gas cooling (see sec. 2.3.1), it is called *purification trap*. Its ring electrode is separated into four segments to allow ion manipulation by dipolar and quadrupolar RF excita-

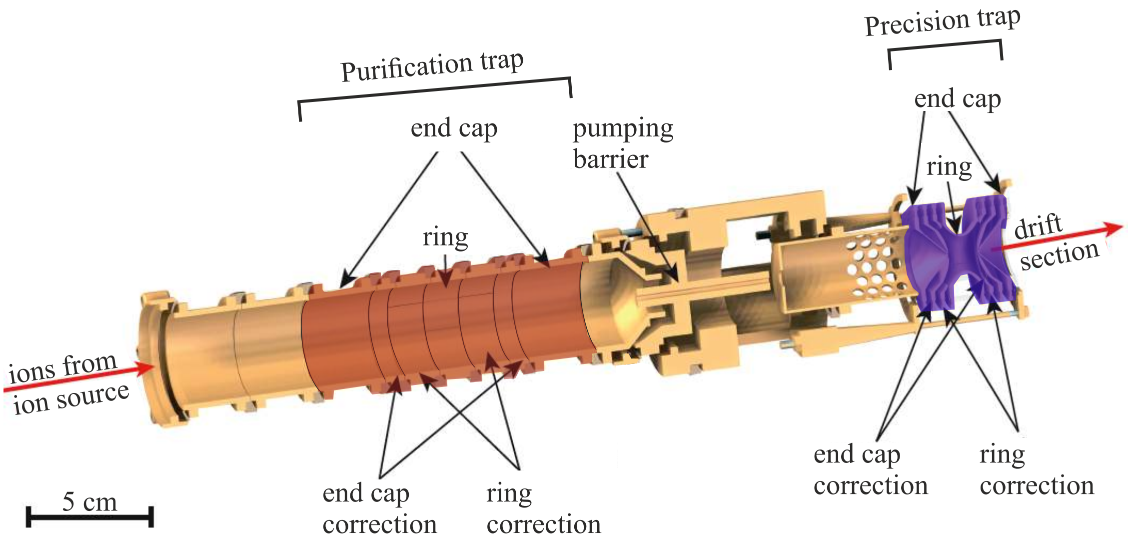

Figure 3.15: Technical drawing of the Penning-trap system installed, adapted from [Eib13]. Ions leaving the PDT enter the cylindrically shaped purification trap (red) from the left. After mass-selective buffer gas cooling within the purification trap, they are injected into the precision trap (purple). For more details, see text.

tions. After centering the ion species of interest, they are ejected through a small aperture and guided to the subsequent hyperbolical precision trap, which is placed 20 cm apart from the first trap, through a pumping barrier with a length of 50 mm and an inner diameter of only 1.5 mm. Due to the pumping barrier, only centered ions can be transmitted from the purification to the precision trap while contaminants are lost at the funnel. Simultaneously the pumping barrier reduces the helium flow into the latter and thereby ensures a low pressure, which is crucial for mass measurements [Nei08] since ion-gas collisions have to be excluded. To achieve an appropriate selection quality inside the purification trap it is also of major interest to avoid overloading this trap with unwanted ions. The precision trap itself has a hyperbolical shape and is designed for maximum electrical field homogeneity and minimum perturbation of the magnetic field. It is used to prepare ions for measurement of the cyclotron frequency via the ToF-ICR technique, PI-ICR or in the future FT-ICR. The size has been kept small in order to trap the ions inside the localized homogeneous field region of the magnet. Thus its inner volume has an axial length of only 11 mm with an inner diameter of 12.76 mm. For injection and ejection of the ions, small holes with a diameter of 1.2 mm are drilled into the endcaps. Like the purification trap, the ring electrode is split into four segments to enable an ion motion manipulation. The two traps have in common that they use correction electrodes to compensate minor field imperfections like the ones caused by the entry and exit orifices. Both the purification trap and the precision trap, as well as the remaining electrodes are made of oxygen free high purity copper, due to its high thermal and electrical conductance as well its low magnetic susceptibility. In addition, they are gold coated to prevent oxidization which could lead to non-conductive patches on the surfaces. The electrodes are electrically separated by sapphire insulators. Subsequently attached to the precision trap is the final drift section to guide the ions onto the MCP detector, which is located 1.2 m outside of the magnet housing.

As introduced in sec. 2.3.2 the mass of an ion can be determined by its cyclotron frequency (eq. 2.13) with a high precision. During these measurements systematic or time-dependent effects have to be considered, since they influence the cyclotron frequency and thereby the determined mass values. One option to avoid these effects is the calibration of the magnetic field strength $\vec{B}$. An elegant method is the measurement of the cyclotron frequency ω_{ref} of a stable nuclide with a well-known mass m_{ref} in alternation to the investigation of the ion of interest. Thus the mass of the probed atom m_{atom} can be calculated by

$$m_{atom} = \frac{\omega_{c,ref}}{\omega_c}(m_{ref} - m_e) + m_e \tag{3.4}$$

with the corresponding uncertainty

$$\Delta m_{atom} = \frac{\Delta \nu_c}{\omega_c + \Delta\omega_c}(m_{ref} - m_{atom}) \tag{3.5}$$

For offline measurements at TRIGA-TRAP, carbon clusters provide the reference mass of choice, since the unified atomic mass unit is defined as 1/12 of the mass of ^{12}C. They are produced by laser ablation inside of the so-called *mini-RFQ* [Sch16], which is mounted perpendicular to the trap beamline. During online operation, it is intricate to switch to this ion source, as it requires strongly differing transport voltages along the beamline. Thus in the present work, the employed mass reference is ^{88}Sr, which is commonly occurring as traces in, e.g., metallic components of the setup or is introduced to the system as contamination. The ionization potential is low enough to generate an appropriate ion beam within the surface ion source, whereby the current is sufficiently high to enable rapid recording of reference resonances. The separate time settings used during each measurement cycle presented within this work, are listed in table 3.4.

Table 3.4: Operation parameters during measurement procedure

Purification trap capture	96 µs
Axial and cyclotron cooling	30 ms
Dipolar magnetron excitation	20.1 ms
Quadrupolar cyclotron excitation	500 ms
Axial and cyclotron cooling	50 µs
Purification trap ejection	50 ms

3.8 Instruments for monitoring and quality assessment

For every experiment, especially after major modifications, having extended knowledge about the performance is of utmost importance. Beside determination of all partial efficiencies, properties of the ion beam are also relevant. Although there are plenty of parameters to describe a particle beam [Str92], decisive characteristics for the performance of TRIGA-TRAP are the shape of the beam profile and the intensity of the ion current. Additionally, instruments for beam monitoring are used for adjustment of the ion beam. Depending on the ion current and isotopic composition, different methods come into consideration: Faraday cups are used to quantify the current carried by the ion beam whereas γ-measurements of fission product collections yield detailed information about the amount of individual radionuclides. To detect low ion currents and estimate the beam shape, multichannel plate detectors (MCP) combined with a phosphor screen are the method of choice. A schematic drawing of a diagnostic station comprising a Faraday cup and an MCP/phoshpor screen-combination is pictured in fig. 3.16.

Several positions for both quantitative and qualitative beam diagnostics available at TRIGA-TRAP are shown in fig. 3.2. The utilized methods are discussed in detail below.

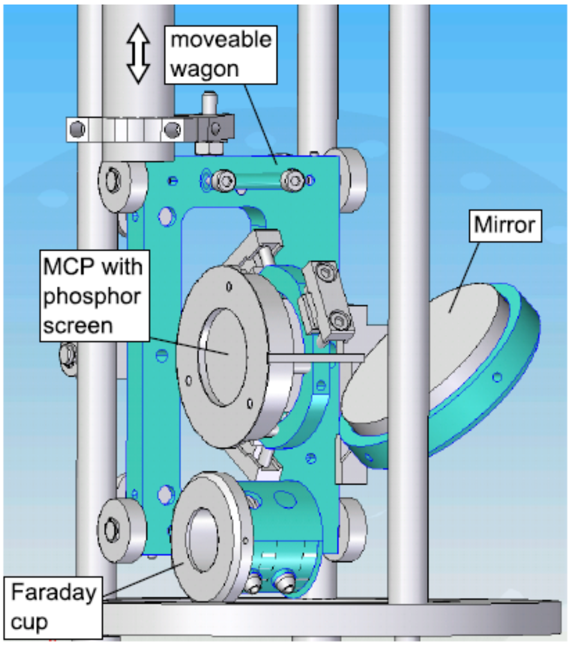

Figure 3.16: Detection stage employed at TRIGA-TRAP [Bey14a]. It comprises a Faraday cup and an MCP with phosphor screen.

3.8.1 Qualitative techniques

Multichannel plate (MCP) detectors are an excellent choice for ion currents below 1 pA. They consist of 10^4 - 10^7 parallel electron multipliers, each with an inner diameter of 10 µm to 100 µm. They are arranged perpendicular to the surface with a small angle of 8° [Wiz79]. The front and the back surfaces are metal coated and serve as electrodes. A voltage of around 1000 V to 1800 V is applied between the two surfaces, thus impacting electrons create a cascade of secondary electrons when hitting the channel walls. The magnitude of the resulting electron current produced by one ion depends on the voltage and the channel geometry, but is usually in the order of 10^3. Most MCP detectors are assembled in a chevron shape, i.e., one plate is mounted on top of the other with angled channels rotated 180°from the other. This MCP geometry produces a significantly higher gain of up to 10^6 secondary electrons per ion. After releasing an electron avalanche, the channel walls must be replenished, which takes several milliseconds. Within this period additional signals cannot be detected, thus this time is called "dead time". The efficiency for positive ions of an MCP depends on their kinetic energy and on the plate voltage. Thus, its value is in the range of 30 - 80% depending on the ion energies [Fra02]. A combination of an MCP and an additional phosphor screen behind allows the visualization of the spatial distribution electron avalanche, and therefore the original beam shape. A voltage of about 1200 V is applied to the phosphor screen, thus every electron impact on the surface induces the emission of several hundred fluorescence photons, thereby creating a picture of the beam shape respectively its intensity distribution. A CCD camera outside of the vacuum chamber records this picture via a mirror. The active area on the phosphor screen is a circle with a diameter of 25 mm, thus the size of the ion beam can be determined. At TRIGA-TRAP, this kind of MCP/phosphor screen-combination is mounted on remote controllable motorized feedthroughs in front of the RFQ, behind the RFQ and behind the PDT. The use before mass separation, i.e., in between the ion source and the dipole magnet, is not advisable due to the high sensitivity of the screen and its poor tolerance of highly intense ion beams. The absolute rate of ions in the beam cannot be determined due to unknown and inhomogeneous deterioration of the phosphor screen. For this reason MCPs are deployed only for qualitative purposes.

3.8.2 Quantitative techniques

An easy and simultaneously highly sensitive way for quantifying ions in a beam is the usage of a so called Faraday cup, which can be inserted into the beam as necessary. It is considered a universal charge detector since it is a robust device, enduring high ion currents, independently from the energy or mass of the investigated species. The design of a Faraday cup is rather simple: It consists of a conductive metal electrode which is electrically insulated from the outer shielding and connected to ground potential through an ampere meter. Ions entering the cup are absorbed and induce a charge drain. The resulting current can be measured by a highly sensitive ampere meter and used to determine the number of ions entering the cup. Assuming that ions produced by surface ionization are singly charged, 1 A corresponds to

$$1\,\mathrm{A} = 1\,\mathrm{C/s} = 6.242 \cdot 10^{18}\,\mathrm{e/s} = 6.242 \cdot 10^{18}\,\mathrm{ions/s} \tag{3.6}$$

with the elementary charge $e = 1.602 \cdot 10^{-19}$ C. To avoid the detection of emitted secondary electrons and thereby introducing systematic errors, a ring electrode on a negative potential (-50 V to -100 V) is added in front of the measurement electrode to repel these electrons back to the cup.

Faraday cups are part of beam diagnostics stages that are installed at four different positions of the TRIGA-TRAP beamline as indicated in fig. 3.2: The first one (FC0) is located behind the ion optics. It provides the largest signal as the beam is not yet mass separated. It can be used to quantify the total amount of ionized atoms, but is rather an examination for axial injection of the beam into the dipole magnet. The second Faraday cup (FC1) is located behind the mass separation, more precisely in front of the RFQ. By slowly increasing the current of the dipole magnet and simultaneously measuring the Faraday cup current, a mass spectrum can be recorded, giving detailed information about the constituents of the ion beam. A third Faraday cup (FC2) is installed directly behind the RFQ for determining the transmission of the RFQ as well as the size of an ion bunch. The last Faraday cup (FC3) is placed behind the pulsed drift tube and is the last monitoring facility before injection of the ions into the purification trap.

To obtain detailed information about quantities of different radioactive ion species at the same time, an applicable method is the collection of fission products on a backing material. Radionuclides are accumulated over a well defined time and measured in a GeLi-γ-detector after an appropriate cooling time, which mainly depends on the time required to dismount the sample and place it in front of the γ detector. By knowledge of the timings, the γ-line intensity of the nuclide of interest, its half-life and the efficiency of the detector, the quantity of radioactive ions can be calculated. The accumulation time is adapted to the expected amount of activity and the half-lives of the investigated isotopes. To get a distinct starting point for the collection, the beam is either guided onto the backing material or the backing material is moved into the beam by a manual feedthrough at a specified time. The various positions for this kind of data acquisition within the gas-jet are indicated in fig. 3.2. During a fission product collection inside the target chamber the backing material of choice is PTFE. Its neutron capture cross section is low and ensures a low activation of the material during its exposure to the high neutron flux inside the reactor. A 22 mm PTFE plate with a thickness of 0.5 mm is also stable and can easily be attached to the target and accordingly quickly dismounted after radiation. The conditions for efficiency studies within the gas-jet differ. Thus a different backing material has to be chosen. Fission products adsorbed to large aerosol particles are comparably slow or rather have a low kinetic energy. It also has to be taken into consideration that the insertion of a backing plate represents a pumping barrier which could lead to significant pressure increases. Due to these demands, glass fiber filters are used to collect fission products from the gas-jet since its permeable structure does not disturb the gas flow significantly. Aerosol particles accumulate loosely inside the filter structure, whereas the carrier gas mostly pervades and the pressure raise remains in an acceptable range. For fission product collections after ionization the backing material has to be exchanged by a more resistant substance. Therefore, aluminium is established as backing material for collections behind the ion source, since it is conductive and will not be charged up when collecting ions. Furthermore, the kinetic energy of the ions is high enough for them to permanently implant into the foils.

The minimum half-life of measurable nuclides is limited by the time required for dismounting and transfer to the γ detector. Venting and opening the setup needs a lot of time, especially when the ion source is running and has to be cooled down first to prevent oxidation processes at the hot tungsten surface of the filaments. Thus three "catching stations" have been designed and implemented successfully. A schematic sketch of the setting is shown in fig. 3.17. They are located in front of the dipole magnet and the RFQ as well as behind the RFQ.

An Al-foil can be inserted into the ion beam by loosening the fixation of the linear manipulator and sliding it into the vacuum chamber. As the aluminium reaches the center of the beam, the collection time starts. After a certain time period (1 to 10 min), the manipulator is pulled out, the gate valve is shut and the Al containing fission products can be removed from the top. Thus opening and venting the complete setup is avoided and the time from end of the beam implantation to start of the γ measurement can be reduced down to one minute. This gives both access to short lived isotopes and enables collecting more data in the same time.

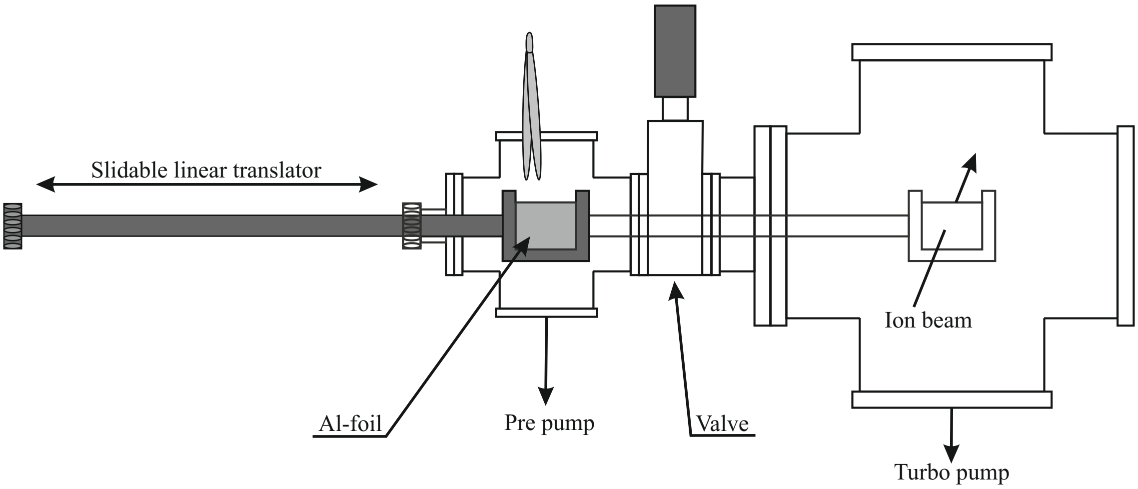

Figure 3.17: Schematic drawing of a catching station, employed at TRIGA-TRAP. The aluminium foil can be inserted into the ion beam by a slidable linear translator and afterwards removed with tweezers while venting only the small vacuum chamber.

Chapter 4

Measurements and results

One of the main goals of TRIGA-TRAP is the mass measurement of short-lived nuclei produced by neutron-induced fission of a target, placed near the reactor core. Within this work extensive characterization studies of the gas-jet and the whole experimental beamline have been made in order to optimize its performance. Moreover, a new surface ion source has been installed to increase the intensity of the generated ion beam. The performance of the new designed ion source has been optimized and enables ionization studies. After subsequent beam profile characterization, these efforts resulted in the first mass measurements of short-lived fission products performed within the purification trap.

4.1 Characterization of gas-jet and beamline

In the following section studies of fundamental properties of the gas-jet are described. It begins with the introduction of the general measurement and evaluation procedure. Subsequently extended efficiency studies are presented, comprising the individual transmission efficiencies of the beamline components as well as absolute efficiencies of the experimental setup. Furthermore determination of the absolute fission yield and the long-term stability of the gas-jet as well as transport efficiencies of fission products through the experiment and transport time measurements are discussed. Finally measurements of the transport time of the gas-jet are shown, which represents a crucial parameter to evaluate the performance.

4.1.1 Efficiency studies

Measurement procedure

To characterize the redesigned beamline, major efficiency studies were mandatory. Since TRIGA-TRAP works with radioactive nuclei the consequences of fission can be exploited to verify the performance of the whole setup as well as of individual components. For this purpose, fission products have been collected on a backing material at different stages of the experimental setup as indicated in fig. 3.2. After a predefined collection time ("collection time"), the sample containing the radio nuclei has been removed from the collecting position and placed in front of a GeLi-detector in a defined distance ("decay time") for a subsequent γ-ray measurement ("recording time"). The backing material had to be matched to the given circumstances as already discussed in sec. 3.8.2. The chosen materials for fission product collections at different positions are listed in table 4.1. For the so-called "100 %-catch" a PTFE plate has been placed directly onto the covered target material, assembled into the target chamber and inserted into the reactor via beam port A for a subsequent irradiation. Due to radiation safety issues, this catch is performed at a reactor power of only 10 kW. During this time produced fission products recoil of the target and implant into the backing material. After removing the target chamber out of the beamport, the PTFE plate is disassembled and placed in front of the GeLi-detector. Results of this 100 %-catch will be presented in sec. 4.1.2. During collections at the positions "DC","pre lens" and "pre IS" aerosol particles have been accumulated inside a glass fiber filter. These fission product collections are time-consuming as the first part of the beamline up to the dipole magnet has to be vented to remove the filter. Especially the "pre IS" collections are elaborate since several flanges have to be opened, i.e., the connection between the ion source and the aerodynamic lens. For collections behind the ion source aluminium foils are introduced as backing material as the kinetic energy of the ions is large enough to implant into the foil. The implementation of three catching stations (see sec. 3.8.2) enables a rapid removal of the aluminium foil and thereby frequent fission product collections at these positions.

The collection, decay and recording times were adapted to the expected amount of nuclei as well as to the half-life of the observed species. The time required for sample extracting and its transport to the detector were considered as well, which mainly sets a lower limit on the decay time, depending on the collecting position. By implementation of three catching stations, this limit could be significantly lowered for these positions compared to previous beamtimes [Ren16]. The minimum decay time of “post IS” collections amounts to five minutes, since the beam diagnostics station “post IS” is located inside of a high voltage cage, but usually a longer decay time of 30 min had been employed. For security reasons the high voltage as well as the extraction electrode have to be shut off before entering this area. Detailed time parameters, used within the latest measurement campaigns, are listed in table 4.1. Such measurements have been made several times to verify the efficiency of each experimental section and obtain appropriate statistical significance. During each measurement series the chosen conditions have been kept constant in order to gain a direct comparability between the collections. Results will be presented in sec. 4.1.4.

Evaluation procedure

For characterization purposes, relative efficiencies as well as absolute count rates of radionuclides are of major interest. The former demands identical conditions during a measurement series, such as collecting-, decay- and recording-time. The recording conditions, i.e., the sample geometry and the distance between the sample and the detector, have to be equal as well to eliminate systematic deviations. On the contrary, determination of absolute count rates requires the preparation of the γ detector and subsequent calculations: before each measurement campaign, the detector was calibrated with a standardized sample in order to verify the energy

Table 4.1: Time parameters used for collecting fission products for subsequent γ-measurements during the latest measurement campaigns.

Position	Collection time (min)	Decay time (min)	Recording time (min)	Collection type
target chamber	30	30/46	30	recoils in PTFE
pre lens	10	30	10	aerosol on filter
pre IS	10	30	10	
post IS	10	5/30	10/30	ion implantation into Al
pre RFQ	5	1	5	
post RFQ	5	1	5	

as well as the energy dependent efficiency. For this purpose the certified QCY48-γ-standard has been used that contains certified amounts of ^{241}Am, ^{109}Cd, ^{57}Co, ^{139}Ce, ^{203}Hg, ^{113}Sn, ^{85}Sr, ^{137}Cs, ^{60}Co and ^{88}Y, which decay by α or β decay in which they release γ rays with energies in the range of 60 keV to 1836 keV. Since the detector efficiency is influenced by geometrical parameters, i.e., the distance between sample and detector, these calibrations are mandatory for each sample position used. To reduce additional systematic deviations caused by self-absorption, the sample geometry of the standard was adapted to the future sample geometry. Thus, 50 µl of the standard solution has been dropped onto a fibre glass filter yielding a source with a geometry similar to that of the following fission product collections. A short recording time of 30 minutes was sufficient to get significant signals. The calibrations as well as γ measurements have been recorded and evaluated with Genie2000. As already mentioned, verification of absolute ion numbers at the observed positions is of major interest for subsequent mass measurements, and were therefore evaluated. Within this procedure several aspects were considered like the intensity of the observed γ line, the corresponding detector efficiency at this energy and decay of the isotope during collection, decay and recording time. The isotopes that have been analysed in detail and their corresponding properties are listed in table 4.2. Some isotopes produce further γ lines, but as their intensity is either too low to get an appropriate number of counts or they overlap with other lines only significant peaks have been investigated. Rubidium and strontium are appropriate candidates for efficiency studies since their ionization potential is sufficiently low, whereby a proper countrate at every collecting spot is guaranteed. Yttrium has also been investigated as it is a daughter nuclide of the Rb/Sr-decay chains with a much longer half-lives as shown in fig. 4.1. Analysing the recorded γ spectra yields a certain amount of counts $N_{\gamma,i}$ for an investigated γ decay i. Knowing the detector efficiency $\varepsilon_{\text{det}}(E_i)$ at the energy of the decay E_i with its intensity $I_{\gamma,i}$, absolute ion rates $\mathit{\Theta}$ inside the ion beam can be calculated via:

$$\mathit{\Theta} = N_{\gamma,i} \cdot I_{\gamma,i} \cdot \varepsilon_{\text{det}}(E_i) \cdot \delta_{\text{recording}} \cdot \delta_{\text{decay}} \cdot \delta_{\text{collecting}} \tag{4.1}$$

δ_i considers the amount of ions, that already decayed during the collecting-, decay- or recording-time. This effect increases with decreasing half-life, especially at collecting

Table 4.2: Investigated isotopes with the corresponding parameters, that are used for calculation of the absolute number of atoms. Values for γ energies and their intensity are taken from [Reu83].

Isotope	Half-life	γ energy (keV)	Intensity	Detector efficiency
^{89}Rb	15.2 m	1 031.9	0.636	0.0054
		1 248.2	0.43	0.0046
^{91}Sr	9.5 h	652.9	0.08	0.0076
		749.8	0.236	0.0069
		1 024.3	0.33	0.0054
$^{91\text{m}}$Y	49.7 m	555.6	0.95	0.0086
^{92}Sr	2.71 h	241.6	0.029	0.0152
		430.5	0.033	0.0104
		1 383.9	0.9	0.0043
^{93}Sr	7.43 m	590.2	0.68	0.0082
		710.3	0.218	0.0072
		875.7	0.245	0.0061
		888.1	0.221	0.0060
		1 269.5	0.071	0.0046
^{94}Sr	76 s	1 427.7	0.942	0.005
^{93}Y	10.18 h	266.9	0.073	0.0143
		590.24	0.998	0.0082
^{94}Y	18.7 m	550.9	0.049	0.0087
		918.74	0.56	0.0059
		1 139.9	0.06	0.0050

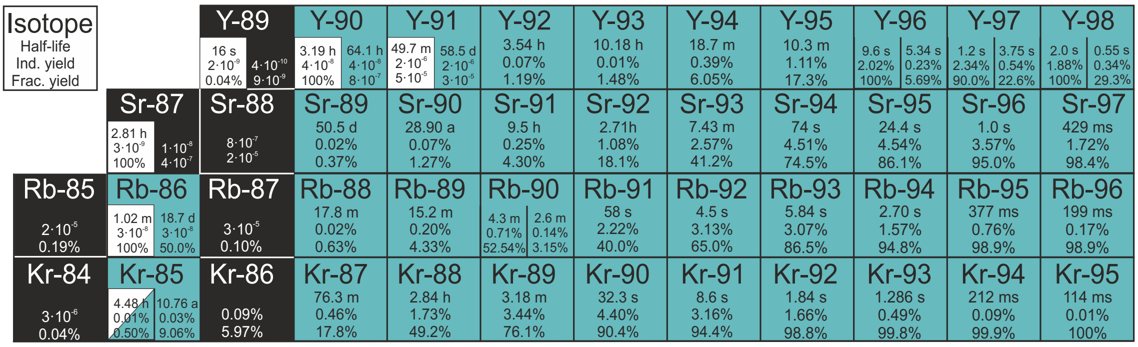

Figure 4.1: Cut-out of the chart of nuclei. For every shown isotope the half-life, the independent fission yield and the fraction of the cumulative yield, which is produced as a primary fission product, are listed. Data are taken from [Kat11, Kat16].

times longer than one or two half-lifes. For calculation of atom or ion rates Θ, the transmission efficiencies of the individual components τ_i up to the location of interest have to be considered. Behind the surface ion source the ionization efficiency I_{eff} of the investigated species has to be taken into account as well:

$$\Theta = \Gamma(Z,N) \cdot \tau_{\text{target cover}} \cdot \tau_{\text{gas-jet}} \cdot \tau_{\text{lens}} \cdot I_{\mathit{eff}} \cdot \tau_{\text{extraction}} \cdot \tau_{\text{magnet}} \cdot \tau_{\text{RFQ}} \cdot \tau_{\text{PDT}} \tag{4.2}$$

Here, $\Gamma(Z,N)$ denotes the fission yield of a certain nuclide.

Nevertheless, it is not possible to calculate independent ion numbers for Rb and Sr decay pairs from the detected γ signal in cases where a direct detection of the Rb beta decay is not feasible due to a too short half-life. Here, the γ signal of the Sr beta decay originates both from Sr atoms as well as twice decayed Rb atoms. To deconvolve these two at least the ion ratio of Rb/Sr is required. This ratio is known for the production by ^{235}U fission inside the target chamber. It is in the order of unity for A=92 to A=94 as illustrated in fig. 4.1 with the fractional yield, that represents the ratio of independent fission yield to the total cumulative yield. The Rb/Sr ratio already changes during extraction and transport out of the target chamber to the ion source, due to differing half-lives. This additional factor has a large uncertainty for short-lived isotopes because of the difficult to determine mean transport time and distribution. To at least give an estimation for the ion rates in these cases, the analysis was performed under negligence of these precursor effects. The resulting numbers do not necessarily represent the actual ion rates but allow comparing between fission product collections with different time-cycles. However, this precursor effect does not affect relative efficiency studies, but poses a problem for determination of absolute ion rates for isotopes with Z ¿ 37.

Besides γ lines from nuclides of interest plenty of others can be identified within a recorded spectrum (see fig. 4.2). The detector is located inside of the reactor hall close to the reactor, thus typical background peaks occur. One example is the so-called annihilation-peak at an energy of 511 keV, caused by pair production due to high-energy photons. Another observable isotope is ^{41}Ar (1293 keV), produced inside of the reactor hall by neutron activation of ^{40}Ar, which has an abundance of 0.93% in air. Natural ^{40}K or ^{40}K produced by neutron-activation, can also be seen in almost every recorded spectrum. If the background is low enough, several lines produced by natural decay chains are observed. Their intensity is low and remains constant independent from experimental conditions. Furthermore significant peaks from Tc and Mo occur in the recorded γ spectra of samples collected before ionization. But since their ionization potential is rather high (Tc: 7.28 eV / Mo: 7.099 eV), they are not ionized appreciably within the surface ion source and cannot be used for efficiency verifications or commissioning purposes.

4.1.2 Absolute rates of fission products

To determine the total number of produced fission recoils inside the target chamber, a 100%-catch has been made with the targets B and D (see table 3.1). As the amount of ^{235}U in target B practically equals that of target C, the 100%-catch of target B is representative for both targets. The mass of fissionable ^{235}U inside the two other targets amounts to 1258 µg in B and 1440 µg in D, respectively. As their uranium content differs by 14 %, an increase in the fission yield of this factor is expected and will be verified in the following. The PTFE plate has been irradiated inside the target chamber for 10 minutes at a reactor power of 10 kW$_{\text{th}}$. After a decay time of 30 min at target B and 46 min at target D, respectively, the PTFE plate has been put into a GeLi-detector and been measured for 30 minutes (real-time). The energy-calibrated γ-ray spectrum of target D is shown in fig. 4.2, in which the investigated γ-ray signals are labeled below the spectrum. Other significant peaks that are denoted above have not been investigated since they represent background radiation or their importance for subsequent collections is low. Since the decay time of this collection amounted to 47 min, short-lived nuclides already decayed and cannot be seen within this spectrum. The reactor is regularly operated at a power of 100 kW$_{\text{th}}$ but the 100 %-catches have been made at a reduced reactor power of 10 kW$_{\text{th}}$, the absolute count numbers extracted from this data were multiplied with the factor 10 to enable direct fission collection comparisons and determination of absolute efficiencies. The production rate of a certain nuclide $\mathit{\Gamma}(Z,N)$ scales linearly with the neutron flux:

$$\mathit{\Gamma}(Z,N) = N \cdot \sigma_f^{235} \cdot \Phi \cdot Y(Z,N) \tag{4.3}$$

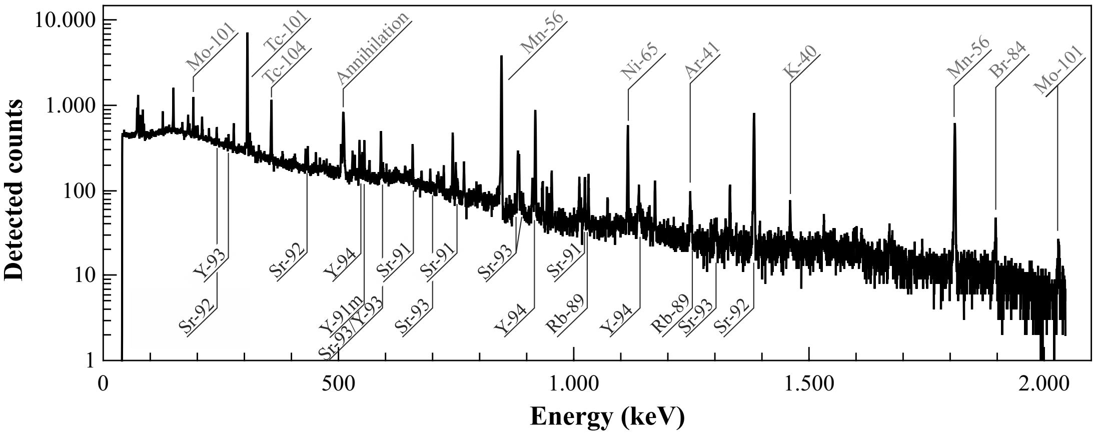

Figure 4.2: Recorded γ spectrum of the 100%-catch made with target D. Decay energies belonging to ions of interest have been marked below the spectrum whereas other significant energies are labelled above.

$Y(Z, N)$ is the independent fission yield of a certain nuclide. This equation shows that the presumed production rate at a reactor power of $100\,\mathrm{kW_{th}}$ can easily be calculated. The corresponding ion rates for both targets are listed in table 4.3. The obtained yields match those of previous experiments [Smo12, Ren16], although they are much smaller than the theoretical yields due to necessity of the products to recoil out of the target. The data also demonstrates that an increase of 14 % in fissionable material increases the ion rates by the same factor, i.e., by average 19 %.

Table 4.3: Ion rates inside the target chamber extracted from collections made with targets B and D, normalized to a reactor power of $100\,\mathrm{kW_{th}}$. The γ peaks of the bold isotopes have been evaluated. Their precursors, which contribute to the investigated peaks, are listed as well.

Isotope(s)	Target B (2015) # Ions (1000/s)	Target D (2017) # Ions (1000/s)
$\mathbf{^{89}Rb}$	37(2)	36(3)
^{91}Rb + $\mathbf{^{91}Sr}$	60(7)	68(8)
^{91}Rb + ^{91}Sr + $\mathbf{^{91m}Y}$	35(2)	48(3)
^{92}Rb + $\mathbf{^{92}Sr}$	288(32)	302(18)
^{93}Rb + $\mathbf{^{93}Sr}$	6(1)	8(2)
^{93}Rb + ^{93}Sr + $\mathbf{^{93}Y}$	236(42)	345(55)
^{94}Rb + ^{94}Sr + $\mathbf{^{94}Y}$	196(10)	207(23)

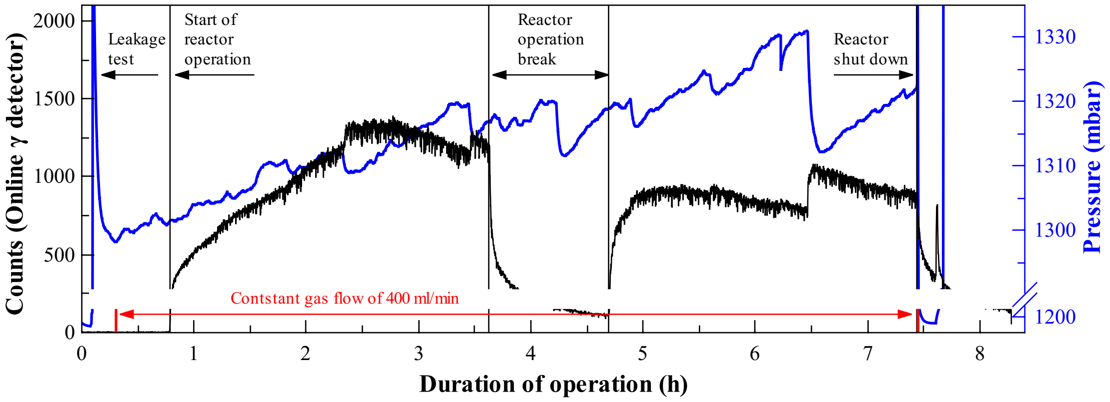

Figure 4.3: Temporal evolution of the target chamber pressure (blue) and recorded counts on the online γ-ray detector (black).

4.1.3 Investigation of the gas-jet behaviour

By implementation of the online γ-ray detector (see sec. 3.1) the long-term stability of the gas-jet system can be investigated in detail. Besides detection of the transported activity during beamtimes, the pressure within the target chamber has been monitored and recorded as well. This combination offers the chance to investigate the gas-jet system more accurately than ever before. Previously it was assumed that the pressure within the target chamber remains constant during the day. This assumption was based on a formerly used analogue manometer with a comparably rough scale (100 mbar per scale division) that has been read out twice a day. This hypothesis has now been disproved by continuously monitoring the pressure inside the target chamber. A typical development of the detected activity on the γ-ray detector in connection with the target chamber pressure is shown in fig. 4.3. The recorded activity on the γ-ray detector (black line) clearly depends on the reactor operation. When it is not operating, the detected signal is extremely low (before operation). After reactor shut off, e.g., during reactor operation break or after a day of operation, the signal drops instantly to several hundred counts per second and then decreases slowly to zero. At the beginning of reactor operation it increases steadily over around one hour. This behaviour is observed every day and might be caused by an accumulation of charged particles onto the inner capillary walls. During operation the signal behaves unsteadily and also shows some sudden increases.

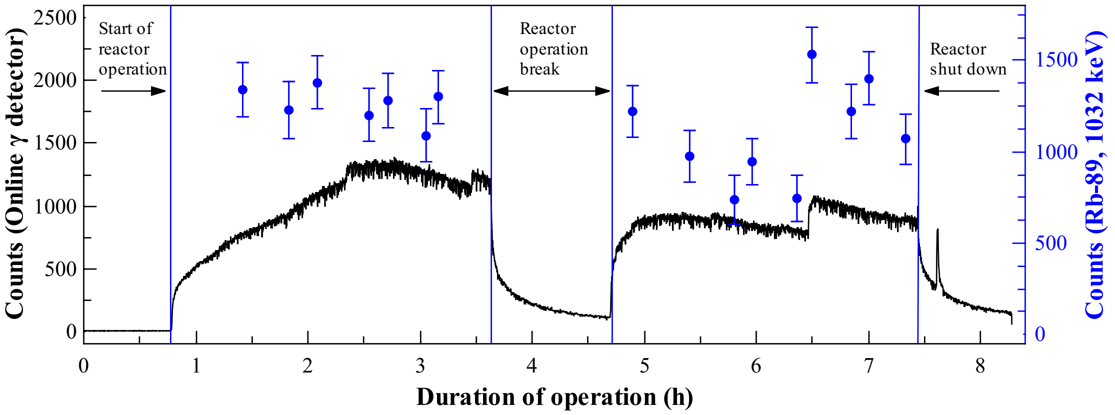

Figure 4.4: Temporal evolution of the recorded signal of the online γ-ray detector and the ^{89}Rb (1032 keV) signal of fission product collection performed in "pre RFQ".

The blue curve shows the pressure development inside of the target chamber. The high peak at the beginning of the plot represents the leakage test that has to be performed each day before reactor operation in order to proof the leak tightness of the target chamber. For this, a test pressure of 2.5 bar is applied to the system, whose decrease is monitored for several minutes and has to be smaller than 1 mbar/min.

Afterwards the routine operation mode with a continuous gas flow of typically 400 ml/min is started, generating a pressure of 1.3 bar. At the end of a measurement day the gas flow is increased again in order to accelerate the cooling of the aerosol oven. During the day the pressure inside of the target chamber increases by around 30 mbar. Although this quantity is comparably low, it seems to affect the transported activity. As the pressure increases, the detected γ signal decreases and vice versa. Without any changes in the operating conditions, a sudden drop in pressure occurs after 6.5 h. It could be induced by a release of CdI_2 deposit that formerly inhibited the gas flow and thereby increased the pressure inside the target chamber. The temporal evolution of the γ-ray signal recorded by the online detector and the amount of transported fission products is depicted in fig. 4.4. The blue data points represent the results of several fission product collections, made in front of the RFQ. The collection-decay-recording time sequence was 5 min-1 min-5 min at standard operating conditions. The mass separator was set to mass 89, thus the strongest γ-ray signal of ^{89}Rb at 1032 keV has been evaluated. There is clearly a significant correlation between the amount collected fission products and the strength of the γ detector signal. As the latter decreases the transport efficiency decreases likewise and vice versa. Also the sudden rise after 6.5 h can be seen in these collections, thereby supporting the assumption of a released salt deposit or rather the elimination of a minor blockage. This comparably small signal increase of 2 % that correlates with a pressure change of 30 mbar results in an efficiency gain of a factor two. As there is a strong correlation between the discussed parameters, the target chamber pressure respectively the signal on the online detector can give information about the development or rather the quality of the fission product transport efficiency. It also explains occurring fluctuations in the fission product yield that have been observed in previous beamtimes during both daily measurements and in between individual days [Ren16, Gün93]. Moreover, the general quality of the gas-jet also differs from day to day. This illustrates the importance of a gas-jet calibration to gain comparability between several measurements.

4.1.4 Transport efficiencies

To extract the produced fission products out of the target chamber and transport them to the experimental setup, an aerosol-based gas-jet system is used. Since a gas-jet requires regular maintenance, it is of certain interest to prove that this is an efficient method which is worth the effort. Thus the transport of fission products to the aerodynamic lens has been investigated, once with the commonly used aerosol, containing nitrogen and CdI_2 particles and once with pure nitrogen as carrier gas. The corresponding γ spectra are shown in fig. 4.5. All other parameters of these two measurements were identical, like the gas flow rate of 400 ml/min, the carrier gas itself, collection, decay, and recording time or preparations of the filter. Nevertheless it is obvious that the transport efficiency is increased by two orders of magnitude by adding aerosol particles. Only the most distinct γ-ray signals of the most abundant isotopes can still be found within the recorded spectrum of the collection performed without aerosol particles. Omitting these peaks, the red line represents the typical background inside of the experimental hall during reactor operation. With this proof of principle, upcoming measurements have been made with the aerosol-loaded gas-jet.

To characterize the performance of the TRIGA-TRAP setup, two quantities are of

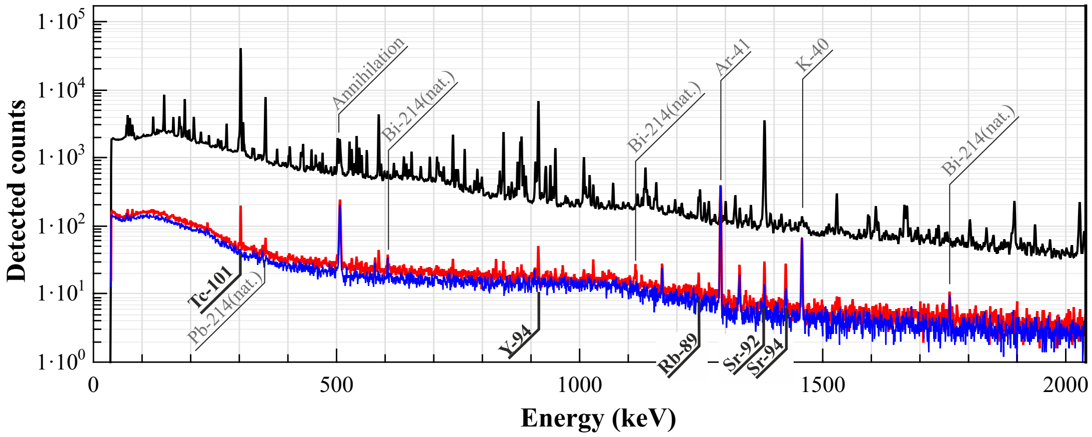

Figure 4.5: Recorded γ spectra of fission products, collected in front of the aerodynamic lens. The carrier gas was pure nitrogen (red) or nitrogen loaded with aerosol particles (black). The blue spectrum shows the background signal, recorded during reactor operation.

major interest: the transmission of individual components τ_{part} to maximize their performance or identify bottle necks within the setup, and the total transport efficiency $\varepsilon_{\text{part}}$ through the beamline to a certain point. The latter results from the product of separate transmission efficiencies, e.g.:

$$\varepsilon_{\text{RFQ}} = \prod^{n} \tau_{\text{n}} = \tau_{\text{gas-jet}} \cdot \tau_{\text{aerod.lens}} \cdot \tau_{\text{IS}} \cdot \tau_{\text{magnet}} \tag{4.4}$$

For detailed verification of individual transmission efficiencies, numerous fission product collections at different stages of the experimental setup as indicated in fig. 3.2 were performed in the framework of several beamtimes (June 2016 to August 2017). The resulting γ-ray spectra were analysed, i.e., every γ line listed in table 4.2 has been evaluated. Afterwards the results have been averaged and compared with a corresponding collection performed at different position. By the large amount of considered isotopes and many collections, statistical deviations were reduced significantly. Table 4.4 shows the resulting values for the transmission of the aerodynamic lens, the ion source (IS), the magnet as well as that of the RFQ during its operation in either continuous (cw) or bunched mode. The listed efficiencies refer to a gas flow rate of 400 ml/min, an oven temperature of 290 °C with CdI_2 as aerosol material and an ion source temperature of 1900°C. The calculated transmission of the latter refers to rubidium that is assumed to be ionized with 100% efficiency at this temperature (see sec. 2.2). Further ionization studies are discussed within sec. 4.2.3.

During data taking it was already apparent that the performance of the gas-jet was suboptimal. Its transport efficiency of 17.7(4) % is quite low in comparison with earlier measurements that had been made with the former aerosol inlet / ion source combination, but otherwise with the same gas-jet. In 2015 investigations at identical experimental conditions yielded 37(8) % transport efficiency to the first vacuum chamber of the TRIGA-TRAP beamline [Ren16]. However, no obvious fault could be found at the components outside of the reactor, since they had not been changed at all. Maintenance on the target chamber itself was not possible because of the high radiation levels, thus the measurement campaign has been continued.

The listed value of $\tau_{\text{aerodyn.lens}}$ represents the combined transmission through lens and skimmer, since both components are permanently connected to each other within the new design and do not allow to perform a dedicated collection in front of the skimmer or behind the lens, respectively. However, the transmission through the skimmer is assumed to be about 100 % as the entrance orifice has a diameter of 4 mm, which is significantly larger than the expected diameter of the particle beam. With the previous setup the transmission of the lens amounted to 84(3) % and that of the skimmer 78(10) %, yielding a combined transmission of 66(7) % [Gru16]. By implementation of the new rectangular vacuum chamber in combination with an additional turbomolecular pump, the pressure in front of the lens has been decreased from 1.8 mbar [Gru14] to $3 \cdot 10^{-2}$ mbar. Furthermore, the pressure in front of the ion source has been reduced by three orders of magnitude from $2.0 \cdot 10^{-2}$ mbar to

Table 4.4: Determined values for the transmission of single stages τ_{part} and absolute transport efficiencies $\varepsilon_{\text{part}}$ from the target chamber to the inlet of the denoted part.

Part	τ_{part} (%)
Gas-jet	17.7(4)
Aerodyn. lens	40(2)
IS	55(8)
Magnet	88(9)
RFQ_{cw}	25(4)
$\text{RFQ}_{bunched}$	38(8)
PDT	$2 \cdot 10^{-4}$

Transport to	$\varepsilon_{\text{part}}$ (%)
Target chamber	100
Aerodyn. lens	17.7(4)
Ion source	7.1(4)
Magnet	3.9(6)
RFQ	3.5(3)
PDT	cw: 0.9(1) / bunched: 1.3(3)
Purification trap	$2.6 \cdot 10^{-6}$

$3.4 \cdot 10^{-5}$ mbar, which represents optimum condition for the subsequent surface ion source. It is expected that the change in pressure strongly influences the performance of the aerodynamic lens, as introduced in sec. 2.1, potentially resulting in a transmission drop. Nevertheless, the determined transmission of $\tau_{\text{aerodyn.lens}} = 40(2)\,\%$ through lens and skimmer still amounts to a decent value. The surrounding conditions of the aerodynamic lens have not been optimized within this thesis as efforts on other components promised stronger effects. However, several degrees of freedom, e.g., the distance between skimmer and ion source, allow to perform optimization studies in the future. With this an improvement of the transmission to the previous values or even better seems possible.

The transmission of the ion source τ_{IS} comprises the ionization efficiency for rubidium, the extraction of the produced ions out of the source and the transport through the ion optics to beam diagnostics station (a), which is approximately one meter away from the ion source. This combined transmission is determined to be 55(8) % for the given conditions. With the already mentioned assumption of 100 % ionization rate of rubidium within the ion source, the observed loss in transmission can either be explained by absorption processes of ions within the hot cavity or an incomplete extraction of these ions. However, although the gas-jet efficiency as well as the transmission through the aerodynamic lens decreased, the total transport efficiency to the RFQ amounts to 3.5(3) %, which matches former measurements [Ren16]. It corresponds to ion rates of up to several thousand ions per second depending on the ion species.

The transmission of the RFQ has been determined for the masses 90, 91 and 93. As their difference in mass and transport properties are negligible with respect to the RFQ performance, the determined values have been averaged. The investigated transmission of the RFQ amounts to 25(4)% during continuous mode and increases to 38(8) % during bunched mode. For the first time since the TRIGA-TRAP beamline was installed, both the continuous and the bunching efficiency of the RFQ were successfully investigated using short-lived nuclides. Previous RFQ commissioning depended on light, stable nuclides (^{39}K,^{40}Ca) with which transmission efficiencies of 25 % and 54(4) % were determined for the continuous and bunched mode operation, respectively [Bey14a, Bey14b]. The difference to the values determined in this work can possibly be attributed to the lower ion mass as well as different timing parameters in the RFQ bunch mode operation. To avoid overloading the buncher and thereby broadening the bunch width, the accumulation time had to be optimized. As shown in [Bey14a] the performance gets worse at ion numbers $>10^6$, thereby limiting the accumulation time. With the previously measured bunching efficiency of 38(8) %, it is expected to produce ion bundles containing several 10^1 to 10^2 ions using an accumulation time of 95 ms or 10^2 to 10^3 with a prolonged accumulation time of 995 ms. Both amounts should be sufficient for a measurement within the purification trap.

Before entering the purification trap, the ion bunches have to pass the PDT in which they are slowed down to an energy of 1.1 keV, which generates some experimental challenges. During this process the transverse emittance of the ion bunch increases by more than a factor of 5 [Smo12], expanding the bunch shape and thereby increasing the probability of partial or even total cut off of ions by orifices along the beamline. Furthermore, the decelerated low-energy ion bunches are more sensitive to electrostatic stray fields and thus the chance of deflection is highly increased. Lastly it has to be considered that the injection efficiency into the purification trap strongly depends on the energy spread of the ion bunches. Therefore the ions have to be decelerated again to around <5 eV to match the acceptance of the trap. Thus optimization of the system proves to be difficult. During the latest beamtime around 0.3 ions per minute (see sec. 4.4) of short-lived ions were observed within the purification trap, corresponding to a transport and injection efficiency of around $2 \cdot 10^{-6}$. Due to the limited measurement time, extended tuning of this section was not possible. During former commissioning studies, measurements yielded a transmission of $5 \cdot 10^{-5}$ for the transport through the PDT with subsequent injection into the purification trap [Bey14a]. Both values are far below expectations and cannot be explained by pulse lengths alone. A thorough investigation is needed to identify the cause of this and eliminate it.

4.1.5 Gas-jet transport time measurement

The transport time of the recoiling fission products to the subsequent experimental setup is a crucial parameter (see sec. 3.1) as it limits the range of accessible nuclides. Thus extended studies have been made in order to characterize this value at different

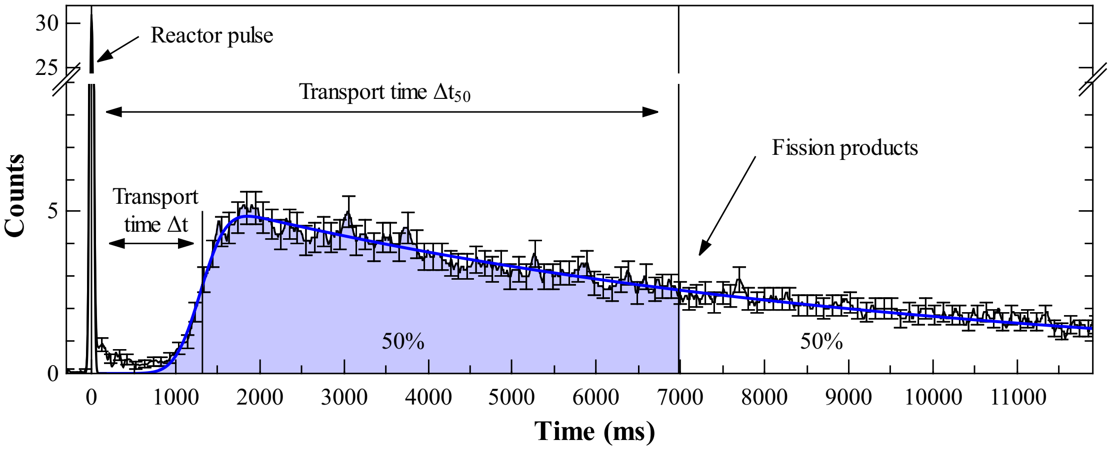

Figure 4.6: Recorded γ radiation during and following a reactor pulse at a gas flow rate of 600 ml/min. The black solid line indicate a gaussian fit for the reactor pulse, whereas the blue line represents an empirical fit for the fission products in order to determine the transport times.

experimental conditions typically employed at TRIGA-TRAP. For these transport time measurements it was exploited that the TRIGA reactor cannot only be operated in continuous mode but also in a pulsed mode (see sec. 3.1). The prompt γ rays produced by a reactor puls can be used as a distinct start signal for these measurements as fission products are only produced within this short interval. The sodium iodide-based γ-ray detector, which is installed at the capillary coming from the target chamber around two meter distant from the high voltage platform, then records the signal of the pulse as well as the signal from the transported fission products. Figure 4.6 shows a typical transport time measurement with a nitrogen gas flow rate of 600 ml/min. Without reactor operation, i.e., before a reactor pulse, the recorded detector signal is low, indicating that fission products are either not produced or not transported by the gas-jet. The time of the reactor pulse is detected by the prompt γ-radiation signal, which has an evaluated FWHM of 60 ms. It can be approximated by a Gaussian distribution due to the time dependence of the neutron flux of the reactor [Men75]. This signal represents the starting trigger with an uncertainty of FWHM/2 for subsequent transport time determinations. After a delay of several hundred milliseconds the measured radiation increases, which indicates that the produced radio nuclides have reached the detector. The recording time frame of the detector is adjusted to be 16 s in total, i.e., one data point per millisecond, to have a sufficiently high time resolution. For enhanced readability, the shown spectrum is averaged over 20 data points and only every 100th error bar is indicated. The decay of the fission product signal to background level is not completely shown in this figure because of the limited recording time. The measured signal $A(t)$ caused by the transported activity can be empirically described with a modified error function multiplied with an exponential decay:

$$A(t) = \frac{1}{2} \cdot \left(1 + \mathrm{erf}\left(\frac{t-\mu}{\sqrt{2 \cdot \sigma^2}}\right)\right) \left(\hat{A} \cdot e^{-\lambda(t-\mu)}\right) \tag{4.5}$$

The transport time Δt is defined in the following as the duration between the maximum of the prompt γ pulse and the time, when the activity of the fission products reaches 50 % of its maximum, given by μ in the fit. The other parameters represent the shape of the signal: $\hat{A}$ describes the peak activity, σ the slope of the onset and λ the decay constant. From this fit the time until 50% of the total activity is detected Δt_{50}, i.e., 50% of the total peak area, can be extracted.

This kind of measurement has been made for a set of different N_2 gas flow rates in the range of 300 ml/min to 800 ml/min. Within this measurement series a waiting time of around 20 minutes has been added between each change of the gas flow rate to ensure that the whole system has reached its pressure equilibrium. The lower limit of the gas flow rate is given by the required minimum pressure inside the target chamber, which has to be sufficiently high to thermalize the fission products, whereas the higher gas flow rate is limited by the pumping capacity of the turbo molecular pump installed behind the surface ion source. As the flow rate of the carrier gas controls the pressure inside the target chamber, the latter has also been recorded during the measurements. Each measurement has been repeated several times and the results have been averaged in order to reduce the statistical uncertainty. An overlay of the recorded data of the different measurements is shown in fig. 4.7. For clarity reasons, only data points of the averaged 400 ml/min-measurement are shown. The remaining curves indicate the $A(t)$ fits resulting from the recorded data. The intensity of the used reactor pulses is identical during each measurement, thus the height and width of the prompt γ-ray peak was equal in each spectrum. As expected, the higher the gas flow rate, the faster the velocity of aerosol particles and thus the earlier rises the signal of the fission products. Detailed results

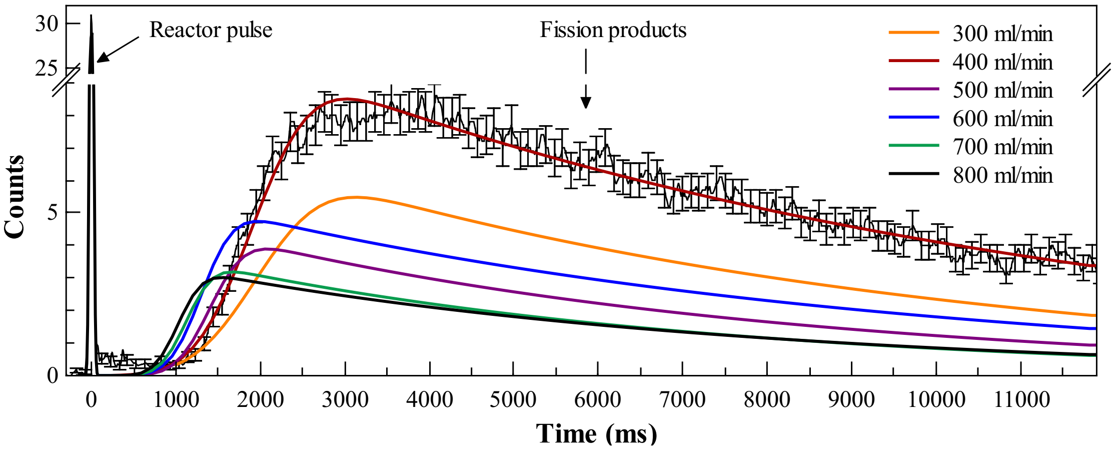

Figure 4.7: Recorded γ radiation during a reactor pulse at a gas flow rate in the range of 300 ml/min to 800 ml/min. Original data has mostly been omitted for clarity. The black line indicates a Gaussian fit for the reactor pulse and the coloured lines represent error function fits for the fission product signals in order to determine the transport time.

Table 4.5: Determined values for the transport times Δt and Δt_{50} at different gas flow rates with the corresponding pressure, measured inside the target chamber.

Q (ml/min)	$p_{TC,abs}$(mbar)	Δt (ms)	Δt_{50} (ms)
300	1000	2030(50)	7410(70)
400	1125	1950(50)	8340(70)
500	1300	1420(50)	6110(70)
600	1375	1320(50)	7000(70)
700	1600	1140(50)	5400(70)
800	1600	1040(50)	5630(70)

including the corresponding pressures measured inside of the target chamber and the extracted Δt_{50}, are given in table 4.5. The given uncertainty of Δt results from the uncertainty of the fit and the 30 ms systematic uncertainty from the width of the reactor pulse. The same was applied to Δt_{50}. Figure 4.8 shows the determined transport times in dependence on the gas flow rate. Both transport times roughly follow an inverse proportionality to the flow rates. At a flow rate of 800 ml/min, the investigated transport time Δt is 1040(50) ms, whereas it is a factor two larger at a rate of 300 ml/min. Usually the gas flow rate was set to 400 ml/min, since this offers the optimum performance of the gas-jet [Gru16]. The development of the Δt_{50} values show a similar behaviour but is less steep, thus the difference between 300 ml/min and 800 ml/min amounts to a factor of only 1.3.

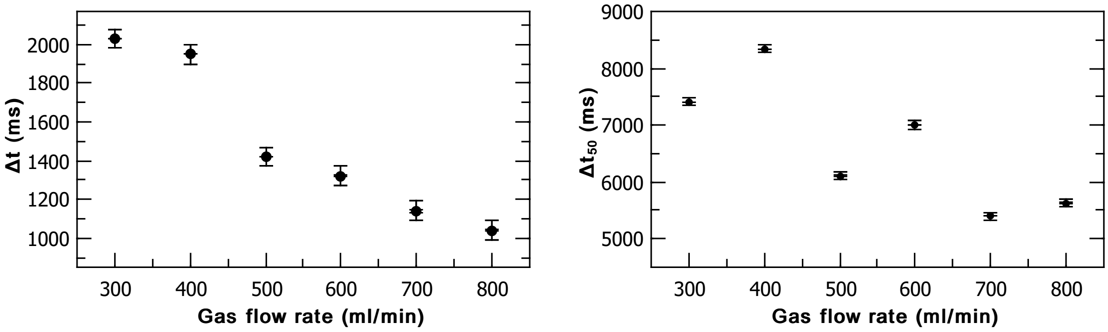

Figure 4.8: Left: Determined transport time Δt at different gas flow rates Q Right: Determined values for Δt_{50} in dependency on the gas flow rate. For more details, see text.

For future experiments at TRIGA-TRAP it is of interest to predict the decay losses of radio nuclides with short half-lives during the transport. Because the measured activity was produced by a large number of isotopes with different half-lives, the detected activity signal is not necessarily equal to the time distribution of the transported particles. However, assuming this equality, the decay losses can be calculated by a convolution of $A(t)$ with the radioactive decay for an isotope of interest. This was carried out for half-lives of 0.5 s to 10 s, as a representation of short-lived fission products. The resulting curves are shown in fig. 4.9, displaying the transported amount of a particle with the chosen half-life in comparison to $A(t)$. The ratio of the peak area of the convoluted curve to $A(t)$ yields the fraction of nuclides that are transported before they decay. The results of this evaluation are listed in table 4.6.

Table 4.6: Transported fraction yields ϵ for nuclides with half-lives in the range of 0.5 s to 10 s at different gas flow rates.

Q (ml/min)	$\epsilon_{0.5s}$ (%)	ϵ_{1s} (%)	ϵ_{2s} (%)	ϵ_{10s} (%)
300	0.9	5.0	36.7	61.0
400	0.5	3.1	10.2	50.0
500	1.9	8.7	45.4	68.1
600	1.4	6.5	36.9	60.3
700	2.4	9.1	43.8	66.3
800	2.6	9.3	43.4	65.7

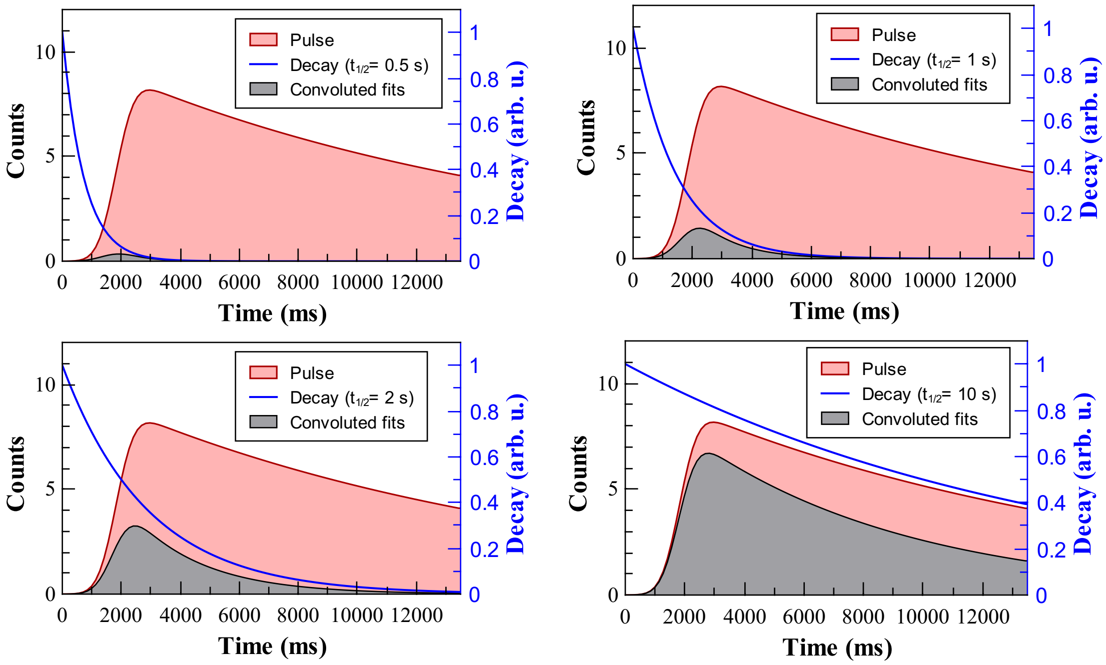

Figure 4.9: Transport efficiency curves for radio isotopes with different half-lives (0.5 s, 1 s, 2 s and 10 s). The red curve represent the evaluated fit curve for the fission product signal detected with a gas flow rate of 400 ml/min. Convolution with a decay curve (blue) yields the grey curve that represents the transported activity.

For a half-life of 10 s the transported fraction is larger than 50%, therefore the losses for longer half-lives can be neglected. This is reduced slightly for a half-life of 2 s, but for even shorter half-lives the transmission drops steeply. Higher gas flow rates can increase the yield for 0.5 s half-life nuclides by more than a factor of two, but have a negligible effect for long half-lives. Finally, the significantly lower transmission for a half-life of 2 s and a gas flow rate of 400 ml/min highlights the strong dependence on Δt_{50}, which for this gas flow rate was determined to be about 1 s longer than for other gas flow rates. Overall, these findings indicate that nuclides with 2 s half-lives can be easily extracted with the current gas-jet setup. For half-lives around 1 s, the gas flow rate can be increased to maximize yields, but it has to be considered that a change in the gas flow rate also affects the extraction efficiency of fission products out of the target chamber or the performance of the aerodynamic lens [Gru16].

4.2 Characterization of the surface ion source

As the surface ion source is a new installation, extended studies about its operation characteristics were carried out. Extended knowledge of its operation was acquired and an optimum heating procedure was investigated for reliable and stable operation. Furthermore, limitations in achievable temperatures were verified. During these studies smaller conceptual flaws of the ion source design have been identified and eliminated. During ion source operations its temperature has been recorded continuously with the pyrometer that is installed at a view port of the dipole magnet (see sec. 3.2). Its transmission factor has been set to $\tau = 100\,\%$ and the emissivity to $\varepsilon = 28\,\%$, which is quoted for tantalum in the pyrometers manual. The temperature readings could be confirmed with a wire pyrometer in the range of 1000 °C to 1600 °C.

4.2.1 Heating procedure

The surface ion source is a new installation and has not been used in this electrical configuration before, thus the development of a reliable heating procedure is necessary. Since there are strong interdependencies between several components or parameters, performance studies were made and the relevant aspects will be discussed.

For constant temperature operation it is crucial to prevent instabilities in the filament power and the bombardment power. Operating the electron bombardment power supply in current restricted mode leads to a self-energizing system. With increasing heating / filament power, the temperature and therefore the filament resistance increases. Due to the fixed set current, this then leads to a rising voltage and heating power and finally a further increase in temperature. This positive feedback is only restricted by the set voltage limitation, thus, once it is reached, the system experiences a current drop that temporarily decreases the temperature of the ionizer as well as the filament. At this point, the system heats up again in the same way, ending up in an oscillating state. These fluctuation usually occur around 2000 °C (see fig. 4.10) with amplitudes of several degree centigrades, increasing at higher temperatures. Thus a stable operation above this temperature is impeded.

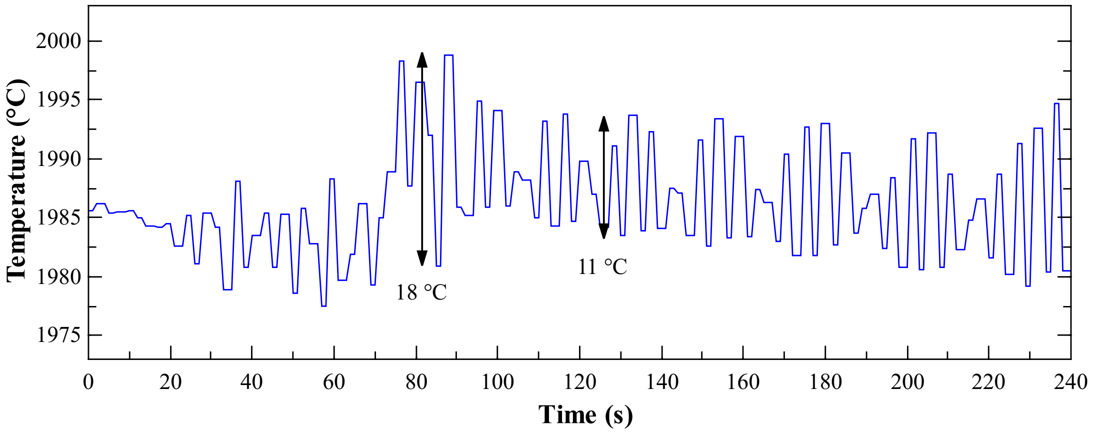

Figure 4.10: Temperature oscillations occurring during ion source heating with current limited operation of the electron bombardment power supplies. For details see text.

Besides this constraint, oscillations have to be avoided, because thermal stress generated by sudden temperature changes decreases the lifetime of the filaments and could lead to a complete fracture.

Conversely, operating the filament power supplies in a current restricted mode in combination with a voltage restriction on the electron bombardment power supplies proved to prevent temperature instabilities caused by unstable electron currents and simultaneously disables a continuous increase of power and temperature. The optimized heating procedure increases the ion source temperature from room temperature to 2000 °C within 45 minutes and is effective and time saving on the one hand, but also gentle and stable on the other hand. Detailed parameters of this heating routine are listed in table 4.7. A newly implemented ion source control software features the ramped increase of operation parameters, i.e., the current applied to the filaments U_{fil}, the electron bombardment voltage U_{EB} and the ramping speed

Table 4.7: Adjusted and observed parameters during the optimized ion source heating procedure. The two filaments are heated equally, thus their parameters are specified separately.

I_{IS} (°C)	I_{fil} (A)	v_{ramp} (A/min)	U_{EB}(V)	U_{EB} (mA)
0 – 770	0 – 20	2	300	0
770 – 1000	20 – 32	1	300	0 – 10
1000 – 1300	32 – 35	0.5	300	10 – 80
from 1300	35 – 38	0.3	300	80 – 530

v_{ramp}. It enables – to a certain extent – an automated heating procedure and simultaneously a smooth heating. It also allows a permanent recording of the mentioned parameters during ion source operation. Their trend throughout the heating process is shown in fig. 4.11. Both filaments are heated simultaneously and equally by increasing the applied current while the voltage remains unrestricted. The ramping rate starts with two ampere per minute, but has to be adapted later depending on the momentary temperature or rather the current applied to the filaments. The electron bombardment power supply creates a potential difference of around 300 V between filaments and ionizer. First commensurable electron bombardment occurs at around 1000 °C. Since it increases rapidly with raising filament current, the ramping speed has to be reduced. The generated temperature T_{IS} is proportional to the total power P_{total}:

$$T_{IS} \propto P_{total} = U_{fil1} \cdot I_{fil1} + U_{EB1} \cdot I_{EB1} + U_{fil2} \cdot I_{fil2} + U_{EB2} \cdot I_{EB2} \tag{4.6}$$

It consists of filament heating and electron bombardment, in which the latter makes the substantial contribution to this heating. The observed dependence of the ion source temperature on the heating power is shown in fig. 4.12. Whereas this dependence is almost linear up to a heating power of around 750 W or 1900 °C, a temperature gain above this value requires a tremendous increase in power. Thus the limit of maximum achievable temperature seems to be located around 2400 °C.

With the established operation parameters, stable temperatures could be kept for the complete daily operation cycles. Figure 4.13 shows the recorded temperature over a day of beamtime. After reaching the temperature of choice (2005 °C), it has been kept constant with minor fluctuations in the range of ± 4 °C during seven hours of operation. It has to be mentioned that the occurring changes are mainly caused by readjustment of certain parameters, e.g. the voltage applied to the filament, and are not caused by instabilities of the ion source itself.

The temperature of the ion source can be set to a chosen value within a few minutes as it is shown in fig. 4.14. This heating is precise and stable as long as the ion source is operated with appropriate patience. The occurring instability in temperature between 2200 °C and 2300 °C was caused by an operator mistake: the combination of an increased restriction of filament current and EB voltage caused a

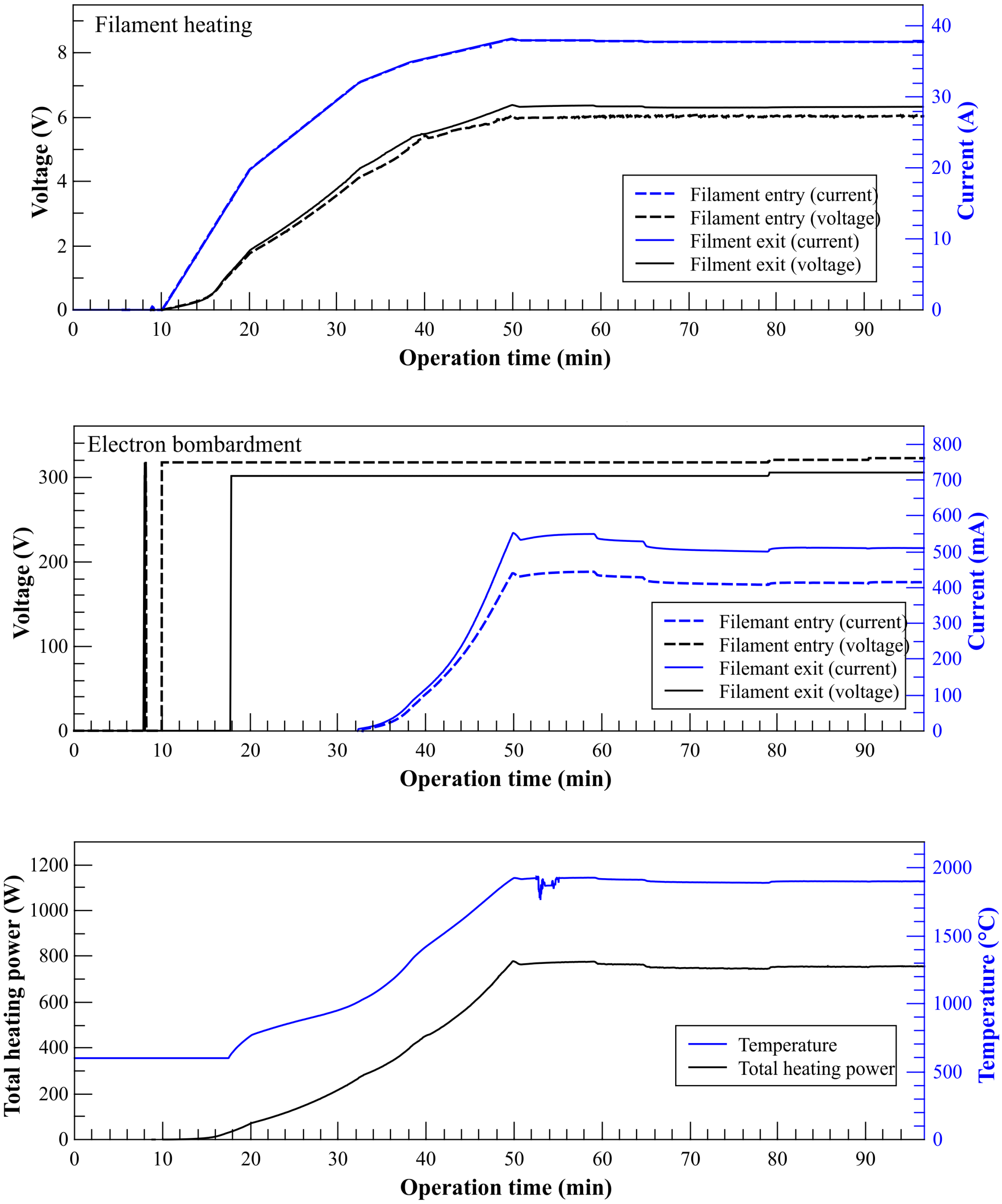

Figure 4.11: Simultaneous heating procedure of the entry and exit filament, split into filament heating (top) and electron bombardment (center). Whereas the filament heating is operated in current restricted mode, the electron bombardment power supply is restricted in its voltage. As the temporal evolution of the current restriction is identical for both filaments, both curves overlap completely (top). Bottom: Total heating power and the resulting temperature of the ion source. The lower detection limit of the pyrometer amounts to 599 °C, thus the temperature curve starts at this value. For details see text.

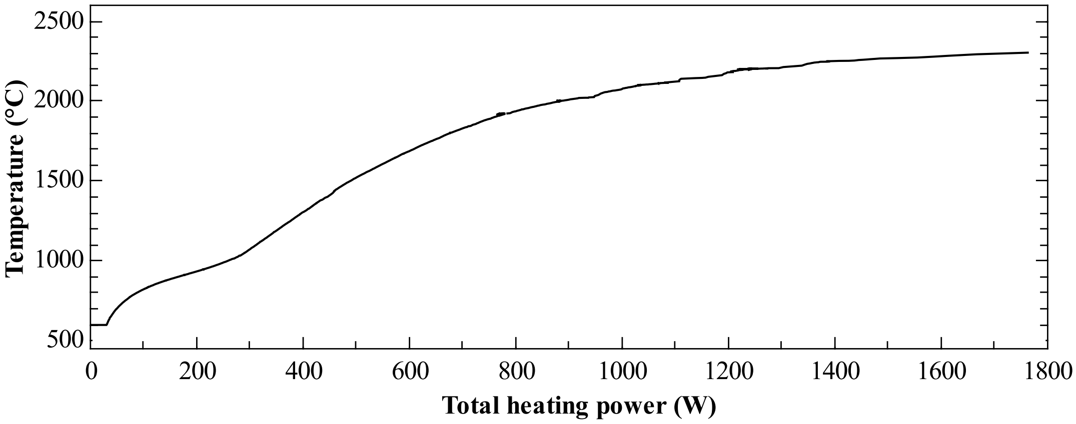

Figure 4.12: Dependence of the ion source temperature on the total heating power, consisting of filament heating and electron bombardment.

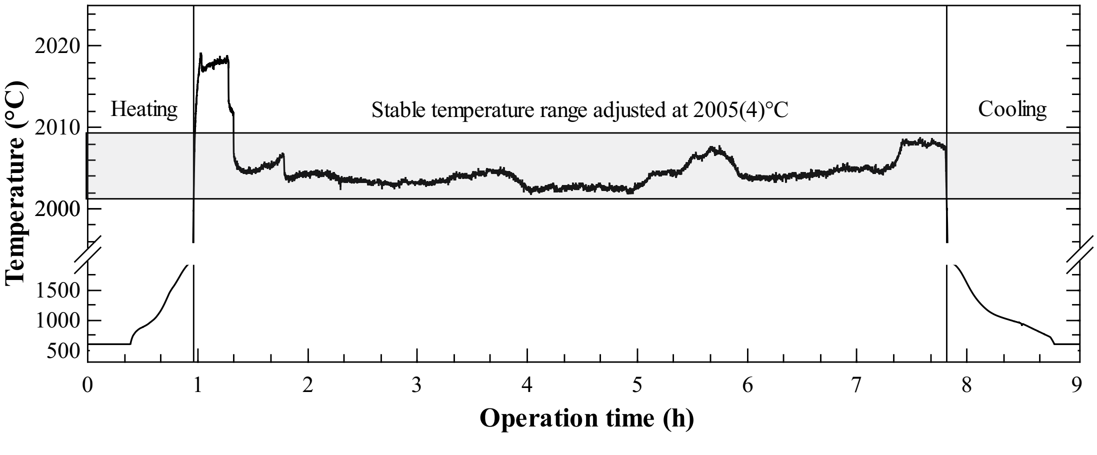

Figure 4.13: Chronological development of the temperature during a day of beamtime. After a short heating period and adjusting the temperature of choice, it remains constant until cooling down of the ion source was initiated.

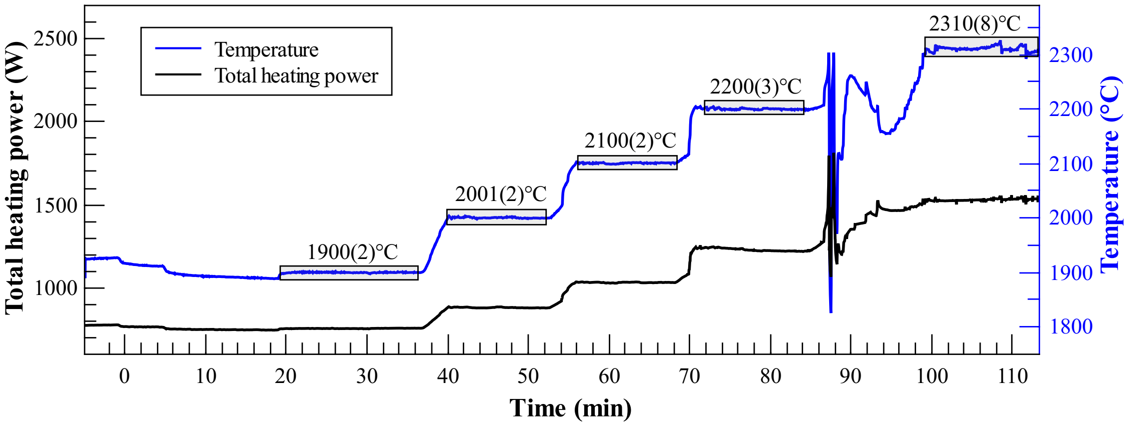

Figure 4.14: Temperature development during several hours of ion source operation. A controlled temperature raise can be induced by increasing the total heating power. The power and temperature fluctuation after 88 min were caused by operator mistake, see text. The chosen temperature ranges are depicted.

sudden rise of the EB current as well as its voltage up to their adjusted restrictions. The resulting negative feedback resulted in a drop of the EB current from 1550 mA to 800 mA at each filament. A readjustment of the mentioned parameters stabilized the system at the chosen temperature within less than ten minutes.

Nevertheless, the introduced procedure is only suitable if the vacuum system has been baked out before. By opening the experimental setup for maintenance of the whole ion source or in order to exchange one or both filaments, surface moisture as well as other pollutants contained within the replaced parts are introduced to the system. Therefore, the system has to be baked out to outgas volatile solvents or other involved contaminants. Especially during heating up the ion source to around 1000 °C for the first time after venting, the pressure inside of the ion source chamber increases drastically. A rapid heating procedure could therefore damage the turbo molecular pumps and has to be avoided. Another issue that has to be considered, is the deformation of the filaments during heating up for the first time. They are made of tungsten, which is relatively ductile in its unheated state. This circumstance allows to fix it within the correspondent holdings, whereby the filament experiences a certain tension. Thus, either a deformation of the shape itself or tilting of a complete filament can occur during heating. The latter results in an asymmetric gap between the filament and the ionizer, thereby generating a non-uniform abrasion of tantalum by the electron bombardment. In the worst case, the filament gets in contact with the ionizer, whereby a short circuit arises and the setup has to be reopened. By a comparably slow increase of the temperature, these two instances can be prevented. After first curing, contaminants are eliminated and simultaneously the tungsten recrystallizes and becomes less ductile [Klo66], thus the shape of the filament remains constant, even during rapid heating. However, at room temperature the recrystallized structure is highly brittle and has to be handled carefully to prevent fractures. By treating the filaments carefully, their lifetime can be extended to two or even more weeks, before they have to be exchanged.

4.2.2 Further ion source modifications

Since the ion source and the subsequent ion optics have been a new installation and their design has not been tested before, certain modifications of different parts had to be made after commissioning.

Heat shields

Fission products are ionized within the surface ion source, extracted through the heat shields and guided into the subsequent beamline. The shape of the produced ion beam can then be monitored on MCP detectors as introduced in sec. 3.8.1. After implementation of the ion source, a ring-shaped structure as depicted in fig. 4.15 appeared around the ion beam spot on the MCP detector behind the dipole magnet. The small spot in the center is the expected beam focus, which is small, accurately defined and circular. The ring leads to additional peaks appearing in recorded mass spectra, leading and tailing several peaks of identified stable nuclides, e.g., ^{88}Sr. It appeared already at a low heating power, long before an ion beam spot was observable. The analogous behaviour occurred during the cooling down process of the ion source. For identification of the cause, the ratio of the ring diameter to the central spot size has been determined. The same ratio of dimensions can be found between outer heat shield and ionizer orifice. It appears therefore evident that the observed MCP-signal is a result of the configuration of ionizer and heat shield, although the reason of its appearance could not be identified. To counteract the creation of this ring, a thin molybdenum disc with a smaller orifice (Ø=6 mm)

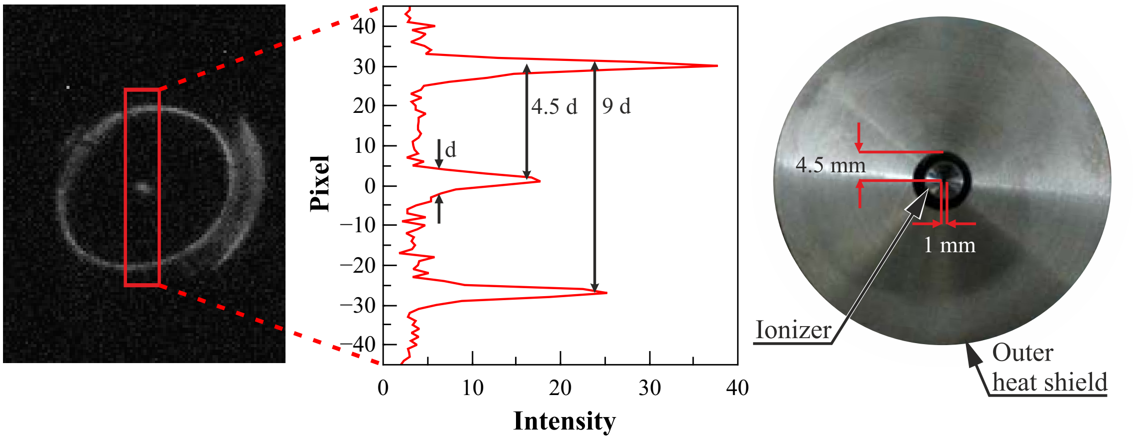

Figure 4.15: Recorded MCP-signal in front of the RFQ (left). The red rectangle marks the investigated area which yields the corresponding intensity profile (center). The photograph on the right is taken from the extraction side of the ion source, showing the same dimension ratios between the ionizer and the heatshield.

has been added between the two heat shields as indicated in fig. 4.16. It reduces the distance between ionizer and heat shield from 1.5 mm to 0.5 mm and thereby successfully prevented the creation of the ring.

Insulation

Another modification was essential concerning the insulators of the copper rods, which provide power to the filaments. To enable keeping a potential difference between these parts and the vacuum chamber or the ionizer, the filaments and their feedthroughs are electrically insulated against the remaining components. Each feedthrough has been surrounded by two identical insulators, whose plain surfaces touch each other at the half thickness of the base plate. Any imperfection of these surfaces or the presence of contaminations on the touching surfaces causes a narrow slit. The small distance between the copper feedthrough and the metallic base plate of 1.05 mm, combined with unevenness and a potential difference of ~ 300 V caused electrical discharges and sputtering that destroyed the insulator. These feedthroughs were not designed for large potential differences, as the ion source at JAEA/Tokai is operated in a different connection concept. Therefore, the feedthroughs were adapted to withstand much higher voltages. A comparison of the two feedthroughs is shown in fig. 4.16.

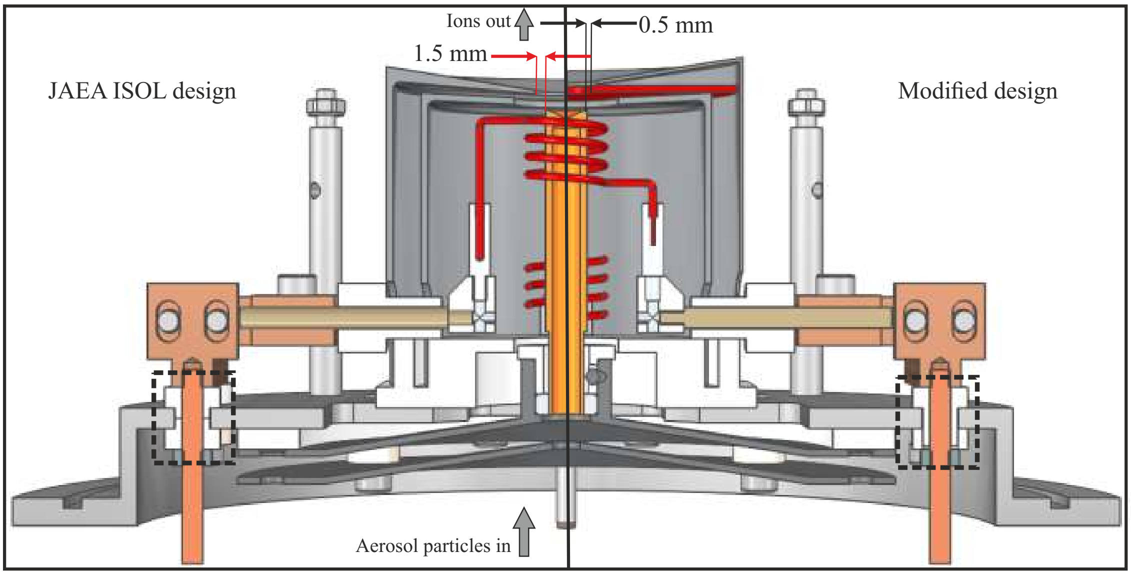

Figure 4.16: Direct comparison between the original JAEA ISOL design (left) and the modified design used at TRIGA-TRAP (right). The dashed areas denote the redesigned insulators. The added heat shield inlay is illustrated in red.

4.2.3 Ionization efficiency studies

Knowledge about the ion source performance is of major interest to estimate the range of accessible elements. An option for verification of the ionization behaviour is the determination of the ionization efficiency of various elements at different temperatures. Since the ionization ability of a surface ion source is limited to elements with comparably low ionization potentials, rubidium ($\mathrm{IP} = 4.177\,\mathrm{eV}$) and strontium ($\mathrm{IP} = 5.696\,\mathrm{eV}$) are appropriate candidates for ionization efficiency investigations. Such investigations are affected by precursor effects as mentioned in sec. 4.1.1, thus these investigation cannot be performed for most strontium isotopes directly with their measured peak areas. Rubidium is exempted from these precursor effects as the corresponding parent element, krypton, is neither ionized by the surface ion source nor adsorbing to the aerosol particles due to its volatile nature. Based on this, the following decay chains are relevant for the evaluation, with bold isotopes being detected in the γ spectra:

$$^{90}\text{Rb} \xrightarrow{4.3\,\text{m (m) / }2.6\,\text{m}} {}^{90}\text{Sr} \xrightarrow{28\,900\,\text{a}} {}^{90}\text{Y}\ldots \tag{4.7}$$

$$^{91}\text{Rb} \xrightarrow{58\text{ s}} {}^{91}\text{Sr} \xrightarrow{9.5\text{ h}} {}^{91}\text{Y}\ldots \tag{4.8}$$

$$^{92}\text{Rb} \xrightarrow{4.5\text{ s}} \mathbf{{}^{92}Sr} \xrightarrow{2.71\text{ h}} {}^{92}\text{Y}\ldots \tag{4.9}$$

$$^{93}\text{Rb} \xrightarrow{5.84\text{ s}} \mathbf{{}^{93}Sr} \xrightarrow{7.43\text{ m}} {}^{93}\text{Y}\ldots \tag{4.10}$$

$$^{94}\text{Rb} \xrightarrow{2.7\text{ s}} {}^{94}\text{Sr} \xrightarrow{74\text{ s}} \mathbf{{}^{94}Y} \xrightarrow{18.7\text{ m}} {}^{94}\text{Zr (stable)} \tag{4.11}$$

$$^{95}\text{Rb} \xrightarrow{378\text{ ms}} {}^{95}\text{Sr} \xrightarrow{23.9\,\text{s}} {}^{95}\text{Y}\ldots \tag{4.12}$$

The ideal decay chain to determine the strontium ionization efficiency is the one with the weakest precursor effects. This situation occurs if the Rb member has a very short half-life, such that it decays to Sr before entering the ion source, or when the independent fission yield of the Rb precursor is negligible compared to that of the Sr isotope. Independent fission yields of rubidium and strontium isotopes inside the target are shown in fig. 4.1. They are in the same order of magnitude, whereas those of rubidium are significantly higher compared to those of strontium up to a mass of 94 u. It would be interesting to investigate ^{95}Sr, since the precursor effect of rubidium is significantly lower compared to other masses. Furthermore, it would offer the advantage that ^{95}Rb decays with a half-life of 377 ms. As the transport time to the ion source is longer than 1950 ms (see sec. 4.1.5) at a gas flow rate of 400 ml/min ^{95}Rb decays almost entirely to ^{95}Sr before entering the ion source. Thus only the daughter is ionized, thereby yielding the undisturbed ionization efficiency of strontium. Unfortunately, the short half-life of 24.4 s makes detection difficult: with an expected ionization efficiency of 2 %, a measurement time pattern of 5/1/5 min (see table 4.1), the γ line at 686 keV with an intensity of 22.6 % and a detection efficiency of 0.9 % at this energy, around 20 counts are expected within a spectrum. With the usual background level, this is not enough for unambiguous detection. It should be possible to detect its daughter nuclide ^{95}Y, but even from a mass separated beam no significant signal above background was found with this measurement pattern. Thus, the nuclides ^{89}Rb, ^{92}Sr, ^{93}Sr and ^{94}Y were investigated and the corresponding results are discussed below.

Two different approaches are conceivable to gain information on the ionization efficiency of strontium: a comparison of individual element quantities before and after ionization directly yields efficiencies, whereby the examination of the ratio between two different species yields relative values for the ionization efficiency of the two species. The first method theoretically allows obtaining absolute efficiencies comparably easy by comparison of two gamma spectra. However, in practice the experimental conditions prohibited application of this method: A “pre IS” or “pre lens” collection would have to be compared to a “post IS” collection, taken ideally at the same time or at least in quick succession, to reduce systematic errors. As there is no advanced beam diagnostic station in front of the ion source, the setup has to be opened and vented in order to remove the glass fiber filter, requiring about 30 minutes. This limits the range of accessible nuclides to those with correspondingly long half-lives. Subsequently the ion source has to be heated to a given temperature, which takes further 45 minutes (see sec. 4.2.1). This reduces the comparability of the acquired spectra significantly due to possible gas-jet fluctuations. Moreover, a collection at these stages contains numerous isotopes producing an increased background within the γ spectra as indicated in fig. 4.17. This is particularly critical during efficiency studies at different temperatures. Smaller signals of less abundant isotopes or less intensive γ lines may be overshadowed. Furthermore, venting the beamline requires a comparably cold ion source as tungsten oxidizes at temperatures of ≥ 400°C and tantalum at ≥ 300 °C. The amount of collections is thereby limited to at most two per day, offering poor statistics. Studies at different temperatures are therefore not possible since a beam time is usually too short. Due to these facts, this method is not suitable to determine ionization efficiencies at TRIGA-TRAP.

Another approach compares the ratio of two individual species and is thereby almost independent of gas-jet fluctuations, the main source of systematic deviations. Thus, the evolution of the ionization efficiency can be observed by collecting several γ spectra at either beam diagnostic station “post IS” or “pre RFQ”, with only one reference spectrum in front of the ion source being necessary. An attempt to determine an ionization efficiency was made by ion collections behind the ion optics subsequent to the ion source at beam diagnostic station “post IS”. The major advantage of this location is that the resulting γ spectra yield information about the complete range of ion species. This offers the possibility to compare the yield of several isotopes at the same time and allows eliminating gas-jet fluctuations by normalization to

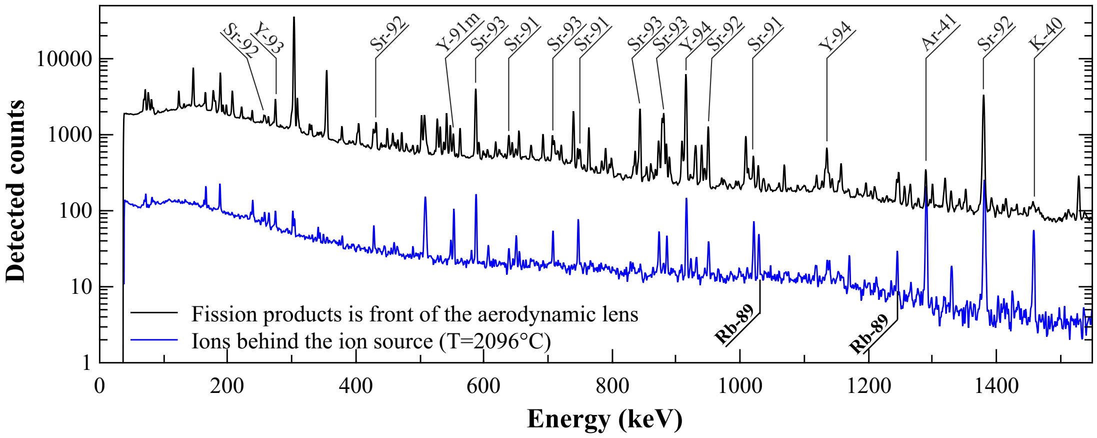

Figure 4.17: γ spectrum of a "pre lens" collection (black) and a "post IS" collection (blue), respectively. The cycle for both measurements has been set to 10 min collection, 30 min decay and 30 min recording time.

a chosen isotope. Figure 4.18 summarizes the results of this measurement study, comprising "post IS" collections taken in a temperature range between 1770 °C and 2330 °C, performed with a measurement cycle of 10 min collection, 30 min decay and 30 min recording time. Although more than one γ line for ^{89}Rb, ^{92}Sr, ^{93}Sr and ^{94}Y each has been analyzed, only one evaluated γ line per isotope is shown for clarity. The aforementioned isotope ratio to eliminate the influence of gas-jet fluctuations on the ion count rate is taken by normalizing to the count rate of ^{89}Rb. Linear functions are fitted to the data to determine the trend from the widely scattered data points. The data sets of both strontium isotopes do not yield a significant increase in the count ratios. Thus it is rather difficult to determine a distinct value for the ionization efficiency.

Assuming that the transport efficiency of the aerosol-based gas-jet is independent from the chemical element, the ratio of particle numbers occurring inside the ion source before ionization, represented by $(\mathrm{Sr}/\mathrm{Rb})_{in}$, should be equal to that of their production rates. This additionally presumes, that neither strontium nor rubidium decays during the transport time. It also neglects the presence and the decay of krypton isotopes, which are precursors of rubidium. This negligence is reasonable as Kr is not transported within the aerosol-based gas-jet due to its volatile nature.

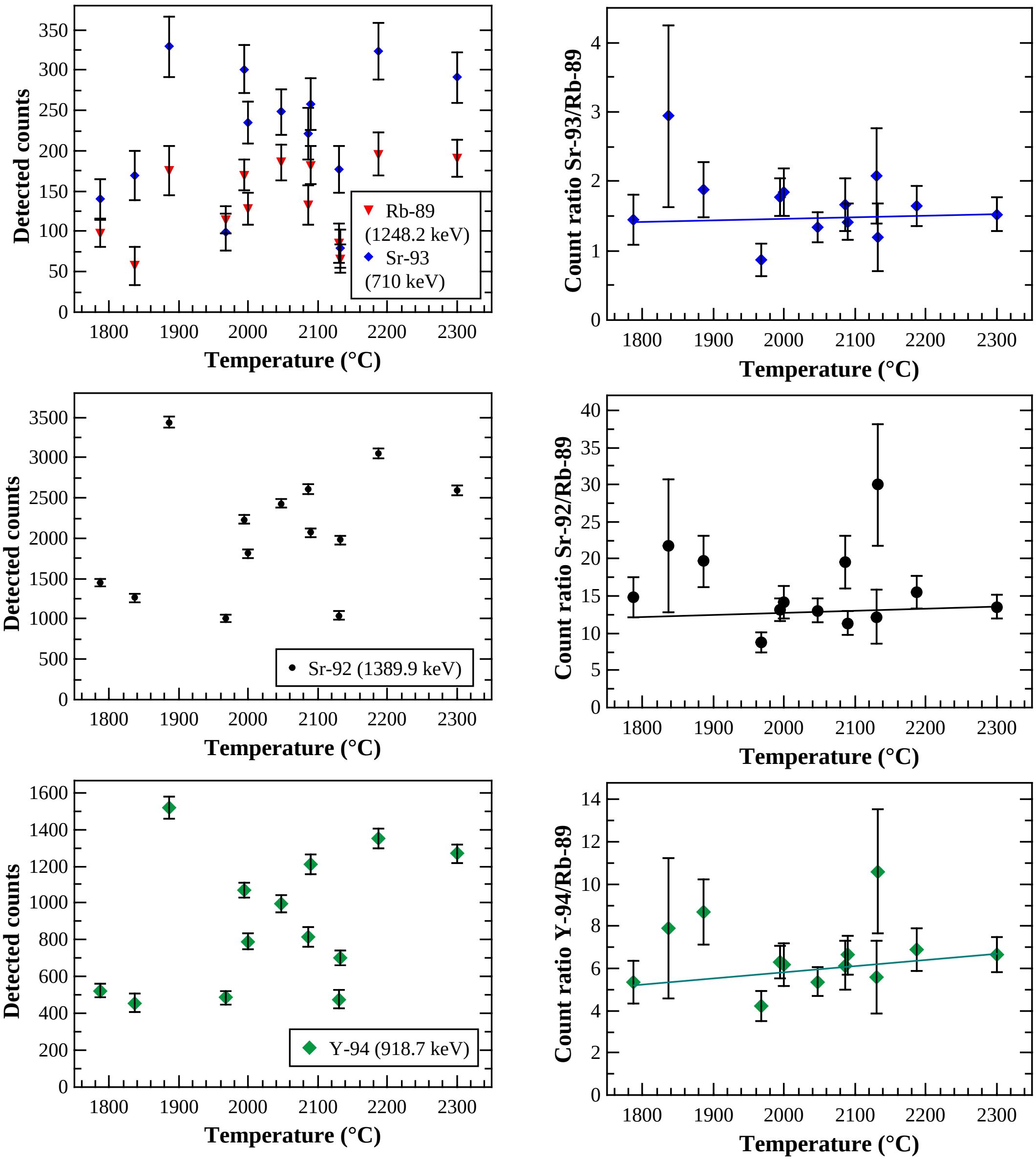

Figure 4.18: Extracted data for ^{89}Rb, ^{92}Sr, ^{93}Sr and ^{94}Y from “post IS” fission product collections, performed in a temperature range of 1770 °C to 2330 °C. Left column: Peak area of selected γ-ray signals. Right column: Detected counts of ^{92}Sr, ^{93}Sr and ^{94}Y normalized to that of ^{89}Rb. A linear fit underlines the dependence of the counts on the temperature. For details, see text.

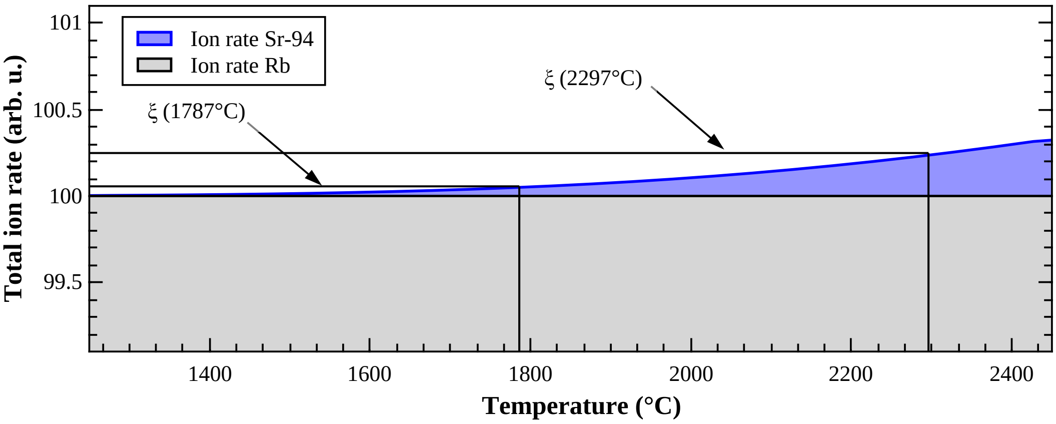

Figure 4.19: Theoretically expected ion rates of ^{94}Sr and its rubidium precursor in dependency on the temperature, calculated by eq. 2.10 with N=50. ξ denotes the cumulative ion rate of Rb and Sr at 1787 °C and 2297 °C, respectively.

However, after ionization the particle ratio decreases to $(\mathrm{Sr/Rb})_{out}$:

$$\left(\frac{\mathrm{Sr}}{\mathrm{Rb}}\right)_{in} \gg \left(\frac{\mathrm{Sr}}{\mathrm{Rb}}\right)_{out} = \frac{I_{\mathit{eff}}(\mathrm{Sr})}{I_{\mathit{eff}}(\mathrm{Rb})} \cdot \left(\frac{\mathrm{Sr}}{\mathrm{Rb}}\right)_{in} \quad \text{with} \quad I_{\mathit{eff}}(\mathrm{Rb}) \gg I_{\mathit{eff}}(\mathrm{Sr}) \qquad (4.13)$$

The ionization efficiency of rubidium is assumed to be 100 % while the expected ionization efficiency of strontium should rise by only 0.5 % to 1 % per 100 °C (see sec. 2.2). Thus the height of recorded γ-ray signals should be rather low, even at a temperature of 2330 °C. The rubidium precursor isotopes decay entirely into strontium during a fission product collection and contribute to the subsequently recorded γ-ray peaks of strontium as indicated in fig. 4.19. It therefore can be considered that this contribution is independent from the temperature and generates a constant offset. The increase in detected signal or the ratio $(\mathrm{Sr/Rb})_{out}$ is therefore solely produced by the gain in ionization of strontium. The theoretically expected cumulative ion rates ξ can be used for estimations of the experimental performance. It has to be mentioned that in the case of the decay chain of isotopes with the mass number 94, the strontium isotope is short-lived as well and thus cannot be observed within the γ spectrum. Hence the signal of ^{94}Y is investigated. It is assumed, that this signal is solely produced by former rubidium and strontium, as the theoretical ionization efficiency of yttrium amounts to values around 0.1 %, 20 times less than strontium.

As depicted in fig. 4.18, a linear function is fitted to the experimental values,

Table 4.8: Ion rate ratio of $\xi(2297\,^\circ\mathrm{C})$ to $\xi(1787\,^\circ\mathrm{C})$, based on theoretical calculations and extracted from experimental results, respectively.

	$\xi_{2297\,^\circ\mathrm{C}}/\xi_{1787\,^\circ\mathrm{C}}$	
Mass (u)	Theory	Experiment
92	102 %	108(27) %
93	105 %	112(30) %
94	118 %	129(24) %

providing experimental values for ξ. The modified Saha-Langmuir equation (eq. 2.10) has too many free parameters to get appropriate results with the little amount of experimental data, thus it was not fitted directly to the data. Due to the broad scattering of the data points it is not possible to extract significant ratios for every temperature, but it can be calculated by comparison of ξ at limit temperatures. Results of this analysis are listed in table 4.8 and compared to expected values. The latter are calculated by eq. 2.10 with $\mathrm{N} = 50$, which seems to be an appropriate approximation for the number of effective atom-wall interactions as reported by Sato et al. [Sat15a]. The resulting ratios agree within the given accuracy, corresponding to an ionization efficiency for strontium of 1.5 % at 1787 °C and 7.0 % at 2297 °C, respectively. Thus, no discrepancy to the ionization behaviour from this model is expected.

4.3 Ion beam characterization

With regard to subsequent mass measurements, it is important to gain information about available ion species that can be guided to a subsequent Penning trap. The beam produced within the surface ion source contains isotopes with different masses from different elements. The installed dipole magnet can separate them by their m/q ratio (see sec. 3.4), but it has to be calibrated to verify the relationship between the magnet current and the separated ion mass. Additionally, analysis and optimization of the ion beam, i.e., its shape, is of major interest for an improved transport of ions to the trap.

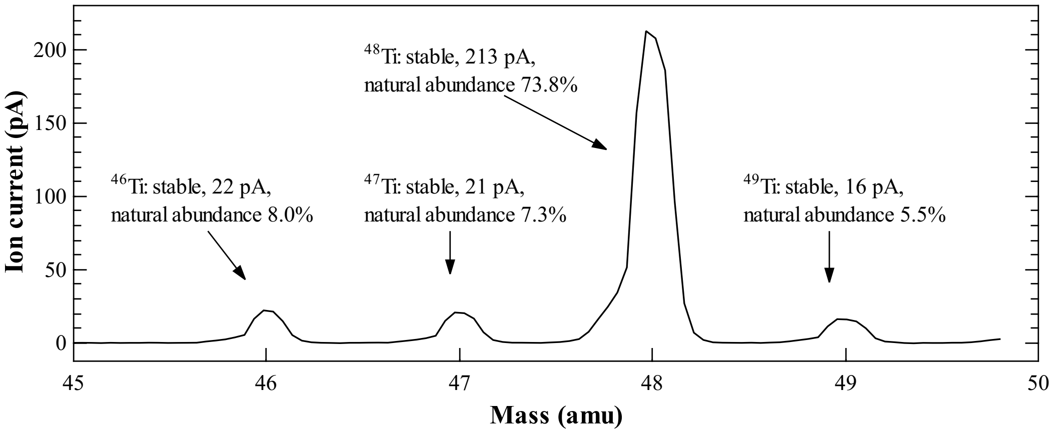

Figure 4.20: Mass spectra recorded on the Faraday "pre RFQ" behind the mass separator. The surface ion source has been loaded with Ti foil for a first calibration of the dipole magnet.

Calibration of the mass separator

For a mass calibration of the dipole magnet it is useful to scan a certain range of masses, detect their current by a Faraday cup and subsequently identify characteristic peak patterns, assuming to observe only singly charged ions. Due to limited time during a measurement campaign, a calibration should be made before beamtime, thus without using the gas-jet. Since the amount of observable species is smaller under these conditions, milligram amounts of a metal foil can be inserted into the ion source to produce ions of corresponding species. The produced isotopes and their masses are well known, thus they are easy to identify. A suitable metal is titanium, since its ionization potential of 6.8 eV and melting point of 1668 °C are not too high, so that a feasible evaporation rate and ion current can be reached at ion source temperatures of 1400 °C and beyond. Furthermore natural titanium consists of five stable isotopes with appropriate abundances that generate a characteristic peak pattern (see table 4.9). A typical mass spectrum of a Ti sample, recorded in front of the RFQ at an ion source temperature of 1500 °C, is shown in fig. 4.20. The adjusted temperature is low enough to enable investigations over several hours. The recorded spectrum shows titanium isotopes in the mass region of 46 u to 49 u. As the scan has been stopped quite early ^{50}Ti is not detected. The ratios of the peak height of ^{49}Ti to the other peak heights are listed in table 4.9 and compared with expected ratios. The observed peak ratios are in agreement with the natural isotope

Table 4.9: Isotope abundances of natural titanium as well as their ratio to ^{49}Ti and peak hight ratios extracted from the recorded mass spectrum.

Isotope	Nat. abundance (%)	Ratio (th.)	Ratio (meas.)
^{46}Ti	8.0	1.4	1.5
^{47}Ti	7.3	1.3	1.3
^{48}Ti	73.8	13	13
^{49}Ti	5.5	1	1
^{50}Ti	5.4	0.98	-

abundances and confirm the determination.

The inserted Ti-foil has to be removed before the start of an online measurement campaign, thus Ti-isotopes are not longer observable. Usually the two most abundant stable isotopes of potassium (^{39}K: 93.26% / ^{41}K: 6.73%) are distinctly identifiable as their presence within the setup, i.e., the gas-jet is comparatively high. Thus they can be used for a check of the calibration and for first verifications of the experimental system. In general, the calibration can be extrapolated to higher masses by following eq. 3.1. However, in the case of a misaligned ion beam, the actual deflection angle ϕ or radius ρ might be different, thus a calibration based on more anchor points should be performed. For subsequent mass measurements of short-lived fission products, masses in the region of 80 u to 100 u are of major interest, thus this region is investigated more precisely. Figure 4.21 shows a detailed scan of these masses. Overall the spectrum is quite empty with a background of several tens to hundreds of fA. As mentioned in sec. 4.1.4 the rate of radioactive ions in front of the RFQ amounts to 10^3 - 10^4 ions per second, corresponding to a current of 0.17 fA to 1.7 fA, depending on the considered isotope. Thus fission products are not observable within this spectrum and signals are solely produced by stable ions. The labeled peaks belong to the natural isotopes of strontium. Their individual signal heights correspond to the natural abundance of each isotope and are consistent amongst each other (see table 4.10). This proves that the mass calibration of the dipole magnet has been done correctly. Besides the distinctly identified strontium peaks, two more signals are detected between the masses 90 and 91 with a current of 51 pA and on mass 93 with 18 pA. An unambiguous identification is not possible, because they do not match singly charges, and monoatomic ions of natural occurring elements. It is also unknown, if these species are singly or doubly charged, thus

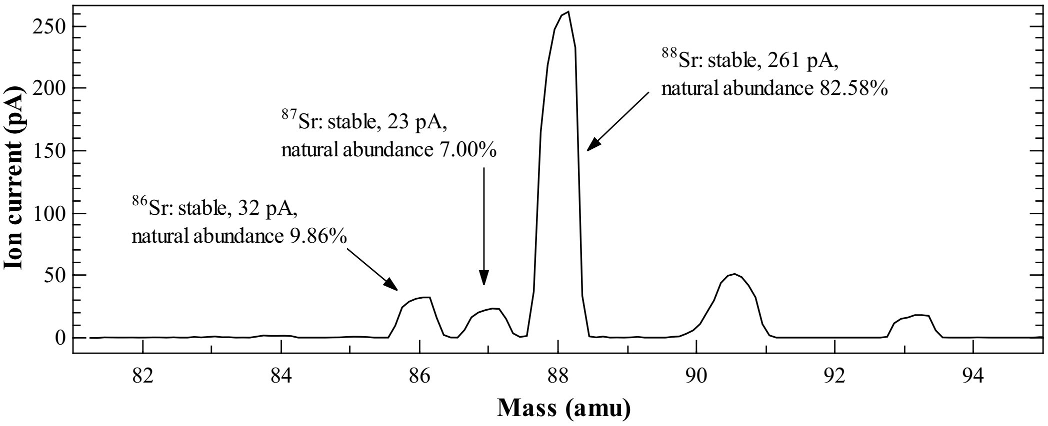

Figure 4.21: Mass spectra in the region of 82-94 amu detected by the Faraday cup behind the mass separator during reactor operation, using the CdI_2 loaded gas-jet.

their mass cannot be determined unambiguosly. The signal appearing at 90.5 u implies at least a doubly charged ion, making $^{181}Ta^{2+}$ a possible candidate, which could have been created by the electron bombardment on the ionizer. The signal appearing at 93 u could be created by $^{186}W^{2+}$ evaporating from the filaments.

Table 4.10: Isotope abundances of natural strontium as well as their ratio relative to ^{87}Sr and peak hight ratios extracted from the recorded mass spectrum.

Isotope	Nat. abundance (%)	Ratio (th.)	Ratio (meas.)
^{86}Sr	9.86	1.4	1.4
^{87}Sr	7.00	1	1
^{88}Sr	82.58	11.8	11.3

Beam shape

The MCP/phosphor screen-combinations installed at several positions of the TRIGA-TRAP beamline offer the chance to verify the optics tuning and the shape of the generated ion beam. As this detector type is extremely sensitive to larger currents, it is not suitable to use before mass separation but highly convenient for detection afterwards. Thus the separated masses can be visualized by the detectors as shown in fig. 4.22. The exposure time of the camera as well as gas-jet parameters remained unchanged during the detection of both signals. The left picture shows the masses 87 u and 88 u, where the stable isotopes ^{87}Sr and ^{88}Sr were identified in the mass

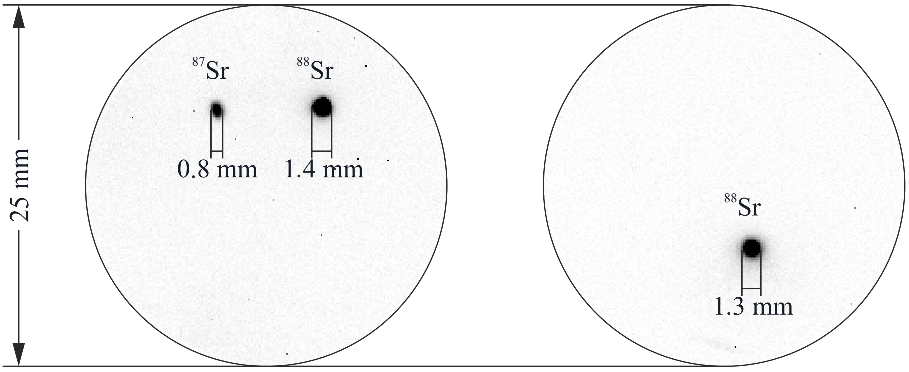

Figure 4.22: Camera images of the MCP phosphor screens in front of the RFQ (left) and behind it (right) after ion cooling and bunching. The observed spot of ^{88}Sr appears larger due to over exposure of the phosphor screen from the larger ion current. The colours are inverted for a better visualization.

calibration. To picture two separated masses, the adjustable slit blades installed behind the magnet were completely opened. For operation of the RFQ they are typically closed to create a slit with a width of 1.5 mm. This ensures that only one m/q species can enter the inner volume of the RFQ and neighboring ones are cut off. The picture on the right shows mass 88 u, detected behind the RFQ operated in bunched mode. At the given conditions optimum buffer gas cooling has been achieved at a helium gas flow rate of 0.11 mbar·l/s. The beam spots shown in fig. 4.22 appear with different intensities because the positions of the MCP's are not aligned axially to the beam. The geometrical shapes of the observed spots are circular. This implies a uniform and highly focused ion beam, offering optimum conditions for transmitting the ions to subsequent components. Knowing that the active area of the MCP has a diameter of $\O = 25\,\text{mm}$, the beam diameter can be determined to 0.8 mm to 1.4 mm depending on the ion species. Naturally isotopes with a higher abundance generate larger beam spots with an enlarged visibility.

4.4 Mass measurements of fission products

The last step in the commissioning process was to transfer the ions into the Penning traps and perform the first mass measurements of short-lived nuclides at TRIGA-TRAP. The prepared ions are transferred to the purification trap with a kinetic

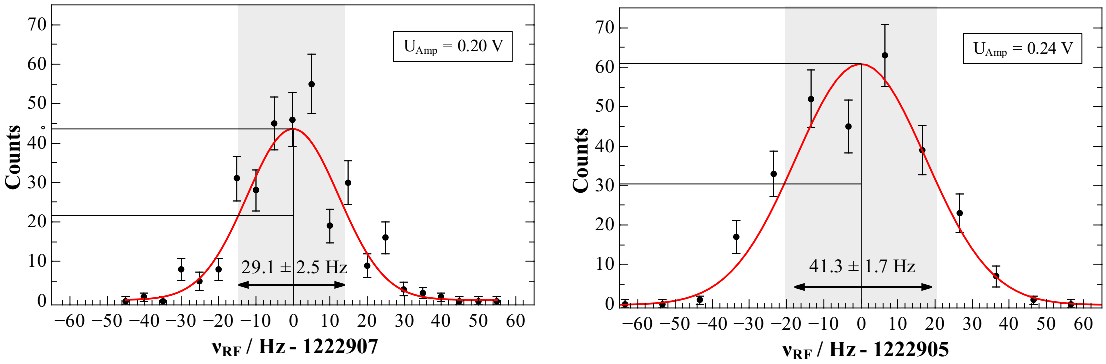

Figure 4.23: Recorded cooling resonances of $^{88}\mathrm{Sr}^{+}$ within the purification trap. The FWHM is indicated in both spectra. Left: Conversion amplitude of 0.20 V. Right: Conversion amplitude of 0.24 V. For details, see text.

energy of only 1.1 keV. Due to the low transmission through the PDT, an ion rate of only 40 stable ions per minute or around 0.3 ions per minute in the case of radio nuclides is observed within the purification trap. Still, this should be sufficient for a subsequent mass measurement. A moderate resolution measurement of ν_c can already be performed in the purification trap by resonant buffer gas cooling (see sec. 2.3.1). This method not only allows selective centering of ion species but also a measurement of ν_c, as introduced in sec. 2.3.1. Due to broadening effects of the buffer gas, the achievable relative precision is limited to around 10^{-6}. Unfortunately, the precision trap was not available during the measurement campaigns, thus it was not possible to achieve a higher precision. The first ion species that has been investigated within the purification trap was $^{88}\mathrm{Sr}^{+}$, the most abundant isotope of natural Sr, which is ionized by the surface ion source. As such it offers the strongest ion beam in the mass region of interest to tune the trap parameters quickly. During the optimization procedure, various values for the conversion amplitude in the range of 100 mV to 400 mV have been tested. For the extraction of ν_c, the target is to obtain a narrow resonance without a loss in peak or ion count rate. Figure 4.23 shows two cooling resonances recorded with the best setting in these regards with a conversion amplitude of 0.24 V and 0.20 V. Smaller amplitudes lead to wider resonances, i.e., worse centering, whereas with higher amplitudes the count rate was too low to record a proper resonance. It was chosen to use a cooling amplitude of 0.24 V, although it results in a broader peak compared to those observed at 0.20 V, but it results in a

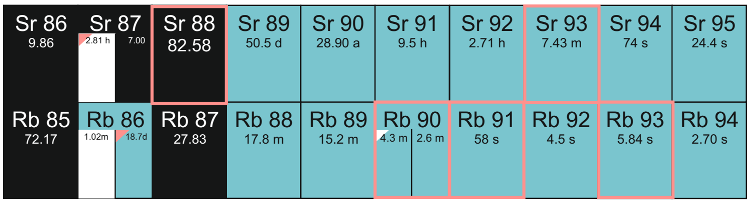

Nuclide	Γ (#/s)
$^{90/90\mathrm{m}}\mathrm{Rb}^+$	$2.1{\cdot}10^6\,/\,4.1{\cdot}10^5$
$^{91}\mathrm{Rb}^+$	$6.6{\cdot}10^6$
$^{93}\mathrm{Rb}^+$	$9.1{\cdot}10^6$
$^{93}\mathrm{Sr}^+$	$7.6{\cdot}10^6$

Figure 4.24: Left: Excerpt of the Karlsruhe nuclide chart, showing the investigated species and their half-lives, respectively the natural abundance of stable nuclides. Right: Fission yield of the determined species, produced within the used ^{235}U-target.

higher ion rate (see table 4.11). After successful and reproducible measurement of this stable nuclide, radioactive species were investigated.

The short-lived neutron-rich fission products $^{90/90\mathrm{m}}\mathrm{Rb}^+$, $^{91}\mathrm{Rb}^+$,$^{93}\mathrm{Rb}^+$ and $^{93}\mathrm{Sr}^+$ have been trapped and identified within the purification trap. The most exotic trapped nuclide was ^{93}Rb with a half life of 5.84 s. These ion species have been chosen since their production rates within the ^{235}U-target are amongst the highest (see fig. 4.24) and the ionization potentials are comparably low resulting in maximum yield. However, due to the low transmission from the RFQ to the purification trap, rates of only 0.3 to 0.9 ions per minute had been observed, thus the measurements typically took up to 140 min to detect an appropriate number of ions. Figure 4.25 shows the measured cooling resonance of $^{90/90\mathrm{m}}\mathrm{Rb}^+$ ($t_{1/2} = 4.3\,\mathrm{min}(^{90\mathrm{m}}\mathrm{Rb})$; 2.6 min (^{90}Rb)) and $^{91}\mathrm{Rb}^+$ ($t_{1/2} = 58\,\mathrm{s}$). The FWHM of the cooling resonances are narrow enough to unambiguously identify the ion species via the determined cyclotron frequency ratios.

Figure 4.26 shows a single cooling resonance of $^{93}\mathrm{Rb}^+$, the most exotic fission product measured within this work, and a combined one of both $^{93}\mathrm{Rb}^+$ and – conjecturally – $^{93}\mathrm{Sr}^+$. During the latter measurement, the scanned frequency range was extended in order to capture the two different ions. Although this resulted in a rather long measurement to get appropriate count rate for both nuclides, the given

Table 4.11: Properties of recorded $^{88}\mathrm{Sr}^+$ resonances and their determined cyclotron frequencies.

U_{Amp} (V)	t_{rec} (s)	# Ions	Rate (#/s)	ν_c (Hz)	FWHM (Hz)
0.24	273	281	1.03	1 222 904.92 (1.03)	41.3 (1.7)
0.20	745	503	0.67	1 222 906.72 (0.57)	29.8 (0.8)
0.20	410	307	0.75	1 222 906.72 (0.57)	29.1 (2.5)

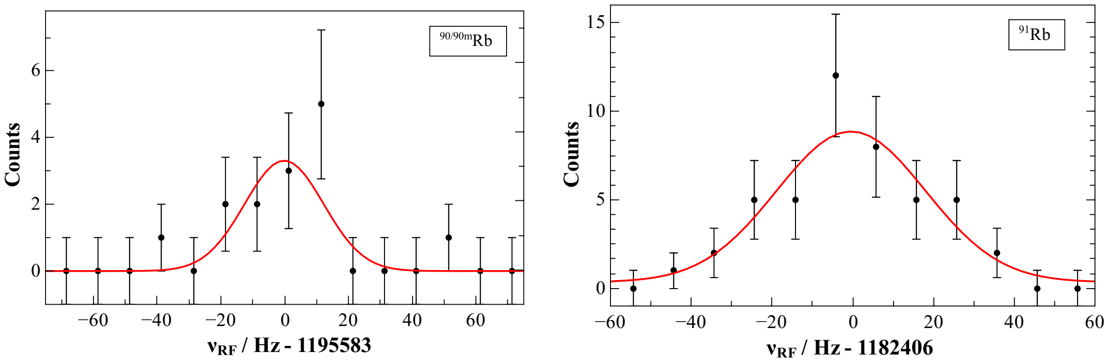

Figure 4.25: Recorded cooling resonance of $^{90/90\text{m}}$Rb$^+$ (left) and ^{91}Rb$^+$ (right). The red lines indicate a Gaussian fit curve for determination of the center frequency. For more details, see text.

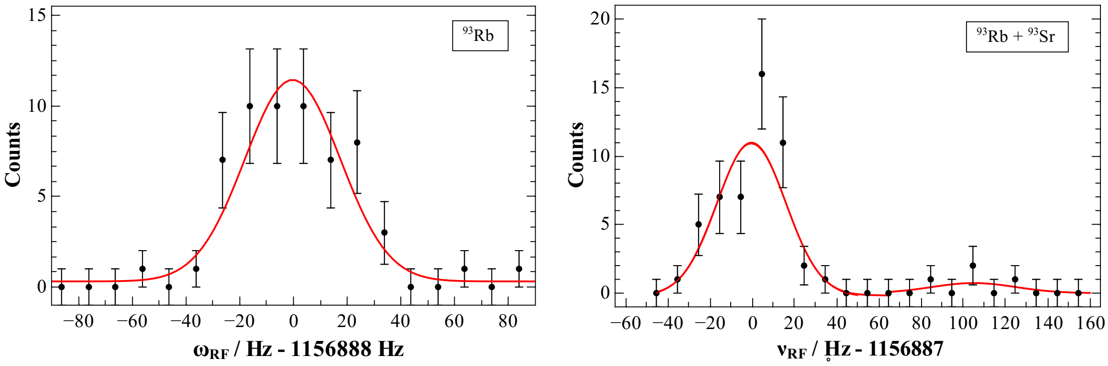

Figure 4.26: Recorded cooling resonance of ^{93}Rb. Right: Simultaneous measurement of ^{93}Rb$^+$ and ^{93}Sr$^+$. For more details, see text.

time frame was too short to achieve a more significant signal of ^{93}Sr$^+$. Details about all measurements of short-lived nuclides, e.g., the full width at half maximum and the determined center frequency, are listed in table 4.12. The determined FWHM-values of the respective resonances prove the selective centering of ions with a mass selectivity of $m/\delta m = 5 \cdot 10^{-5}$. To extract the atomic mass of an unknown trapped ion from a measured cooling resonance and thereby identifying the ion species, the cyclotron frequency has to be determined first. In the case of a cooling resonance, it coincides with the center frequency and can be determined by the maximum of a Gaussian function, fitted to the detected data. The atomic mass can then be calculated by eq. 3.4 using the resonance of a reference ion as a calibration standard for the magnetic field. For that, ^{88}Sr$^+$ was chosen, because its mass is well known and close to those of the ions of interest which is ideal to minimize mass-dependent

Table 4.12: Free cyclotron frequencies determined by resonant buffer gas cooling.

Ion	# Ions	$t_{recording}$ (hh:mm:ss)	ν_c (Hz)	FWHM (Hz)
^{90}Rb$^+$	14	00:45:54 (45.9 min)	1 195 583.29 (2.71)	27.4 (5.8)
^{91}Rb$^+$	51	02:20:43 (140.75 min)	1 182 405.40 (2.07)	43.3 (4.2)
^{93}Rb$^+$	61	01:08:52 (68.87 min)	1 156 887.77 (2.08)	41.7 (4.2)
^{93}Rb$^+$	49	01:50:10 (110.17 min)	1 156 887.07 (2.29)	39.1 (8.4)
^{93}Sr$^+$	5	01:50:10 (110.17 min)	1 157 000.31 (5.16)	46.7 (3.9)

Table 4.13: Evaluated masses of the trapped ions. ^{88}Sr$^+$ was used as reference ion. Δm is defined as m_{atom}^{TT}- $m_{atom}^{AME2016}$.

Atom	m_{atom}^{TT} (μu)	rel. prec.	$m_{atom}^{AME2016}$ (μu)	Δm (μu)
^{90}Rb	89 914580 (210)	$2 \cdot 10^{-6}$	89 914798.8 (7.0)	-220 (210)
^{91}Rb	90 916670 (170)	$2 \cdot 10^{-6}$	90 916537.3 (8.4)	130 (170)
^{93}Rb	92 922060 (130)	$1 \cdot 10^{-6}$	92 922039.3 (8.4)	19 (130)
^{93}Sr	92 912990 (420)	$4 \cdot 10^{-6}$	92 914024.3 (8.1)	-1030 (420)

errors. In addition, it offered the strongest signal, allowing to take reference measurements quickly and regularly. Because it is produced in the same ion source as the ions of interest, further possible systematic errors caused by, e.g., deviating ion energy, are excluded. Therefore it is an excellent choice as a reference for mass measurements of short-lived fission products in the adjacent mass range. The calculated mass values of the trapped radioactive ions are listed in table 4.13. The data gained by the two ^{93}Rb$^+$ measurements have been averaged in order to reduce the statistical uncertainty. The determined atomic masses are compared to the masses listed in the Atomic Mass Evaluation 2016 [Wan17] and agree within the scope of accuracy. An exception to this is the measured mass of ^{93}Sr resulting from the low statistics. The determined masses reach a precision of 10^{-6}, which is the lower limit that can be reached by resonant buffer gas cooling. Due to broadening effects of the buffer gas, it is not possible to achieve a higher precision within the purification trap.

Chapter 5

Conclusion & Outlook

This thesis describes the successful coupling of the mass spectrometry experiment TRIGA-TRAP to the research reactor TRIGA Mainz. The major part is about the design of a new surface ion source, its implementation into the experimental setup and subsequent characterization. The installation of beam diagnostic stations and the introduction of continuous monitoring of crucial experimental parameters enabled extended performance studies and optimizations. A benchmarking step has been made by trapping and identification of short-lived fission products within the purification trap at TRIGA-TRAP for the first time.

Comprehensive monitoring of the gas-jet revealed detailed information about its performance, i.e., about the interconnection of transport efficiency and target chamber pressure. Measurement of the transport time of fission products yielded their dependence on the gas flow rate and can be used for further gas-jet optimizations. The operation of the surface ion source fulfilled all requirements as its performance was reliable, even at temperatures above 2000 °C, and yielded good ionization efficiencies for alkaline metals. In combination with precise alignment of the experimental setup and the implementation of new ion beam optics, an ion beam with excellent properties, especially a small and circularly focussed spot, was generated. The transmission of each component was optimized, resulting in a total transport efficiency of 1.3(3) % to the pulsed drift tube, which proved itself as the bottleneck of the beamline. Although its transmission was far below expectations it was sufficient to detect and confine short-lived fission products inside the purification trap.

This demonstrates that ion bunches coming from the RFQ can be decelerated from 30 keV to 1.1 keV. Four different radionuclide were captured inside the first Penning trap and identified by their atomic mass which in turn was determined by resonant buffer gas cooling. The evaluated masses agree with those listed in the AME2016 within the scope of accuracy, confirming the successful transport of fission products from the target to the Penning trap. As the subsequent precision trap was not available during the measurement campaigns, it was not possible to perform mass measurements using the ToF-ICR technique to gain a higher precision. Nevertheless, capturing short-lived fission products within the purification trap was an important advancement and finalized the commissioning of TRIGA-TRAP.

Furthermore, the beamline is now ready for high-precision mass measurements of neutron-rich nuclides, which was the main research goal of this experiment. Future data will contribute to test and refine theoretical models that investigate the nucleosynthesis, i.e., the path of the r-process. Moreover, as TRIGA-TRAP is a development platform for the planned mass spectrometry experiment MATS, the technical developments will contribute to this future setup. As MATS will be installed at the accelerator facility FAIR, the most exotic nuclides far from stability can be studied. The knowledge of their fundamental properties will contribute to further improvements of theoretical models and thereby the exact investigation of the nucleosynthesis process. This is of major interest, in particularly as the site of the r-process and its general path have been confirmed recently.

For future measurement campaigns at TRIGA-TRAP it is of interest to use a non-covered target of ^{235}U or ^{249}Cf to enable mass measurements of the heavy branch of fission products. It was not feasible so far as the usage of a non-covered target is associated with long-term contamination of the experimental setup, which is inconvenient when the setup needs a frequent exchange of components due to optimizations. As the beamline has now successfully been commissioned and provides a reliable and satisfying performance, this is no longer necessary. Already the easy to ionize isotope chain of ^{140}Cs to ^{144}Cs is of interest for high-precision mass measurements as their listed mass uncertainties are greater than 7 keV [Wan17].

The gas-jet performance could be optimized with regard to its long-term stability to reduce the uncertainties of determined transmissions of individual components. However, this is not necessarily needed for mass measurements as changes in the ion rates do not affect the measurement precision. Furthermore, shortening the capillaries or reducing transitions from one capillary diameter to another would be valuable to reduce particle losses. The latter would increase the transport time, but the gas-jet could be operated with higher gas flow rates or with helium instead of nitrogen if required. The first option would influence the pressure inside the target chamber and therefore the stopping power or the thermalization performance. The latter option would enable to run the system with higher gas flow rate while keeping the present stopping power inside the target chamber. Both changes would improve the transport time of the gas-jet significantly, thereby giving access to radio isotopes with shorter half-lives. A GeLi-detector with a better detection efficiency and a higher resolution or the installation of a tape station would enable to measure the short-lived nucleus ^{95}Sr or its daughter ^{95}Y in order to verify the ionization efficiency of strontium with an appropriate accuracy. However, as the pulsed drift tube represents the bottleneck of the setup, there is a urgent demand for a thorough investigation of the ion optics alignment as well as new calculations for the required voltages to efficiently guide the ions to the purification trap. In combination with a tuned precision trap and the implementation of the PI-ICR or FT-ICR technique, the way is then paved for high-precision mass measurements of neutron-rich nuclides at TRIGA-TRAP.

Bibliography

[Abb17] B. Abbott, R. Abbott, R. Adhikari et al. *Multi-messenger observations of a binary neutron star merger.* Astrophysical Journal Letters, **848(2)**, (2017) L12.

[Bah08] R. Bahreini, E. J. Dunlea, B. M. Matthew et al. *Design and operation of a pressure-controlled inlet for airborne sampling with an aerodynamic aerosol lens.* Aerosol Science and Technology, **42(6)**, (2008) 465–471.

[Bey71] G. Beyer, E. Herrmann, A. Piotrowski et al. *A new method for rare-earth isotope separation.* Nuclear Instruments and Methods, **96(3)**, (1971) 437–439.

[Bey14a] T. Beyer. *Installation and operation of a radio-frequency quadrupole cooler and buncher and offline-commissioning of the TRIGA-SPEC ion beam preparation transfer line.* Phd. thesis, University of Heidelberg (2014).

[Bey14b] T. Beyer, K. Blaum, M. Block et al. *An RFQ cooler and buncher for the TRIGA-SPEC experiment.* Applied Physics B: Lasers and Optics, **114(1-2)**, (2014) 129–136.

[BF17] O. Boine-Frankenheim, C. Trautmann, P. Senger et al. *FAIR forges its future.* CERN Courier.

[Bla06] K. Blaum. *High-accuracy mass spectrometry with stored ions.* Physics Reports, **425(1)**, (2006) 1–78.

[Bol90] G. Bollen, R. Moore, G. Savard et al. *The accuracy of heavy-ion mass measurements using time of flight-ion cyclotron resonance in a Penning trap.* Journal of Applied Physics, **68(9)**, (1990) 4355–4374.

[Bre09] M. Breitenfeldt, G. Audi, D. Beck et al. *Penning trap mass measurements of Cd 99-109 with the ISOLTRAP mass spectrometer, and implications for the r p process.* Physical Review C, **80(3)**, (2009) 035805.

[Bro86] L. S. Brown and G. Gabrielse. *Geonium theory: Physics of a single electron or ion in a Penning trap.* Rev. Mod. Phys., **58**, (1986) 233–311.

[Bro04] I. G. Brown. *The physics and technology of ion sources*, (WILEY-VCH, Weinheim, 2004).

[Brü83] M. Brügger. *Entwicklung einer Hochtemperaturoberflächenionenquelle für den Heliumjet Massenseparator Helios und Zerfallsstudien an massengetrenmass, neutronenreichen Praesodymisotopen.* Ph.D. thesis, Johannes Gutenberg-Universität Mainz (1983).

[Brü85] M. Brügger, N. Hildebrand, T. Karlewski et al. *Operation of a high temperature ion source at the helium-jet on-line isotope separator facility HELIOS.* Nuclear Instruments and Methods in Physics Research Section A: Accelerators, Spectrometers, Detectors and Associated Equipment, **234(2)**, (1985) 218–223.

[Cal59] A. Calverley. *Heating by electron bombardment.* Nature, **184**, (1959) 690–693.

[Col01] FAIR Collaboration et al. *FAIR CDR – An International Accelerator Facility for Beams of Ions and Antiprotons, Conceptual Design Report.* Tech. rep., Technical Report, GSI (2001).

[Dat56] S. Datz and E. H. Taylor. *Ionization on platinum and tungsten surfaces. I. The alkali metals.* J. Chem. Phys., **25(3)**, (1956) 389–394.

[Dre68] M. Dresser. *The Saha-Langmuir Equation and its Application.* Journal of Applied Physics, **39(1)**, (1968) 338–339.

[Dro17] M. Drout, A. Piro, B. Shappee et al. *Light curves of the neutron star merger GW170817/SSS17a: Implications for r-process nucleosynthesis.* Science, **358(6370)**, (2017) 1570–1574.

[Eib09] M. Eibach. *Characterization of a carbon aerosol generator in a helium gas-jet for the extraction of fission products from the research reactor TRIGA Mainz.* Master's thesis, Johannes Gutenberg-University Mainz (2009).

[Eib13] M. A. Eibach. *High-precision mass measurements in the realm of the deformed shell closure N= 152.* Phd. thesis, University of Heidelberg (2013).

[Eli13] S. Eliseev, K. Blaum, M. Block et al. *Phase-imaging ion-cyclotron-resonance measurements for short-lived nuclides.* Phys. rev. lett., **110(8)**, (2013) 082501.

[Elo09] V.-V. Elomaa, T. Eronen, U. Hager et al. *Light-ion-induced reactions in mass measurements of neutron-deficient nuclides close to A= 100.* Eur. Phys. J. A, **40(1)**, (2009) 1–9.

[Ett13] S. Ettenauer, M. Simon, T. Macdonald et al. *Advances in precision, resolution, and separation techniques with radioactive, highly charged ions for Penning trap mass measurements.* Inte. J. Mass Spectrom., **349**, (2013) 74–80.

[Fer07] R. Ferrer, K. Blaum, M. Block et al. *Development of a Fourier-Transform Ion-Cyclotron-Resonance detection for short-lived radionuclides at SHIPTRAP.* Eur. Phys. J. Spec. Top., **150(1)**, (2007) 347–348.

[Fra02] G. Fraser. *The ion detection efficiency of microchannel plates (MCPs).* Int. J. Mass Spectrom., **215(1)**, (2002) 13–30.

[Fre99] C. Freiburghaus, S. Rosswog, and F.-K. Thielemann. *R-process in neutron star mergers.* Astrophys. J. Lett., **525(2)**, (1999) L121.

[Geo07a] S. George, S. Baruah, B. Blank et al. *Ramsey method of separated oscillatory fields for high-precision Penning trap mass spectrometry.* Phys. Rev. Lett., **98(16)**, (2007) 162501.

[Geo07b] S. George, K. Blaum, F. Herfurth et al. *The Ramsey method in high-precision mass spectrometry with Penning traps: Experimental results.* Int. J. Mass Spectrom., **264(2)**, (2007) 110–121.

[Gib61] W. Gibson, T. Thomas, and G. Miller. *Structure in the Kinetic Energy Spectrum of Fragments from Thermal-Neutron-Induced Fission of U 235.* Phys. Rev. Lett., **7(2)**, (1961) 65.

[Gün93] R. Günther. *Charakterisierung der Eigenschaften der KCl-Aerosolpartikel eines He-Gasjets.* Master's thesis, Johannes Gutenberg-Universität Mainz (1993).

[Grä80] G. Gräff, H. Kalinowsky, and J. Traut. *A direct determination of the proton electron mass ratio.* Zeitschrift für Physik A Hadrons and Nuclei, **297(1)**, (1980) 35–39.

[Gru14] J. Grund. *Optimierung des Gas-Jet-Systems bei TRIGA-SPEC.* Master's thesis, Institute of Nuclear Chemistry, Johannes Gutenberg-University, Mainz, Germany (2014).

[Gru16] J. Grund, Ch. E. Düllmann, K. Eberhardt et al. *Implementation of an aerodynamic lens for TRIGA-SPEC.* Nucl. Instru. Meth. B, **376**, (2016) 225–228.

[Gut06] H. H. Gutbrod, I. Augustin, H. Eickhoff et al. *FAIR Baseline Technical Report.* GSI, (2006).

[Ham10] G. Hampel and K. Eberhardt. *Utilization of the research reactor TRIGA Mainz.* IAEA Technical Meeting on Commercial Products and Services of Research Reactors, Vienna, (2010).

[Hay14] W. M. Haynes. *CRC handbook of chemistry and physics*, (CRC press, 2014).

[Hin12] W. C. Hinds. *Aerosol technology: properties, behavior, and measurement of airborne particles*, (John Wiley & Sons, 2012).

[Joh73] P. Johnson, A. Bolson, and C. Henderson. *A high temperature ion source for isotope separators.* Nucl. Instrum. Meth., **106(1)**, (1973) 83–87.

[Jok02] A. Jokinen, J. Huikari, A. Nieminen et al. *The first cooled beams from JYFL ion cooler and trap project.* Nucl. Phys. A, **701(1-4)**, (2002) 557–560.

[Jok03] A. Jokinen, M. Lindroos, E. Molin et al. *RFQ-cooler for low-energy radioactive ions at ISOLDE.* Nucl. Instrum. Meth. B, **204**, (2003) 86–89.

[Kat11] J. Katakura. *JENDL FP decay data file 2011 and fission yields data file 2011.* JAEA-Data/Code, **25(2012)**, (2011) 1.

[Kat16] J. Katakura, F. Minato, and K. Ohgama. *Revision of the JENDL FP fission yield data.* In *EPJ Web of Conferences*, vol. 111, (EDP Sciences2016) 08004.

[Kes14] O. Kester, W. Barth, F. Hagenbuck et al. *Status of the FAIR accelerator facility.* Proceedings of the 5th International Particle Accelerator Conference, IPAC-2014, Dresden, Germany, 2084.

[Ket08] J. Ketelaer et al. *Triga-Spec: A setup for mass spectrometry and laser spectroscopy at the research reactor TRIGA Mainz.* Nucl. Instrum. Meth. A, **594(2)**, (2008) 162–177.

[Ket09] J. Ketelaer, K. Blaum, M. Block et al. *Recent developments in ion detection techniques for Penning trap mass spectrometry at TRIGA-TRAP.* Europ. Phys. J. A, **42(3)**, (2009) 311–317.

[Kir81] R. Kirchner. *Progress in ion source development for on-line separators.* Nucl. Instrum. Meth., **186(1-2)**, (1981) 275–293.

[Kir90] R. Kirchner. *On the thermoionization in hot cavities.* Nucl. Instrum. Meth., **292(2)**, (1990) 203–208.

[Kir03] R. Kirchner. *Review of ISOL target - ion-source systems.* Nucl. Instrum. Meth., **204**, (2003) 179–190.

[Klo66] W. D. Klopp and W. R. Witzke. *Mechanical properties and recrystallization behavior of electron-beam-melted tungsten compared with arc-melted tungsten.* NASA Technical Note D-3232, (1966).

[Kön95] M. König, G. Bollen, H.-J. Kluge et al. *Quadrupole excitation of stored ion motion at the true cyclotron frequency.* Int. J. Mass Spectrom., **142(1-2)**, (1995) 95–116.

[Kös08] U. Köster, O. Arndt, E. Bouquerel et al. *Progress in ISOL target–ion source systems.* Nucl. Instrum. Meth. B, **266(19)**, (2008) 4229–4239.

[Krä10] J. Krämer. *Construction and commissioning of a collinear laser spectroscopy setup at TRIGA Mainz and laser spectroscopy of Magnesium Isotopes at ISOLDE (CERN).* Ph.D. thesis, Johannes Gutenberg-University, Mainz (2010).

[Kre07] M. Kretzschmar. *The Ramsey method in high-precision mass spectrometry with Penning traps: Theoretical foundations.* Int. J. Mass Spectrom., **264(2)**, (2007) 122–145.

[Kre08a] M. Kretzschmar. *Calculating damping effects for the ion motion in a Penning trap.* Eur. Phys. J. D, **48(3)**, (2008) 313–319.

[Kre08b] M. Kretzschmar. *Theory of the elliptical Penning trap.* Int. J. Mass Spectrom., **275(1)**, (2008) 21–33.

[Laa15] J. J. W. de Laar. *Aufbau eines ortsempfindlichen Detektors für TRIGA-TRAP.* Master's thesis (2015).

[Lan25] I. Langmuir and K. Kingdon. *Thermionic effects caused by vapours of alkali metals.* In *Proc. R. Soc. Lond. A*, vol. 107, (The Royal Society1925) 61–79.

[Lav07] J. Lavoie, P. Bricault, J. Lassen et al. *Segmented linear radiofrequency quadrupole/laser ion source project at TRIUMF.* In *TCP 2006*, 389–395, (Springer2007).

[Lie91] K. Lieser. *Einführung in die Kernchemie, 3., neubearbeitete Auflage, VCH* (1991).

[Lie08] H. Liebl. *Applied charged particle optics*, vol. 2012, (Springer2008).

[Liu95a] P. Liu, P. J. Ziemann, D. B. Kittelson et al. *Generating particle beams of controlled dimensions and divergence: I. Theory of particle motion in aerodynamic lenses and nozzle expansions.* Aerosol Sci. Tech., **22(3)**, (1995) 293–313.

[Liu95b] P. Liu, P. J. Ziemann, D. B. Kittelson et al. *Generating particle beams of controlled dimensions and divergence: II. Experimental evaluation of particle motion in aerodynamic lenses and nozzle expansions.* Aerosol Sci. Tech., **22**, (1995) 314–324.

[Loh17] S. Lohse. *private communication* (2017).

[Lun03] D. Lunney, J. Pearson, and C. Thibault. *Recent trends in the determination of nuclear masses.* Rev. Mod. Phys., **75(3)**, (2003) 1021.

[Mac69] R. Macfarlane, R. Gough, N. Oakey et al. *The helium-jet recoil transport method.* Nucl. Instrum. Meth., **73(3)**, (1969) 285–291.

[Man08] D. Manura and D. Dahl. *SIMION Version 8.0. 4.* Idaho National Laboratory, **2011**.

[Man13] M. Manzolaro, A. Andrighetto, G. Meneghetti et al. *Ionization efficiency estimations for the SPES surface ion source.* Nucl. Instrum. Meth. B, **317**, (2013) 446–449.

[Mar07] A. Martın, D. Ackermann, G. Audi et al. *Mass measurements of neutron-deficient radionuclides near the end-point of the rp-process with SHIPTRAP.* Europ. Phys. J. A, **34(4)**, (2007) 341–348.

[Maz81] A. Mazumdar, H. Wagner, W. Walcher et al. *Performance of the on-line isotope separation facility HELIOS at the Mainz reactor.* Nucl. Instrum. Meth., **186(1)**, (1981) 131–134.

[Men75] H. Menke, N. Trautmann, and W. Krebs. *Irradiations by means of reactor pulses.* Tech. rep., Mainz Univ.(FR Germany). Inst. für Kernchemie (1975).

[Met14] B. D. Metzger and R. Fernández. *Red or blue? A potential kilonova imprint of the delay until black hole formation following a neutron star merger.* Monthly Notices of the Royal Astronomical Society, **441(4)**, (2014) 3444–3453.

[Mol96] P. Moller, J. Nix, and K.-L. Kratz. *Nuclear Properties for Astrophysical Applications.* arXiv preprint nucl-th/9601043.

[Moo13] I. Moore, T. Eronen, D. Gorelov et al. *Towards commissioning the new IGISOL-4 facility.* Nucl. Instrum. Meth. B, **317**, (2013) 208–213.

[Moo14] I. Moore, P. Dendooven, and J. Ärje. *The IGISOL technique - three decades of developments.* Hyperfine interactions, **223(1-3)**, (2014) 17–62.

[Nau17] P. Naubereit. *private communication* (2017).

[Nei08] D. Neidherr, K. Blaum, M. Block et al. *Measurement and simulation of the pressure ratio between the two traps of double Penning trap mass spectrometers.* Nucl. Instrum. Meth. B, **266(19)**, (2008) 4556–4559.

[Pau90] W. Paul. *Electromagnetic traps for charged and neutral particles.* Rev. Mod. Phys., **62(3)**, (1990) 531.

[Pia17] E. Pian, P. D'Avanzo, S. Benetti et al. *Spectroscopic identification of r-process nucleosynthesis in a double neutron-star merger.* Nature, **551(7678)**, (2017) 67.

[Rea89] *Technische Unterlagen für Bestrahlungen am FR TRIGA Mainz.* Tech. rep., Institut für Kernchemie (1989).

[Ren16] D. Renisch. *Installation and operation of a high-temperature surface ion source for the online coupling of TRIGA-SPEC to the TRIGA Mainz re-*

search reactor and high-precision mass measurements of transuranium nuclides at TRIGA-TRAP. Ph.D. thesis, Johannes Gutenberg-University of Mainz (2016).

[Rep12] J. Repp, C. Böhm, J. C. López-Urrutia et al. *PENTATRAP: a novel cryogenic multi-Penning-trap experiment for high-precision mass measurements on highly charged ions.* Appl. Phys. B, **107(4)**, (2012) 983–996.

[Reu83] U. Reus and W. Westmeier. *Atomic Data and Nuclear Data Tables 29: Catalog of Gamma-Rays from Radioactive Decay Part II.* Academic Press.

[Rod10] D. Rodríguez, K. Blaum, W. Nörtershäuser et al. *MATS and LaSpec: High-precision experiments using ion traps and lasers at FAIR.* The European Physical Journal Special Topics, **183(1)**, (2010) 1–123.

[Sat13] T. K. Sato, N. Sato, M. Asai et al. *First successful ionization of Lr (Z= 103) by a surface-ionization technique.* Rev. Sci. Instrum., **84(2)**, (2013) 023304–023304.

[Sat15a] T. Sato, M. Asai, A. Borschevsky et al. *Measurement of the first ionization potential of lawrencium, element 103.* Nature, **520(7546)**, (2015) 209–211.

[Sat15b] T. Sato, M. Asai, N. Sato et al. *Development of a He/CdI2 gas-jet system coupled to a surface-ionization type ion-source in JAEA-ISOL: towards determination of the first ionization potential of Lr (Z= 103).* J. Radioan. Nucl. Ch., **303(2)**, (2015) 1253–1257.

[Sat17] T. K. Sato. *private communication* (2017).

[Sav91] G. Savard, G. Bollen, H.-J. Kluge et al. *A new cooling technique for heavy ions in a Penning trap.* Phys. Lett. A, **158(5)**, (1991) 247–252.

[Sch66] H. Schmitt, J. Neiler, and F. Walter. *Fragment Energy Correlation Measurements for Cf 252 Spontaneous Fission and U 235 Thermal-Neutron Fission.* Phys. Rev., **141(3)**, (1966) 1146.

[Sch16] F. Schneider. *First steps of the ECHo experiment: Penning-trap mass measurements of the* ^{163}*Ho electron capture process and implantation of ultrapure Ho into microcalorimeter arrays.* Phd. thesis, University of Mainz (2016).

[Smo12] C. Smorra. *High-precision Q-value and mass measurements for neutrino physics with TRIGA-TRAP and commissioning of an on-line ion source for TRIGA-SPEC.* Phd. thesis, University of Heidelberg (2012).

[Sto13] T. Stora. *Recent developments of target and ion sources to produce ISOL beams.* Nucl. Instrum. Meth. B, **317**, (2013) 402–410.

[Str92] P. Strehl. *Beam diagnostics.* Rev. Sci. Instrum., **63(4)**, (1992) 2652–2659.

[Stu13] S. Sturm, A. Wagner, M. Kretzschmar et al. *g-factor measurement of hydrogenlike 28 Si 13+ as a challenge to QED calculations.* Phys. Rev. A, **87(3)**, (2013) 030501.

[Tur12] M. Turek, A. Droździel, K. Pyszniak et al. *Simulations of ionization in a hot cavity surface ion source.* Rev. Sci. Instrum., **83(2)**, (2012) 023303.

[Wan06] X. Wang and P. H. McMurry. *A design tool for aerodynamic lens systems.* Aerosol Sci. Tech., **40(5)**, (2006) 320–334.

[Wan17] M. Wang, G. Audi, F. Kondev et al. *The AME2016 atomic mass evaluation (II). Tables, graphs and references.* Chinese Physics C, **41(3)**, (2017) 030003.

[Web03] C. Weber. *Konzeption eines kryogenen Penningfallenaufbaus für SHIP-TRAP und Massenbestimmungen von Radionukliden um den Z= 82-Schalenabschluss an ISOLTRAP.* Phd. thesis, University of Heidelberg (2003).

[Web05] C. Weber, K. Blaum, M. Block et al. *FT-ICR: A non-destructive detection for on-line mass measurements at SHIPTRAP.* Eur. Phys. J. A, **25(1)**, (2005) 65–66.

[Wei35] C. v. Weizsäcker. *Zur Theorie der Kernmassen.* Zeitschrift für Physik, **96(7-8)**, (1935) 431–458.

[Wie72] K. Wien, Y. Fares, and R. Macfarlane. *Application of the helium-jet technique for fission fragment transport from spontaneous fission sources.* Nucl. Instrume. Meth., **103(2)**, (1972) 181–187.

[Wiz79] J. L. Wiza. *Microchannel plate detectors.* Nucl. Instrum. Meth., **162(1-3)**, (1979) 587–601.

[Woh78] H. Wohlfarth, W. Lang, H. Dann et al. *The ionic charge distribution of fission products and the influence of internal conversion on highly preionized heavy ions.* Zeitschrift für Physik A Atoms and Nuclei, **287(2)**, (1978) 153–163.

[Wol76] H. Wollnik. *Principles behind a He-jet system and its application for isotope separation.* Nucl. Instrum. Meth., **139**, (1976) 311–318.

[Wol12] H. Wollnik. *Optics of charged particles*, (Elsevier, 2012).

[Zan59] E. Y. Zandberg and N. Ionov. *Surface ionization.* Soviet Physics Uspekhi, **2(2)**, (1959) 255.

[Zha04] X. Zhang, K. A. Smith, D. R. Worsnop et al. *Numerical characterization of particle beam collimation: Part II integrated aerodynamic-lens–nozzle system.* Aerosol Sci. Techn., **38(6)**, (2004) 619–638.

[Zie13] J. Ziegler, J. Biersack, and M. Ziegler. *The stopping and range of ions in matter, Software* (2013).

[Zud86] F. Zude. *Transportverhalten von Spaltprodukten.* Master's thesis, Johannes Gutenberg-Universität Mainz (1986).